INVESTIGATION OF FATIGUE LIFE AND FRACTURE MECHANICS OF UNCONSTRAINED Ni-Mn-Ga SINGLE CRYSTALS

by

Theodore Bryson Lawrence

A thesis

submitted in partial fulfillment

of the requirements for the degree of

Master of Science in Materials Science and Engineering

Boise State University

December 2014

BOISE STATE UNIVERSITY GRADUATE COLLEGE

DEFENSE COMMITTEE AND FINAL READING APPROVALS

of the thesis submitted by

Theodore Bryson Lawrence

Thesis Title: Investigation of Fatigue Life and Fracture Mechanics of Ni-Mn-Ga Single Crystals

Date of Final Oral Examination: 23 October 2014

The following individuals read and discussed the thesis submitted by student Theodore Bryson Lawrence, and they evaluated his presentation and response to questions during the final oral examination. They found that the student passed the final oral examination.

Peter Müllner, Ph.D.	Chair, Supervisory Committee
Paul Lindquist, Ph.D.	Member, Supervisory Committee
Trevor Lujan, Ph.D.	Member, Supervisory Committee

The final reading approval of the thesis was granted by Peter Müllner, Ph.D., Chair of the Supervisory Committee. The thesis was approved for the Graduate College by John R. Pelton, Ph.D., Dean of the Graduate College.

ACKNOWLEDGEMENTS

I would like to thank all of the people who played a part in helping me get through graduate school. Dr. Peter Müllner, you have been a constant source of inspiration, knowledge, and guidance. Your ability to convey complex material in a way that was easy to understand was invaluable for my learning experience. I would also like to thank Dr. Paul Lindquist for his guidance and direct involvement with the project in helping with experimental set up and procedure. You were always willing to lend a hand or offer advice for which I am grateful.

The Müllner research group was a vital part to my success. The other members of the group offered their insight, troubleshooting abilities, and technical skills without hesitation. The conversation and caliber of personalities make working with them a pleasure. I cannot begin to express my gratitude for the staff in the MSE office. The work done to help our experience be the best it could be as well as planning for travel abroad was outstanding. Phil Boysen was never too busy for me and always made it seem like my research was a priority.

Finally, I would like to thank my wife, Alexa, for her unending support and understanding when I was working late. She also helped motivate me to push through the hard parts.

Financial support was provided by the Office of Basic Energy Sciences of the Department of Energy.

ABSTRACT

Ni-Mn-Ga is a magnetic shape memory alloy (MSMA) that exhibits large recoverable strains. The magnetic field induced strain (MFIS) occurs through twin boundary motion resulting in reorientation of the crystal structure, which is coupled to the magnetic moment of the material. The shape memory capabilities of the material make it promising for applications including microactuators, sensors, microfluid pumps, refrigeration, energy harvesting, and data storage.

In order for Ni-Mn-Ga to become a viable option for use in commercial applications, the performance and reliability must be on par with industry standards. Ni-Mn-Ga has been shown to achieve high cycles at low strains, but there is little data on the fatigue life of samples that are actuated near the theoretical strain limit. 10M $Ni_{51.2}Mn_{26.6}Ga_{22.2}$ single crystal samples were magneto-mechanically cycled in a rotating magnetic field under minimal mechanical constraints to study the effects of crystal imperfections on fatigue life and fracture mechanics with a consideration of surface roughness. High surface roughness and areas of high local stress concentration lead to crack initiation. Cracks tended to propagate in <110> directions at an angle of 45° to the axis about which the magnetic field rotated. Crystal defects, surface imperfections, and total strain should be minimized to achieve long operational life.

TABLE OF CONTENTS

LIST OF TABLES

LIST OF FIGURES

LIST OF ABBREVIATIONS

at-%	Atomic Percent
DIC	Differential Interference Contrast
EDS	Electron Dispersive X-Ray Spectroscopy
FCC	Face-Centered Cubic
FSMA	Ferromagnetic Shape Memory Alloy
MFIS	Magnetic Field Induced Strain
NM	Non-Modulated
PID	Proportional Integral Derivative controller
SCFH	Standard Cubic Feet per Hour
SEM	Scanning Electron Microscope
SMA	Shape Memory Alloy
SME	Shape Memory Effect
VSM	Vibrating Sample Magnetometer
XRD	X-Ray Diffraction

CHAPTER ONE: INTRODUCTION

Magnetism is one of the oldest phenomena in the history of science. Magnetism is used in many applications including data storage, speakers, power transformers, and electric motors, etc. Magnetism is a force of attraction or repulsion that acts at some distance away from a magnetic material due to the magnetic field of that material. The magnetic field produces a force that will be experienced by an electric charge passing through the field, the torque on a magnetic dipole, or reorientation of spins on electrons in certain atoms [1]. A change in magnetic flux near a conductive material will induce a current of electrons

Recent discoveries have been made where certain alloys will change shape in a magnetic field. Ferromagnetic shape memory alloys (FSMA) such as Ni-Mn-Ga have recently emerged as a new class of materials that exhibit large magnetic field induced strains (MFIS) [2]. MFIS occurs through the reorientation of the crystal structure in an applied magnetic field. FSMAs share similarities with magnetostrictive materials such as Terfenol-D, which also exhibit strains in an applied magnetic field. The highest strains measured for Ni-Mn-Ga is 12% compared to 0.2% for Terfenol-D [3, 4]. The main difference between these two types of materials is that the strain associated with FSMAs is due to a crystallographic reorientation whereas the strain associated with magnetostriction is due to a homogeneous straining of bonds [5].

Large MFIS make Ni-Mn-Ga an ideal solution for unique magnetic actuation applications. A novel micro-pump application has been developed by Ullakko et al. using a Ni-Mn-Ga element as the pumping mechanism that could one day be used with compact lab-on-a-chip applications [6]. The Ni-Mn-Ga element is sealed against a glass plate with an inlet and outlet. The device acts like a swallow pump in that a magnetic field is used to induce shrinkage in a localized area near an inlet of liquid. The pocket filled with liquid can be transported by manipulating the magnetic field and thus the location of the shape change. The only movement is in the localized change of shape of the Ni-Mn-Ga element, so the overall complexity, compared to other mechanical pumps containing many moving parts, is kept to a minimum. Ni-Mn-Ga alloys have also been synthesized into polycrystalline foam structures that act similarly to single crystalline samples with strains as high as 8.7% [7]. Bruno et al. used a Ni-Mn-Ga element in a constant magnetic field and actuated the sample with a strain controller within a pickup coil to harvest energy from the crystal reorientation [8]. It is even possible to create a four state memory device with Ni-Mn-Ga as opposed to the typical binary memory devices that are prevalent now [9].

Ni-Mn-Ga appears to be a versatile alloy and its shape changing properties have been studied for nearly 20 years. However, there are no commercially available devices that utilize Ni-Mn-Ga. This is partly because device designers lack confidence in the reliability of the actuating mechanisms. Many properties of Ni-Mn-Ga have been extensively characterized, including transformation behavior, transformation temperatures, magnetostress and strain, and magneto-caloric properties [10-14]. These properties are important to understand when considering this material for commercial

applications; however, a phenomenon that is not widely studied in the Ni-Mn-Ga community is fatigue. When FSMAs are cycled thousands or even millions of times, cracks begin to initiate and propagate through the material [15]. In order for this material to become a viable option for use in commercial applications, the reversibility, repeatability, and consistency of the crystal reorientation must meet the needs of the application. In high frequency operation of a FSMA, it is important to understand the fatigue life and properties of the material. This thesis studies fatigue life and fracture mechanics of Ni-Mn-Ga single crystalline samples tested in a purely magnetic actuation mode.

CHAPTER TWO: MOTIVATION

Ni-Mn-Ga is an exciting material with potential uses in actuation, micro-pumps, sensors, and energy harvesting [2, 8, 16]. Commercial applications require that a device is sufficiently dependable to justify production costs, complexity, and implementation. One of the largest benefits to Ni-Mn-Ga FSMA devices is their simplicity due to having very few moving parts. A Ni-Mn-Ga micro-pump only utilizes the shape change of an FSMA element to transport liquid between an inlet and outlet. A typical mechanical pump or actuation device will contain many moving parts that could contribute to failure. This makes FSMAs ideal for applications that require a small footprint and minimal energy usage.

This research investigates the fatigue and fracture mechanics of Ni-Mn-Ga single crystals grown via the Bridgman-Stockbarger method. Aaltio et al. have performed long term fatigue testing using an oscillating mechanical force to linearly actuate single crystalline Ni-Mn-Ga samples up to 2×10^9 cycles at a frequency of 250 Hz and a strain of ±1% [17, 18]. This type of testing was purely mechanical, but commercial applications will involve the use of magnetic fields to actuate the FSMA. Therefore, fatigue testing should be performed in such a way that the performance is replicated.

A large number of samples should be analyzed to achieve a statistical understanding of the behavior of Ni-Mn-Ga at high cycles. Previous methods used for fatigue testing are time intensive because only one sample can be tested at a time. A task

of this study was to develop a method with which many samples can be tested simultaneously. The instrument should also utilize a rotating magnetic field to actuate samples in a similar method that would be used in commercial applications.

Chmielus et al. have performed magnetic field actuated fatigue testing on samples constrained in a strain measuring fixture in a rotating magnetic field [19]. Constraints from testing instrument fixtures minimize the maximum strain exhibited by a sample and could limit capabilities in applications. The goal of this thesis is to research the fatigue life and fracture mechanics of Ni-Mn-Ga single crystals that are unconstrained in a rotating magnetic field with a consideration of surface properties.

CHAPTER THREE: BACKGROUND

3.1 Magnetism

3.1.1 Magnetic Moments

The magnetization, **M**, of a material represents the response of a magnetic material to an applied magnetic field, **H**. The magnetic moment determines the amount of torque, $\boldsymbol{\tau}$, a magnetic dipole or a current loop will experience in an external magnetic field [1]. A magnetic dipole or current loop model is typically used to describe magnetism. The magnetic field produced by a current loop is similar to that of the field produced by two magnetic poles. The torque on a moment can be represented by

$$\boldsymbol{\tau} = \mathbf{m} \times \mathbf{B} \tag{3.1}$$

where **m** is the magnetic moment and **B** is the magnetic induction. The magnetic induction is the flux density of the magnetic field and will induce alignment of the magnetic moment to be parallel to the induction. In a ferromagnetic material, each atom has a magnetic moment associated with it. A magnetic material can be described by approximating the material as a collection of magnetic moments. Magnetization is the summation of these moments per unit volume.

Magnetic materials contain volumes, called domains, of magnetic moments. All of the magnetic moments within a domain are aligned in parallel with each other. Neighboring domains will become randomly oriented in order to minimize the

magnetostatic energy. The domains in magnetic materials will preferentially align in an applied magnetic field.

When a magnetic material is placed in a magnetic field, the induction within the material will be altered due to that materials permeability. The permeability of a material is a quantity that measures the extent of magnetization that a material will experience within an external magnetic field. The permeability of free space, μ_o, is a constant that represents the ability of a magnetic field to form in a vacuum. The magnetic induction, **B**, and magnetic field intensity, **H**, are related by the free space permeability in the following equation

$$\mathbf{B} = \mu_o(\mathbf{H} + \mathbf{M}) \tag{3.2}$$

where **M** is the magnetization of the material. The field lines of **B** and **H** point in the same direction on the outside of the material, but on the inside of the material they point in opposite directions [1]. The negative direction of magnetic field lines within the material relative to the external magnetic field lines is the demagnetizing field. The demagnetizing field is dependent on the geometry of the material, magnetization, and the intensity of the surrounding magnetic field.

3.1.2 Ferromagnetic Materials

There are several types of magnetic materials including diamagnetic, paramagnetic, ferromagnetic, anti-ferromagnetic, and ferrimagnetic materials. Magnetic materials are classified according to their magnetic susceptibility. Magnetic susceptibility is a constant that describes the extent to which a material will be magnetized in a magnetic field [20]. An atom can be considered a magnetic dipole with an associated magnetic moment if the atom contains unpaired electrons. Diamagnetic materials have

filled electron shells and therefore have no magnetic moment without the presence of a magnetic field; see Figure 3.1. When a material is placed in a magnetic field, the electrons orbiting atoms will experience a force resulting in a reduced magnetic moment. Diamagnetic materials oppose an applied magnetic field; they have a negative magnetic susceptibility due to an oppositely induced moment according to Lenz' Law.

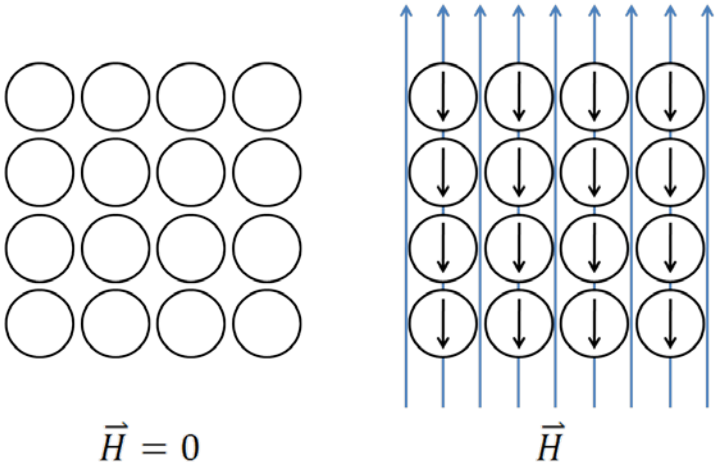

Figure 3.1 Atoms of a diamagnetic material have no magnetic moment associated with them. When a magnetic field is applied (right image), magnetic moments are induced in the opposite direction of the applied magnetic field.

Atoms in paramagnetic materials contain unpaired electrons. The magnetic moments associated with the unpaired electrons are allowed to freely orient themselves. The magnetic susceptibility is positive, but relatively small for paramagnetic materials, meaning the magnetic moments will align parallel to an applied magnetic field; see Figure 3.2.

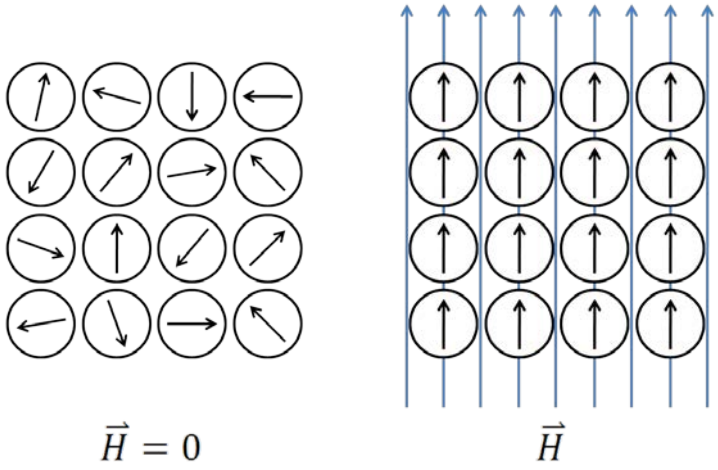

Figure 3.2 Magnetic moments in a paramagnetic material are randomly oriented (left). In an applied magnetic field (right), the moments will align parallel to the applied magnetic field in the same direction.

Atoms in ferromagnetic materials also contain unpaired electrons with magnetic moments that will tend to align with an applied magnetic field. The moments in ferromagnetic materials remain aligned with each other without the presence of an applied magnetic field; see Figure 3.3. Anti-ferromagnetic materials are similar to ferromagnetic materials in that they retain an ordered structure, except the nearest neighbor moments are anti-parallel to each other. Ferrimagnetic materials are another type of anti-ferromagnet, but one set of atoms contains a smaller moment relative to the anti-parallel moments.

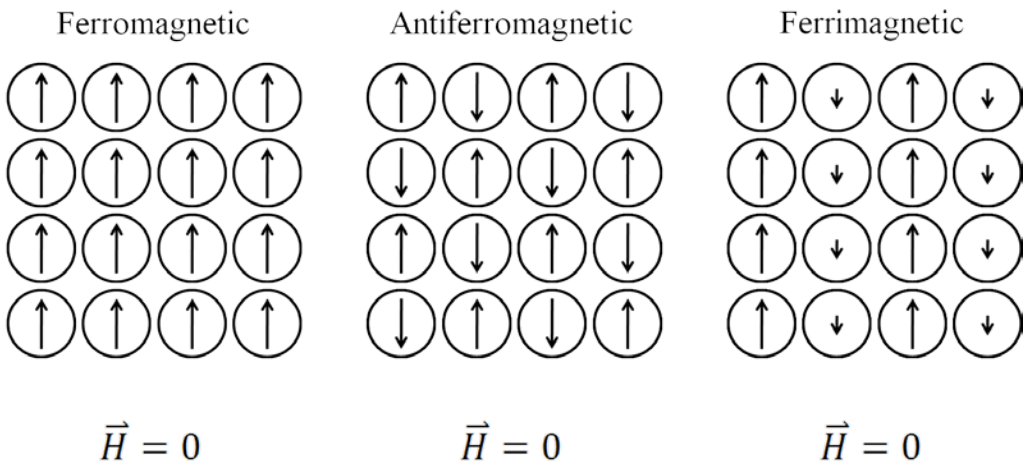

Figure 3.3 Magnetic moment models of ordered magnetic materials. In the image on the left, the magnetic moments of ferromagnetic materials remain aligned parallel to one another without the presence of a magnetic field. Nearest neighbor antiferromagnetic moments align anti-parallel relative to one another. Ferrimagnetic materials contain separate lattices with anti-parallel aligned magnetic moments.

3.1.3 Curie Temperature

At high temperatures, ferromagnetic materials lose their magnetization. This temperature is known as the Curie temperature, T_c. This is the temperature at which a material transitions from ferromagnetic to paramagnetic; see Figure 3.4. Above the Curie temperature, the thermal disorder overcomes the weak interactions of the magnetic moments and the moments become randomly oriented. Below the Curie temperature, the material is ferromagnetic and the magnetic dipoles are all aligned parallel to one another creating a magnetic field.

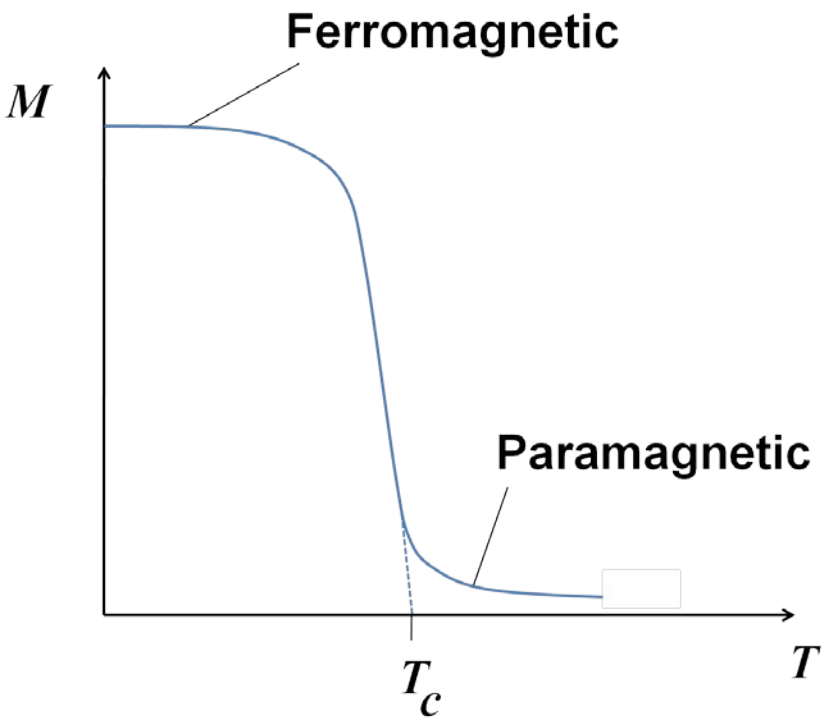

Figure 3.4 Magnetization as a function of temperature for a material that exhibits ferromagnetic properties at low temperatures. At low temperatures, below T_c, the magnetic moments of the material are aligned. At high temperatures, above T_c, the thermal energy overcomes the order of the magnetic moments and the material exhibits paramagnetic properties.

3.1.4 Magnetocrystalline Anisotropy

The magnetic moments of neighboring domains exhibit different orientations. When these domains are aligned with each other, the material is in a fully magnetized state. When they are randomly oriented, the material is demagnetized. When a magnetic field is applied to a demagnetized ferromagnetic material, the magnetic domains and moments will preferentially align with the magnetic field; see Figure 3.5. When all of the magnetic moments have aligned via domain wall motion, the material has reached its saturation magnetization and the magnetization will not increase upon further increase of the magnetic field. As the magnetic field is removed, the magnetization of ferromagnetic materials only slightly decreases because the moments will remain aligned with each

other. If a negative magnetic field is applied in the opposite direction, the magnetic moments will become disordered as the moments realign themselves. The magnetization will become zero when the moments are randomly oriented. As the negative field increases, the material will become saturated once again as it becomes negatively magnetized. The magnetization of a ferromagnetic material forms a hysteresis loop as a function of applied magnetic field.

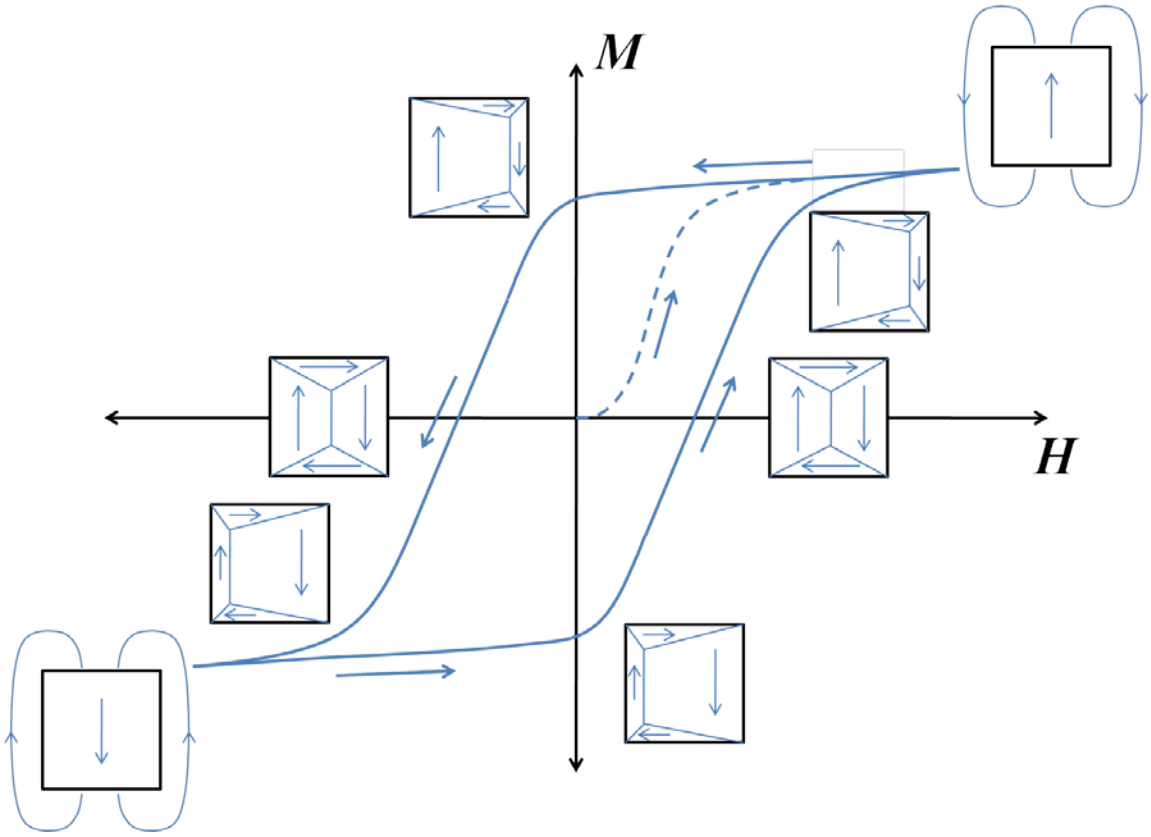

Figure 3.5 Hysteresis loop for the magnetization of a ferromagnetic material. The material starts out as demagnetized at the origin. An increasing magnetic field induces alignment of the magnetic domains to saturation of the magnetization. Ferromagnetic materials retain magnetization when the magnetic field is removed. An increasingly negative field will decrease the magnetization of the material to its original state. As the negative field is continuously applied, the magnetization will saturate in the negative direction. This process can be repeated in either direction.

Due to the shape of their atomic crystal structure, some ferromagnetic materials require higher magnetic fields applied in specific directions in order to fully magnetize

the material [21]. If a structure contains an easy and a hard axis of magnetization, this is what is known as magnetocrystalline anisotropy; see Figure 3.6. The initial slope of the M-H curve in the easy axis is higher than the hard axis curve. A single crystal ferromagnetic material with a magnetic field applied parallel to the easy axis of magnetization will reach saturation magnetization with a lower field than if it was applied parallel to the hard axis. The shape of the magnetization curve depends on the temperature, constituents of the material, crystal structure, and composition.

The energy required to fully magnetize a sample is larger when the magnetic field is parallel to the hard axis of magnetization. The difference between the energy required to magnetize a sample to saturation in the easy and hard axis is known as the magnetic anisotropy energy. The magnetic field required to saturate the magnetization of a sample along the hard axis is the anisotropy field.

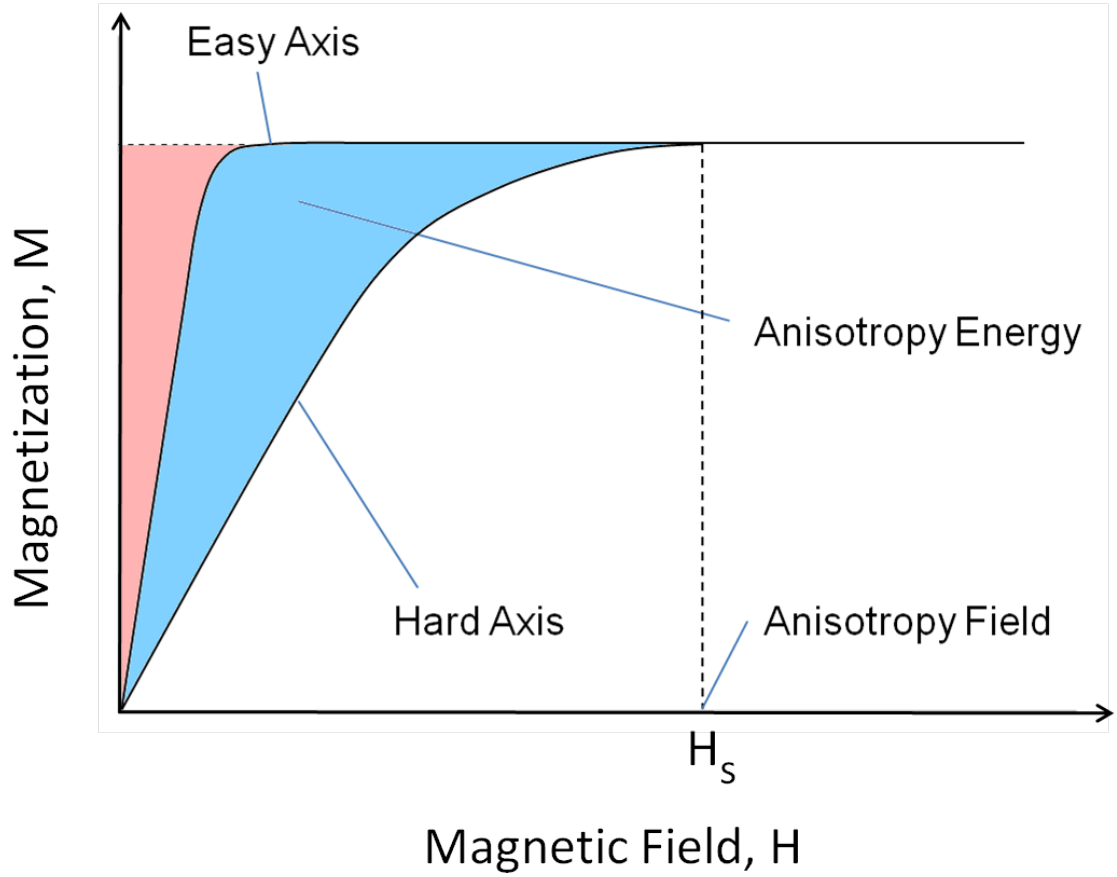

Figure 3.6 Magnetization as a function of magnetic field for a ferromagnetic material exhibiting magnetocrystalline anisotropy. The area between the curves and the magnetization axis is the energy required to achieve saturation magnetization. The blue shaded area is the magnetic anisotropy energy. The anisotropy field is the magnetic field required to saturate the sample's magnetization when the magnetic field is applied parallel to the hard axis of magnetization.

3.1.5 Shape Anisotropy

The shape of a magnetic material has an effect on the magnetic field experienced within the finite volume of that material. This is known as shape anisotropy. A magnetized sample will develop oppositely charged north and south poles on its surface. The magnetic field lines of a material travel from the north pole to the south pole; see Figure 3.7. Therefore, there is an internal magnetic field known as the demagnetizing field, $\mathbf{H}_d$, which will oppose an applied magnetic field. The magnetization vector, **M**, and the magnetic induction lines, **B**, travel from the south pole to the north pole.

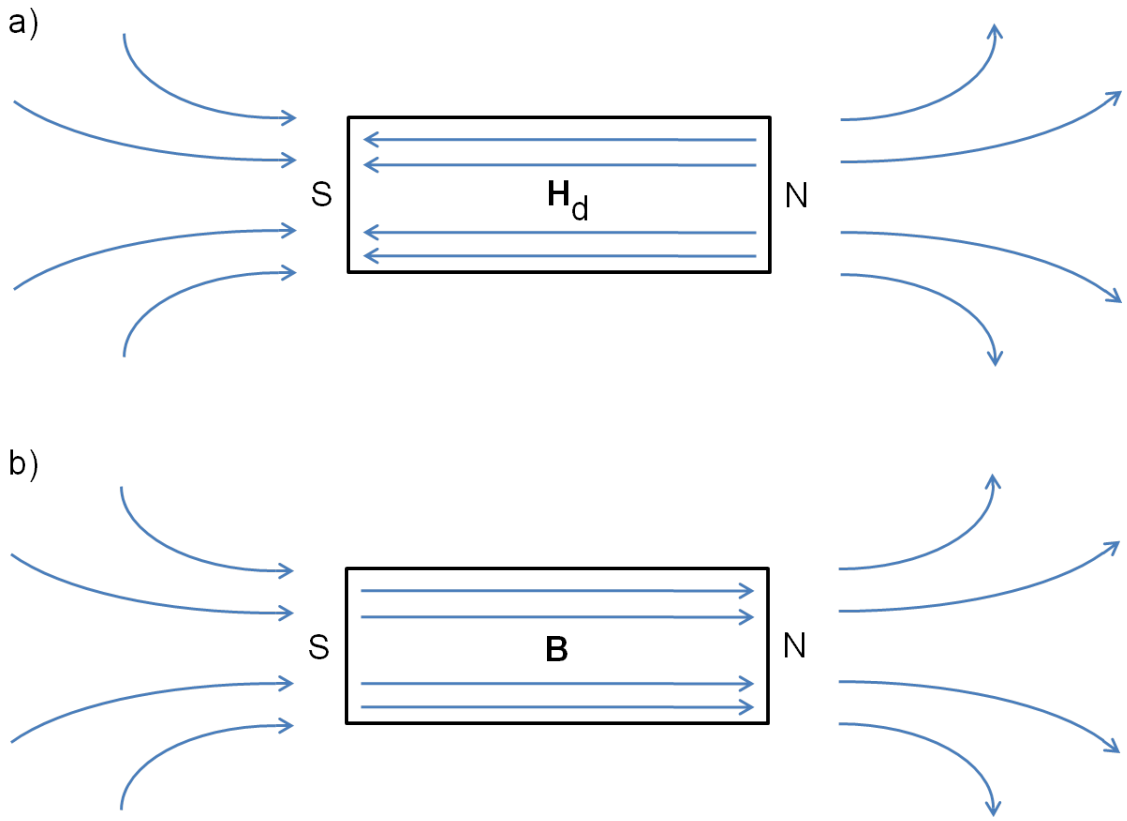

Figure 3.7 a) Magnetic field lines within and outside of a magnetic material. b) Induction field lines within and outside of a magnetic material. The magnetic field lines within a magnetized material point in the opposite direction of the induction field lines. On the outside of the material, the lines point in the same direction.

The demagnetizing field in a sample is proportional to the magnetization by the following equation

$$\boldsymbol{H}_{\mathrm{d}} = -N_{\mathrm{d}}\boldsymbol{M} \tag{3.3}$$

where N_{d} is the demagnetizing factor, which depends on the geometry of the sample and depends on the orientation of the sample within the magnetic field. The effective field, $\boldsymbol{H}_{\mathrm{eff}}$, within the sample is the vector sum of the applied field and the demagnetizing field:

$$\boldsymbol{H}_{\mathrm{eff}} = \boldsymbol{H}_{\mathrm{app}} - N_{\mathrm{d}}\boldsymbol{M} \tag{3.4}$$

where $\boldsymbol{H}_{app}$ is the applied magnetic field. When measuring magnetic properties of a material it is necessary to exclude error from measurements by taking the demagnetizing field into account in order to determine the effective field.

3.2 Shape Memory Alloys

3.2.1 Phenomenology

The shape memory effect (SME) is generally attributed to the ability to reverse a large stress-induced deformation at low temperature by heating the material to a high temperature. Nickel titanium, or Nitinol, is the most commonly known SMA and is currently used in many applications such as arterial stents, orthodontics, and actuators. Nitinol was discovered in 1959 by William J. Buehler and Frederick E. Wang of the U.S. Naval Ordnance Laboratory [22]. The shape memory effect is related to a diffusionless phase transformation. The low temperature martensite phase is heavily twinned. Nitinol exhibits SME when it is heated from the deformed martensite state to the austenite phase; see Figure 3.8. The reverse phase transformation returns the material to its original shape. The phase transformation can also be stress induced through deformation in the austenite phase. In this case, the austenite phase recovers upon unloading, resulting in super-elastic properties.

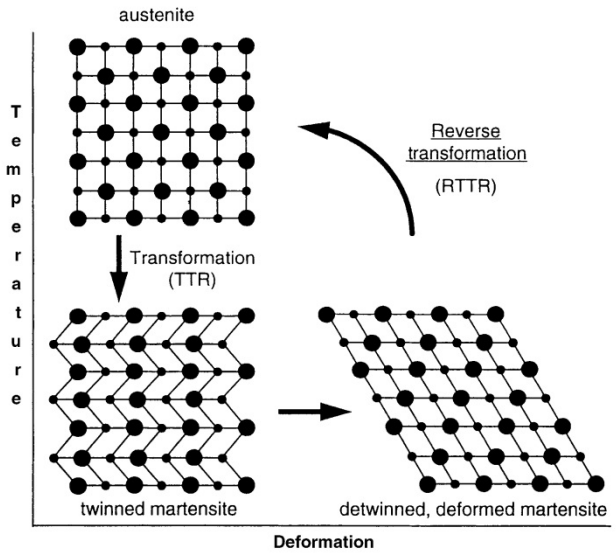

Figure 3.8 Representation of the martensitic transformation and shape memory effect of NiTi alloy. Reprinted with kind permission from [23].

3.2.2 Martensitic Transformation

Shape memory alloys (SMA) exhibit a structural transformation upon cooling from a high temperature, high symmetry austenite phase to a lower temperature, lower symmetry martensite phase. The phase change is abrupt and the change in lattice parameter is significant and discontinuous, but the change occurs without diffusion and the relative position of the atoms remains unchanged [24, 25]. There is no shuffling, which means that each phase can be obtained through a distortion from the previous phase.

Upon cooling from the martensite phase, the austenite phase starts to form at the austenite start temperature, A_s. The point at which all of the martensite phase has transformed completely to austenite is the austenite finish temperature, A_f. During the martensite transformation, physical properties change if the material is ferromagnetic. For example, the magnetization at low magnetic field changes during the phase transformation; see Figure 3.9. Upon cooling, when the temperature reaches the

martensite start temperature, M_s, the martensite phase will start to become stable and nucleate within the sample. The martensite and austenite transformation temperatures are dependent on composition and will vary slightly [26]. When the sample has transformed completely, the martensite finish temperature has been reached, M_f. The transformation is reversible, meaning no intermediate phases are formed during the phase transformation from austenite to martensite and vice versa.

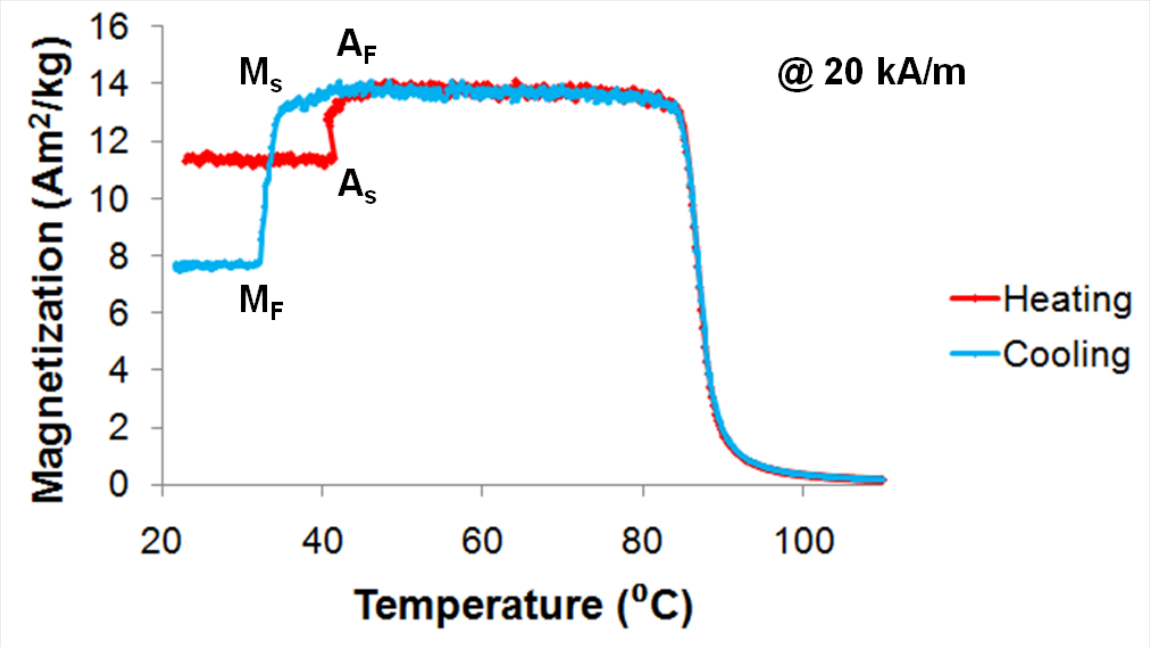

Figure 3.9 Transformation temperature diagram. The red line indicates the magnetization as a function of temperature as the temperature is increased. The blue line indicates the magnetization temperature as a function of temperature as the temperature is decreased.

3.2.3 Twinning

There are two main modes of deformation known as slip and twinning; see Figure 3.10. Slipping occurs by the motion of lattice dislocations. The crystal structure on either side of a slip plane is identical to each other. Twins are two adjacent crystals that are related to each other by a reflection about a common plane or a rotation of π about a

common direction. One region is related to another by a homogeneous simple shear of the crystal lattice. The plane interface intersecting the two regions is called the twin boundary. In deformation through twinning, there is no long range motion of atoms resulting in a movement that is less than their interatomic spacing. The tendency for a material to deform by slipping or twinning is dependent on the type of material, chemical composition, temperature, etc. Deformation by twinning occurs typically in alloys with low symmetry and large lattice constants.

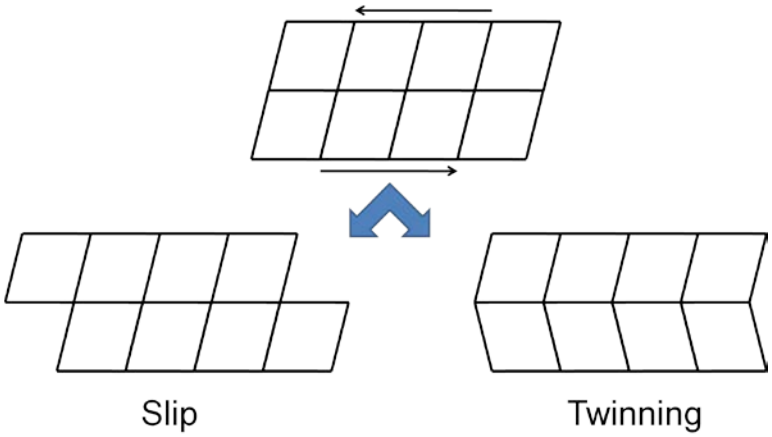

Figure 3.10 The top structure represents an undistorted lattice. Atoms would be located at the intersections of the crystal lattice. Slip deformation can occur via lattice dislocation motion. Deformation via twinning occurs via shearing of atoms.

Twinning is characterized by four twinning elements K_1, K_2, η_1, and η_2; see Figure 3.11 [27]. The twinning plane, K_1, is the interface between the parent matrix and the twinned matrix. The shear direction, η_1, is the direction that an atom is shifted when transforming from the parent location to the twinned location. The second plane is the conjugate plane, K_2, containing the conjugate twinning direction, η_2, and these two components describe the twin [28]. K'_2 is the position of K_2 prior to twinning. η_1 and η_2 lie on planes K_1, and K_2, respectively. The shear plane S is perpendicular to K_1 and contains η_1 and η_2 where η_1 lies along the intersection of S and K_1. Because the crystal

lattice parameters do not change on either side of the twinning plane after shear, there are three different types of twins possible, including type I, type II, and compound twins [29]. Type I twins are described with a mirror symmetry about the K_1 plane where K_1 and η_2 are the only elements with rational indices. Type II twins are characterized by a rotation of π about η_1 with rational elements K_2 and η_1. All of the twinning elements in compound twins are rational .

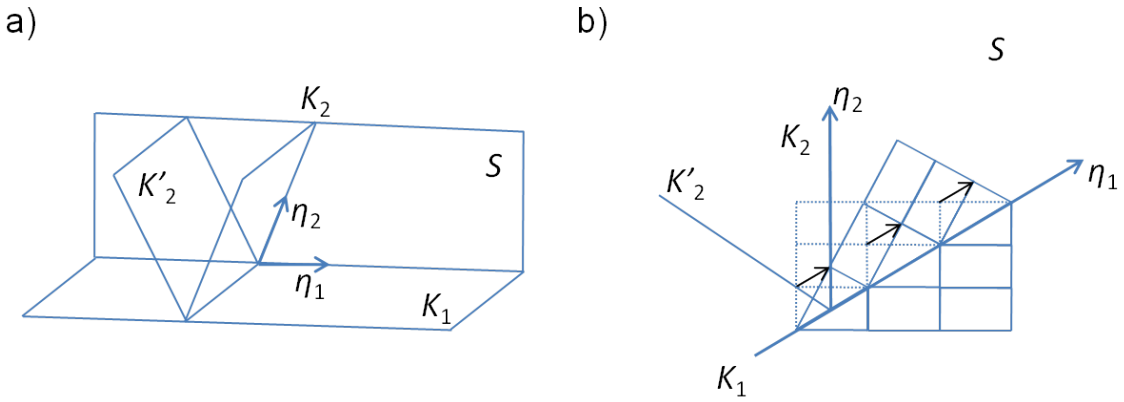

Figure 3.11 a) Twinning elements K_1, K_2, η_1, and η_2. η_1 and η_2 lie on the shear plane, S. The K_2 plane lies along a row of atoms after twinning from the K'_2 plane. b) Secondary view normal to the shear plane. K_1 is the twinning plane and η_1 is the shear direction of the atoms. a) Redrawn from Acta Materialia, vol. 58, P. Müllner and A. H. King, Deformation of hierarchically twinned martensite, pp. 5242-5261, (2010), with permission from Elsevier. b) Redrawn from Thermo-Mechanical Processing of Metallic Materials, 1st Edition, B. Verlinden, J. Driver, I. Samajdar, and R. D. Doherty, Alternative Deformation Mechanisms, pp. 121-123, (2007), with permission from Elsevier.

The mechanism in which twin boundaries propagate through a material is through twinning dislocation motion. A twinning dislocation is a partial dislocation containing a Burgers vector parallel to the interface plane K_1 [30]. The Burgers vector of a twinning dislocation is smaller than a lattice vector. A twinning dislocation creates a step height equal to the d-spacing of the twinning planes; see Figure 3.12. An applied stress, referred to as the twinning stress, will cause a dislocation to glide along the twinning plane. As a

twinning dislocation propagates through the material, one crystal grows at the expense of the other. Because the Burgers vector is parallel to the glide plane of the dislocation, the dislocation can move along the twin boundary without requiring diffusion [28].

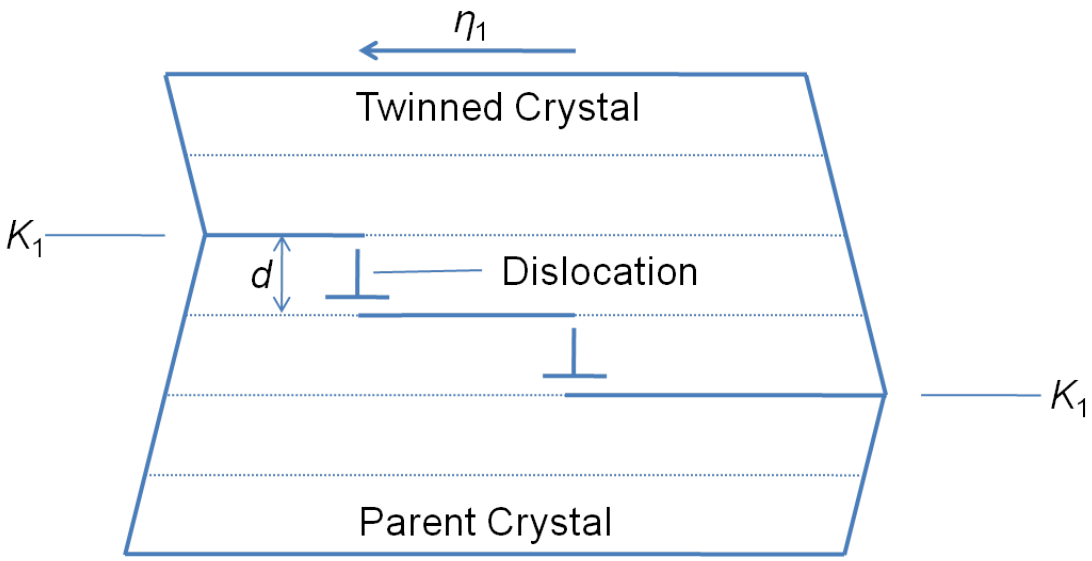

Figure 3.12 Schematic of twinning dislocations propagating through a material. As the twinning dislocations move to the left along the shear direction, the twinned matrix grows at the expense of the parent matrix. A dislocation creates a step height in the twinning plane. The twinning plane, K_1, is the interface between the two matrices.

3.3 Ferromagnetic Shape Memory Alloys

3.3.1 Magnetic Field Induced Twinning

During martensite transformation, the crystal forms a very complex microstructure in order to accommodate for internal strains and twins form within the martensite variants [31]. There are a number of different types of twins that have been observed in martensite Ni-Mn-Ga, including type I, type II, and compound twins; see Figure 3.13 [32, 33]. Type I twins exhibit relatively higher twinning stresses (~1 MPa) that are dependent on temperature and the austenite start temperature, while type II twins

exhibit lower twinning stresses (~0.2 MPa) and a nearly constant twinning stress over a wide range of temperatures [34, 35]. The relative angle between type I and type II twins is approximately 7° [33]. This is because the type II K_1 plane is irrational. The type I twins are reflections about a mirror plane while the type II twins are 180º rotations about the shear direction.

In addition to temperature induced phase changes, FSMAs are also reactive to mechanical stress and applied magnetic fields [36, 37]. In a highly twinned crystal with magnetic anisotropy, the magnetic moments are aligned in a zigzag pattern according to the twinned microstructure. In an applied magnetic field, the magnetic moments will align with the magnetic field and become misaligned with the easy axis of magnetization of the crystal structure. This results in an increase in the energy of the crystal. The energy difference between the two states will apply a driving force on a twin boundary; see Figure 3.14. If the driving force is larger than the twinning stress, the twin boundary will move, resulting in plastic deformation. The maximum strain, ε, for a martensitic single crystal is related to the length of the lattice parameters: $\varepsilon = 1 - c/a$.

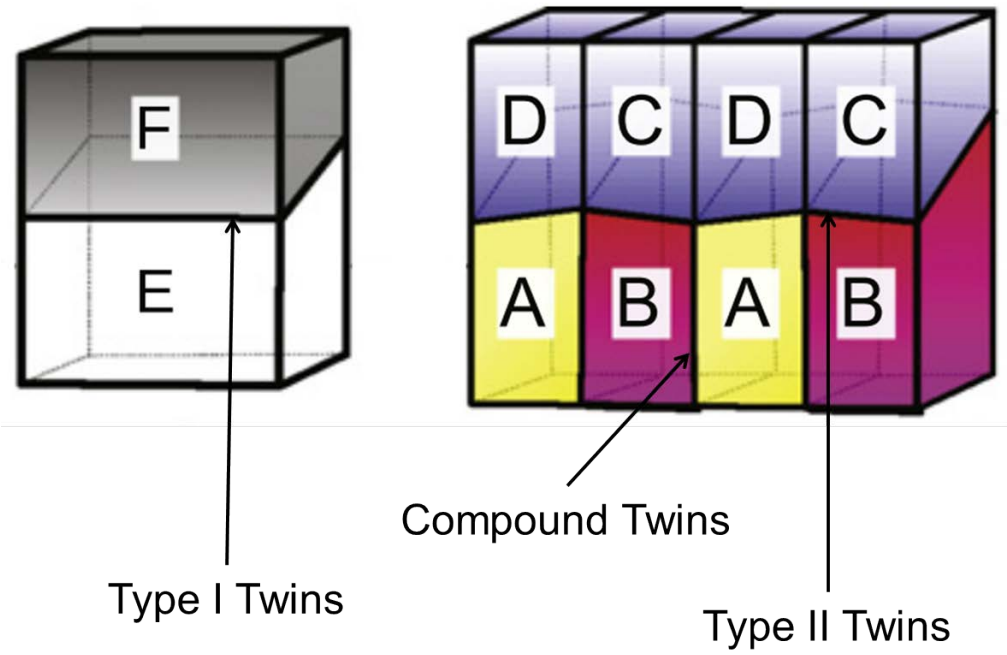

Figure 3.13 Diagram representing the three different types of twinning occurring in Ni-Mn-Ga martensite. Type I twin boundaries are parallel to the <100> directions. Type II twins deviate from <100> directions by approximately 7^0. Compound twins are mirror planes reflecting the modulation direction of the crystal structure. Reprinted from Acta Materialia, 59, L. Straka, O. Heczko, H. Seiner, N. Lanska, J. Drahokoupil, A. Soroka, S. Fähler, H. Hänninen, and A. Sozinov, Highly mobile twinned interface in 10M modulated Ni-Mn-Ga martensite: Analysis beyond the tetragonal approximation of lattice, pp. 7450-7463, (2011), with permission from Elsevier [33].

The shape change is diffusionless, resulting in extremely fast actuation response and can be cycled with frequencies as high as 2 kHz, resulting in complete field induced strain in as little as 250 μs [38]. If the magnetic field is removed, the martensite variants will remain in their current state. In order to reorient the crystal structure and change the shape of the material, the magnetic field would have to be rotated by 90° relative to the previously applied field [39]. There are usually many twin variants that contribute to the overall shape change and variants will either nucleate or be eliminated when exposed to an external stress.

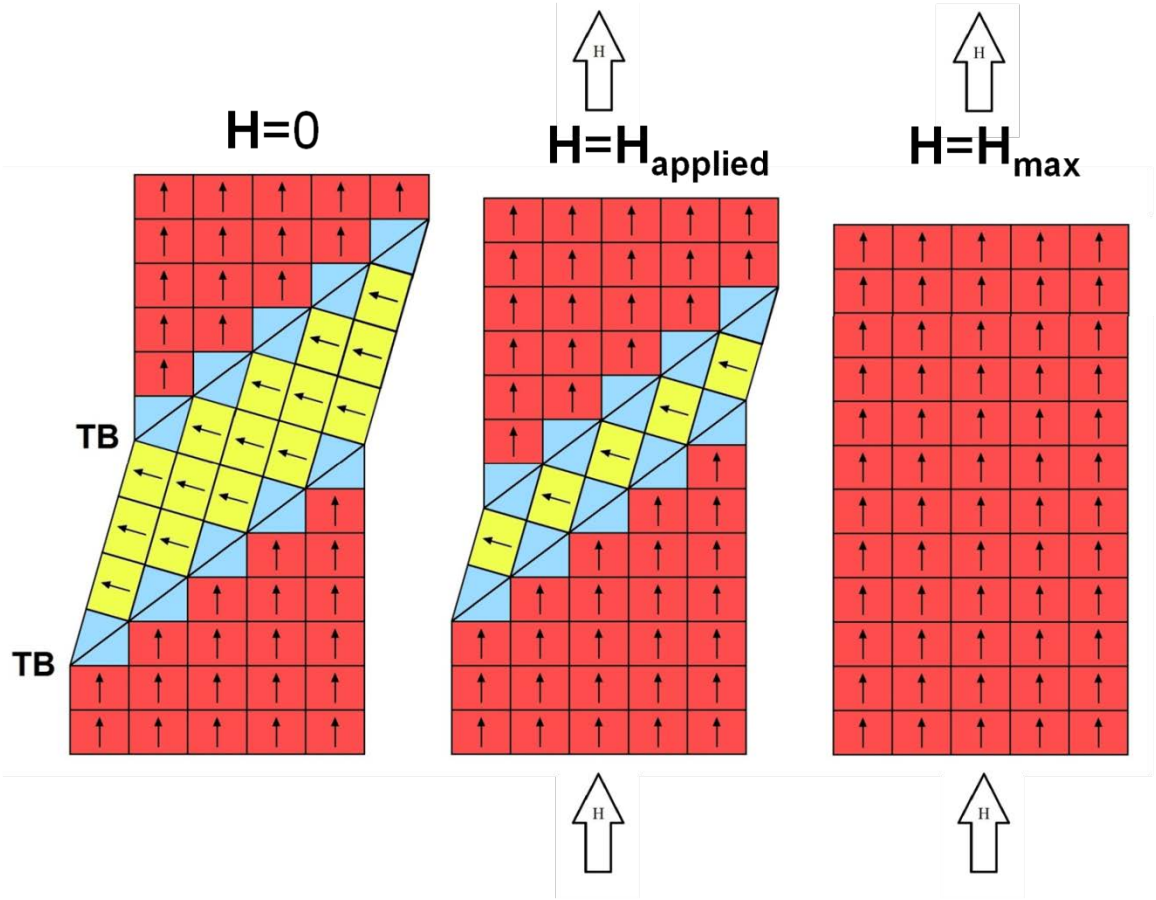

Figure 3.14 Conceptual diagram representing martensite twin variant reorientation in an applied magnetic field. The white arrows represent an applied magnetic field. The initial state (left) contains a large twin with two different variants, yellow and pink. The two diagonal lines within the blue region represent the twin boundaries. The easy axis of magnetization, represented by the small arrow within the unit cell, will preferentially align parallel with an increasing magnetic field (middle), causing the pink variant to grow at the expense of the yellow variant. At a sufficiently high magnetic field (right), the yellow variant will disappear as the structure reorients into a single variant.

3.3.2 Magnetostress

Numerous theoretical models have been proposed to describe the deformation of ferromagnetic martensite that focus on the thermodynamic analysis of the MFIS [10, 40-42]. L'vov et al. developed a phenomenological model to describe the changes in magnetic properties of ferromagnets within the martensite phase referred to as the phenomenological magnetoelastic model [43, 44]. The inhomogeneous strains that

become present in the martensite phase cause the changes in magnetic properties. It was shown that the magnetocrystalline anisotropy of the martensite phase exceeds that of the austenite phase. Therefore, the inhomogeneous strains govern the magnetization of martensite. A model of L'vov from [45] is based on the framework of the phenomenological magnetoelastic model for crystals containing two variants with different orientations. The model is based on the Gibbs potential of a cubic crystal expressed as

$$G = F_e + F_m + F_{me} - \frac{1}{6}(\sigma_2 u_2 + \sigma_3 u_3) \tag{3.4}$$

where

$$u_2 = \sqrt{3}(\varepsilon_{xx} - \varepsilon_{yy}) \tag{3.5}$$

$$u_3 = 2\varepsilon_{zz} - \varepsilon_{yy} - \varepsilon_{xx} \tag{3.6}$$

$$\sigma_2 = \sqrt{3}(\sigma_{xx} - \sigma_{yy}) \tag{3.7}$$

$$\sigma_3 = 2\sigma_{zz} - \sigma_{yy} - \sigma_{xx} \tag{3.8}$$

where σ_{ii} and ε_{ii} are strain and stress tensor components, respectively. The coordinate axes *x*, *y*, and *z* are oriented along [100], [010], and [001], respectively. When $\sigma_{ii} < 0$, the stress state is in compression and when $\sigma_{ii} > 0$ the stress state is in tension. The first term, F_e, on the right in Eq. (3.4) is the Helmholtz free energy of strains and expresses the ordinary elastic energy of a cubic crystal. The second term in Eq. (3.4), F_m, is the free energy of the magnetic subsystem of the crystal. The third term in Eq. (3.4), F_{me}, describes the relationship between the magnetic vector and the diagonal strain components.

From the Gibbs potential, Chernenko and L'Vov derived the effective magnetostress as a function of magnetic field expressed as

$$\sigma^{eff}(H) = \begin{cases} 12\delta_1 M^2 H^2/H_S^2, & H < H_S \\ 12\delta_1 M^2, & H \geq H_S \end{cases} \quad (3.9)$$

where δ_1 is the magnetoeleastic constant and H_S is the magnetic saturation field [45-47]. The magnetic saturation field is the point at which the magnetization of a sample no longer increases in an increasing applied magnetic field because all magnetic moments are perfectly aligned with the magnetic field [47]. This relationship is applicable to a two variant system with the easy axis of magnetization aligned in either the *x* or *y* axis. If a magnetic field is applied in the *x* direction, no stress will be imposed on the *x* variant because the easy axis of magnetization is parallel to the magnetic field so the magnetic dipole cannot be rotated by the field. An effective compressive stress will only be imposed on the second *y* variant because the easy axis of magnetization is perpendicular to the applied magnetic field. The maximum magnetostress is the maximum stress that a twin domain that is orthogonal to the applied magnetic field would experience in an applied magnetic field larger than the saturation field. The magnetic saturation field can be approximated by

$$H_S = 12|\delta(1 - c/a)|M_S \quad (3.10)$$

where *c* and *a* are lattice parameters, M_S is the saturation magnetization, and $\delta = \delta_1/M_S^2$ [48].

3.4 Ni-Mn-Ga

3.4.1 Heusler Alloys

In 1903, Heusler discovered that Cu_2MnAl exhibited ferromagnetic properties while the pure form of the elements Cu, Mn, and Al are all non-ferromagnetic [49]. X-Ray and neutron diffraction experiments have shown that Cu_2MnAl has the ordered $L2_1$ structure; see Figure 3.15 [50, 51]. Heusler alloys are ternary intermetallics with a

stoichiometry of X_2YZ. The X sub-lattice is occupied by a transition element and the Z sub-lattice is an element from the IIIA-VA groups of the periodic table. When the Y element is manganese, the resulting alloy is ferromagnetic. In 1960, Hames reported that Ni_2MnGa exhibited ferromagnetic properties associated with the ferromagnetic coupling of manganese atoms [52]. The austenite parent phase of Ni-Mn-Ga has the ordered face-centered cubic (FCC) $L2_1$ Heusler structure [53]. The magnetic and structural properties of Ni-Mn-Ga FSMAs depend strongly on composition [10].

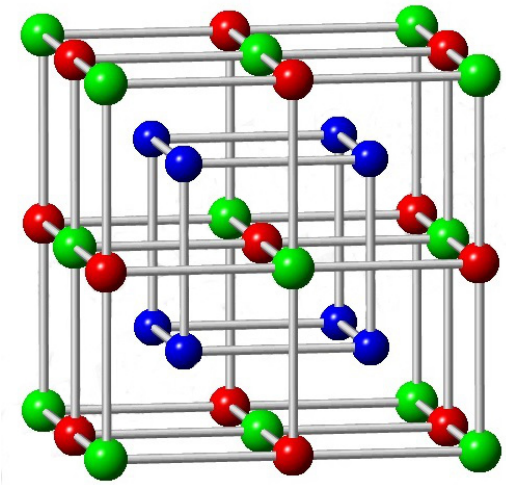

Figure 3.15 Ni_2MnGa $L2_1$ structured Heusler alloy. Manganese is located at the green sites, Gallium is at red, and Nickel is at blue. The austenite cubic phase is shown in this diagram.

3.4.2 Crystallography

Manganese occupies the eight corners of the unit cell as well as the 6 faces resulting in a face-centered cubic structure. Gallium occupies the sites in between the manganese atoms at the middle of each edge and in the center of the unit cell and also forms an FCC sub-lattice. Nickel atoms occupy the ¼,¼,¼ sites of the unit cell forming a cubic sub-lattice.

There are several martensite structures that will form upon cooling from the austenite phase depending on the composition of the alloy, the temperature, and external stresses [54]. The 10M and 14M structures exhibit a layered and modulated monoclinic crystal structure. The denotation of 10M and 14M comes from the stacking pattern of the structures and M refers to monoclinic. The non-modulated structure exhibits tetragonal symmetry.

Righi et al. have determined the 10M and 14M crystal structures to be monoclinic [55, 56]. However, the 10M and 14M structures are also referred to as pseudo-tetragonal and pseudo-orthorhombic, respectively. The 10M and 14M stacking sequences are $(\bar{3}2)_2$ and $(\bar{5}2)_2$ in Zhdanov notation, respectively [54]. This $(\bar{X}Y)_Z$ notation indicates the modulation of the structure's unit cell. The X indicates the number of atoms that are aligned in a certain direction, and the Y indicates the number of atoms that are aligned in a separate direction creating a zigzag pattern. The Z identifies the number of times that the stacking pattern is repeated in the unit cell. Thus, the 10M structure gets its name because the unit cell contains 10 layers of modulated atoms.

The austenite phase has a higher symmetry compared to the martensite structure. The martensite structure can form in a number of variants depending on the loss of symmetry of the structure. For example, if the unit cell of a martensite phase is tetragonal there are a total of three possible variants with the *c*-axis parallel to the [100], [010], or [001] directions. If the unit cell was orthorhombic, there are a total of six variants because there would be two unique orientations when the *c*-axis is parallel to [100], [010], or [001]. If the material is allowed to cool from austenite to martensite without any externally applied forces, the microstructure will be composed equally of each of the

possible variants. This is because the martensite phase will nucleate simultaneously at different parts of the crystal. This is known as self-accommodation and occurs because the orientation of the many variants produces an overall net distortion of zero. When the material is deformed, it is no longer self-accommodated because the variants become reoriented preferentially with the applied stress.

3.4.3 Magnetomechanical Properties

Ni-Mn-Ga exhibit MFIS when in the low temperature martensite phase [2]. The magnetic moments in Ni-Mn-Ga are coupled to the short *c*-axis of the unit cell and easy axis of magnetization [57-62]. The *c*-axis preferentially reorients to align with the magnetic field. The shape change is diffusionless, so the atoms shift in order to accommodate an imposed strain. This means that shape memory effect can be induced without heating and cooling the material, which allows for faster actuation responses with strains as high as 9.6% for Ni-Mn-Ga alloys [63]. Ni-Mn-Ga based alloys with small additions of copper and cobalt have even been found to exhibit strains as high as 12% [4]. See Figure 3.16 for a comparison of various actuator performances, including actuation response and elongation.

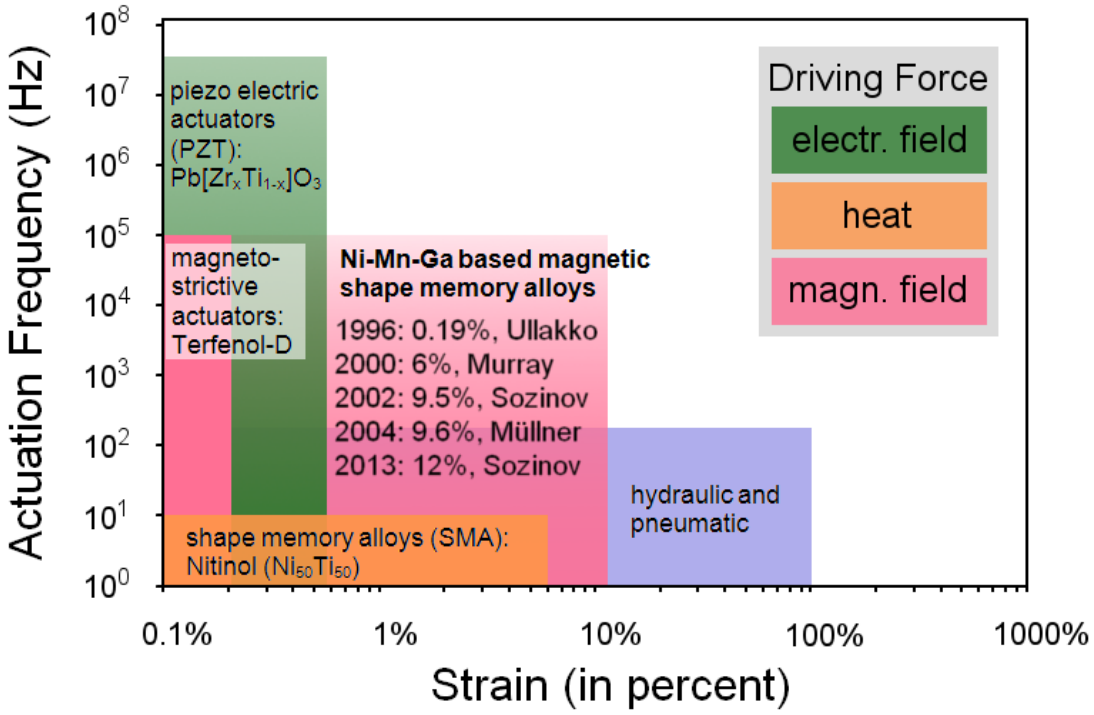

Figure 3.16 Diagram relating various actuator characteristics. FSMAs are attributed with high actuation response and large strain. Common actuators are typically associated with having either a large strain potential or high actuation frequency, but Ni-Mn-Ga exhibits both of these traits [2, 4, 58, 63, 64].

The highest twinning strain measured at room temperature for the 10M structure is 7.1% [12]. The 14M structure exhibits strains as high as 10.6% [13]. The non-modulated (NM) tetragonal martensite exhibits strains as high as 20.5% [65]. If the martensite transformation temperature is higher than the Curie temperature, the NM structure will be present, and when the transformation temperature is below the Curie temperature, the 10M or 14M can be observed [66]. This thesis utilizes samples with a 10M martensite structure because it has the lowest twinning stress requiring smaller magnetic fields to produce MFIS.

3.4.4 Fatigue and Fracture Mechanics

Müllner et al. performed the first high cycle testing on 10M and 14M single crystals [67, 68]. The samples were trained by heating into the austenite phase and

cooling with a constant compressive stress parallel to the [010] direction. This was done to prevent self-accommodation of martensite and allow the material to cool into a single martensite variant in the case of the 10M structure. The 14M structure, however, forms a minimum of two martensite variants because the unit cell is pseudo-orthorhombic. It has been shown previously that Ni-Mn-Ga alloys characterized with low twinning stress required a higher stress to initiate twin boundary motion in a sample containing a single variant than in a crystal containing twin boundaries, but the strain is highest in a single variant single crystal [69].

The test set-up for the fatigue tests in [67] involved rotating a magnetic field around a stationary sample in the (100) plane with the sample attached to strain gauge. A thermo-mechanical treatment was applied to the samples at the beginning of the tests and after 1000 cycles. The 10M sample exhibited a repeatable maximum strain throughout testing because only two possible martensite variants can be present during fatigue cycling, allowing for a clear twin boundary motion path. The 14M sample exhibited a decrease in strain with increased cycling prior to the second thermo-mechanical treatment. This is due to the twin structure changing with each cycle and the interaction of twinning dislocations preventing twin boundary motion. The maximum strain in the 10M and 14M sample increased with an increased number of cycles when a second thermo-mechanical treatment was performed [67]. Because the 10M structure is more stable throughout fatigue cycling, it was chosen for the experiments in this thesis.

The amount of training that is performed on an actuator element is a factor that affects the performance of FSMAs [19, 70]. Thermo-mechanical training was mentioned previously where a stress is applied while cooling into the martensite phase. The second

kind of training is magneto-mechanical where an actuator is cyclically deformed in two directions either by mechanical stresses, magnetic induced stresses, or both [67]. Samples with effective training performed prior to fatigue testing resulted in fewer than 100,000 cycles of magneto-mechanical cycles prior to failing, however the maximum initial strain was near the theoretical limit [19, 39]. Effectively trained samples contain a few twins and minimal self-accommodation resulting in large strains that are increased through magneto-mechanical cycling. Samples with no prior training were cycled to beyond $10x10^6$ cycles with increasing strain due to magneto-mechanical cycling [19].

Sample constraint has been shown to have a significant impact on the overall performance of Ni-Mn-Ga actuators [19, 71]. Chmielus et al. showed that a 10M sample constrained on both ends with super glue exhibited a strain of 0.6%, but when the sample was only constrained on one end and a decoupler was used on the other end the strain increased to 2.7% [71]. In a sample that has been trained into a single variant with constraints on either end, multi-variant twins will nucleate near the constraints. As the sample is cycled, mobile twins will interact with the constrained twins causing localized stress that leads to fracture. In samples that are untrained and contain many thin twins, the microstructure will remain relatively unchanged at the constrained portion of the sample while the unconstrained portion of the sample will become trained or develop into a few mobile twins. In another study, it was shown that internal constraints affect performance through the synthesis and analysis of a porous Ni-Mn-Ga structure. The porous structure allows for single crystal like strain responses as high as 8.7%, a value that is much higher than any previously recorded MFIS in polycrystalline Ni-Mn-Ga [7]. This occurs because each of the struts that connect the pores acts like a single crystal due

to the thickness of the strut being smaller than average grain size. For maximum MFIS, constraint should be kept to a minimum.

Another method used for fatigue testing is linear actuation. Aaltio et al. used a linear actuator to induce an oscillating mechanical stress with up to 2% strain, achieving $2x10^9$ fatigue cycles for 10M single crystals [17]. Larger induced strains and higher actuation frequency lead to lower fatigue life [18]. The experimental setup used in these experiments was purely mechanical in that an actuator was used to cycle the deformation of the sample uniaxially with frequencies ranging from 75-344 Hz. The range in strain measured in these tests was 0.5-3.8%, so it is less than the maximum strain reported in the 10M single crystals used at 6.5% [17, 72]. When a constant strain of 2% was implemented, it was found that the twinning stress increased up to 1.6 MPa after cycling up to 900×10^6 times; see Figure 3.17 [17]. This means that the material is hardening and it requires a higher stress in order to actuate at higher cycles.

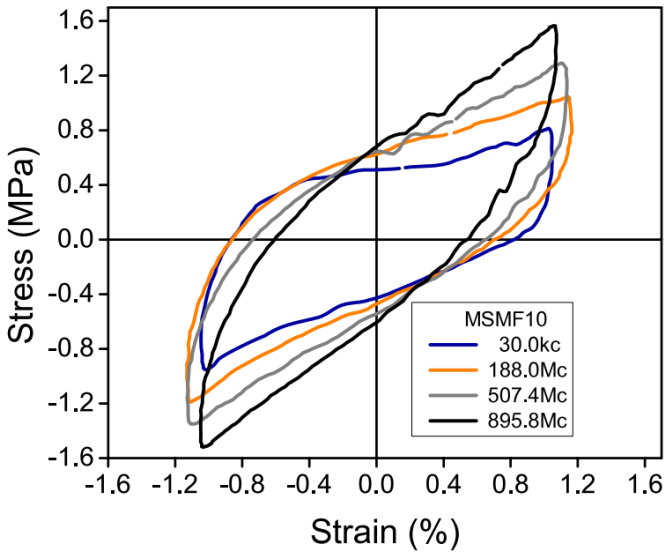

Figure 3.17 Progression of stress vs. strain loops for a Ni-Mn-Ga sample actuated to nearly 1×10^9 cycles. The maximum stress achieved increases from approximately 0.8 MPa to 1.6 MPa over the course of testing. Reprinted with kind permission from [17].

CHAPTER FOUR: EXPERIMENTAL

The fracture mechanics and fatigue life of 10M Ni-Mn-Ga single crystal samples were investigated through rotating field testing. The 10M crystal structure was selected because it exhibits the lowest twinning stress for Ni-Mn-Ga. The twinning stress is related to the magnetic field required to reorient the microstructure. Samples were individually characterized and cycled to fracture. The samples were analyzed throughout cycling to document crack propagation and measure the effects of fatigue life on material properties.

4.1 Single Crystal Growth

Oriented Ni-Mn-Ga single crystals were grown via the Bridgman-Stockbarger technique. 99.999% nickel, 99.9999% gallium, and 99.99% manganese were the high purity metals used in casting master alloys and final alloys. Nickel, manganese, and gallium have melting temperatures of 1455 ˚C, 1246 ˚C, and 29 ˚C, respectively. The low melting temperature of gallium helps bring the melting temperature of the alloys down below 1200 ˚C, the temperature at which the melt was held at throughout growth.

4.1.1 Master Alloy and Final Alloy Casting

The initial master alloy elements were weighed out so that the nominal composition would be 75.7 at-% nickel and 24.3 at-% gallium. Gallium was alloyed with nickel at this stage to lower the melting temperature of the alloy. Manganese was not yet added because it has the highest partial vapor pressure and tends to evaporate easily at high temperatures. The elements are added to an alumina crucible. The crucible was

placed in a fused silica quartz tube. The quartz tube was connected to a turbo pump vacuum assembly and evacuated to approximately 1 x 10^{-3} mbar. The system was then purged with argon to a pressure of 5 x 10^{2} mbar. The system was again evacuated to approximately 5 x 10^{-4} mbar and purged with argon to remove as much oxygen as possible to reduce oxidation. The Quartz tube was sealed off and transferred to a Reitel Induret Compact induction furnace. The alloy was heated to melting where it was held for 30 minutes to enable mixing. The heat of the furnace was manually adjusted to be high enough to enable mixing but also low enough to prevent extensive evaporation of manganese. The alloy was then left to cool in the open furnace to room temperature then crushed to a powder.

Manganese and additional gallium were then added to achieve a desired final alloy composition of $Ni_{51.2}Mn_{26.6}Ga_{22.2}$ at-%. The process for evacuating the crucible assembly, melting, and mixing the final alloy was identical to the master alloy process. A slice of the alloy was cut with a diamond wafer saw. The section was ground down to 1200 grit to prepare a flat surface for electron diffraction spectroscopy (EDS). Several EDS area and point scans were performed to verify the composition of the alloy. If the alloy composition was as expected, the alloy was crushed to a fine powder until the particles passed through a number 16 U.S.A. Standard Testing Sieve, with 1.18 mm openings. This powder was used in the growth of single crystals via the Bridgman-Stockbarger technique.

4.1.2 Single Crystal Growth via Bridgman-Stockbarger Technique

Large MFIS is generally attributed to single crystalline structure on account of grain boundaries inhibiting twin boundary motion. The MFIS is negligible in

polycrystalline alloys with extremely fine grains and random texture [73]. It is for this reason that single crystalline samples were used in the fatigue testing presented in this thesis. Ni-Mn-Ga single crystals of nominal composition $Ni_{51.2}Mn_{26.6}Ga_{22.2}$ at-% were grown in a modified MTI Corporation tube furnace capable of temperatures as high as 1400 ˚C. The melting temperature of stoichiometric $Ni_{50}Mn_{25}Ga_{25}$ is 1109 ˚C with the melting temperature ranging from 1073 ˚C to 1122 ˚C for compositions $Ni_{50}Mn_{35}Ga_{15}$ and $Ni_{50}Mn_{15}Ga_{35}$, respectively [74]. The composition was chosen based off of previous results from crystals that yielded a large portion of 10M crystal structure (Figure 4.1).

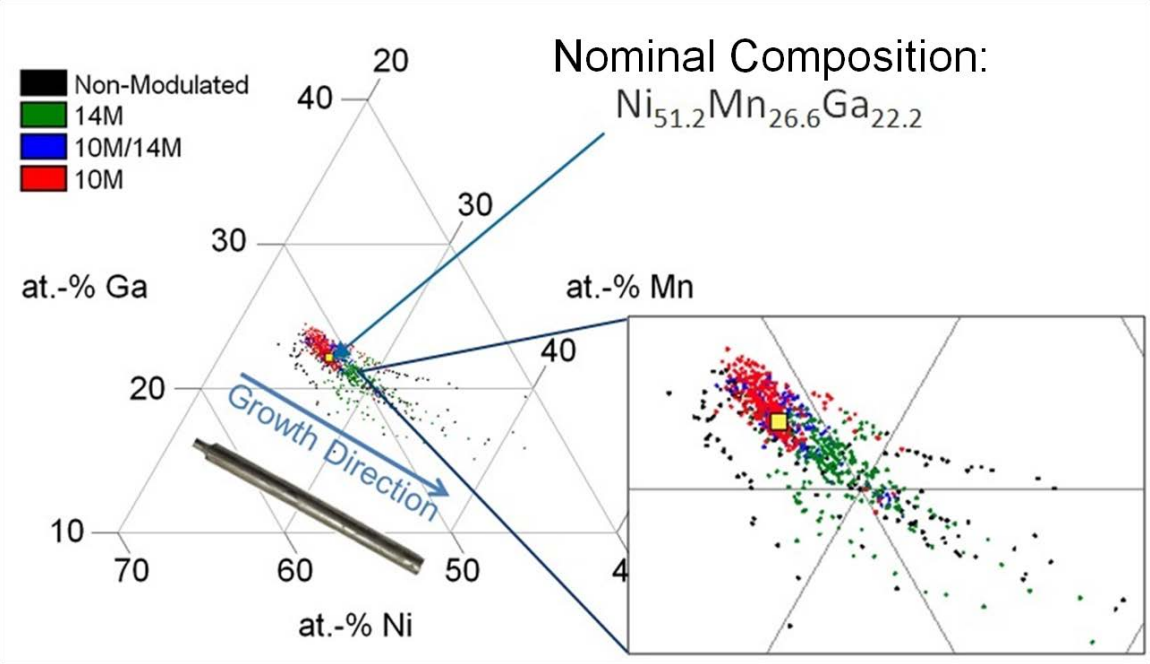

Figure 4.1 The target composition for the crystals used in the following experiments was 51.2% Ni, 26.6% Mn, and 22.2% Ga and was determined based off of previous results that yielded large sections of the desired 10M martensite structure. This ternary diagram contains EDS and XRD data from 31 crystals of varying composition. EDS and XRD data was taken along the length of each crystal every 2 mm and plotted here.

The crushed Ni-Mn-Ga powder was weighed out and placed in a growth assembly; see Figure 4.2 [75]. The assembly consisted of a hollow copper rod, hollow

steel rod, seed holder, single crystal seed, 6 mm inner diameter alumina tube, and fused quartz tube. The rods acted as spacers to position the single crystal seed and powder as well as act as a heat sink to draw heat from the Ni-Mn-Ga seed. The smaller steel rod was placed next to the seed because it has a higher melting point than copper. Copper was used for the bottom rod because of its high thermal conductivity.

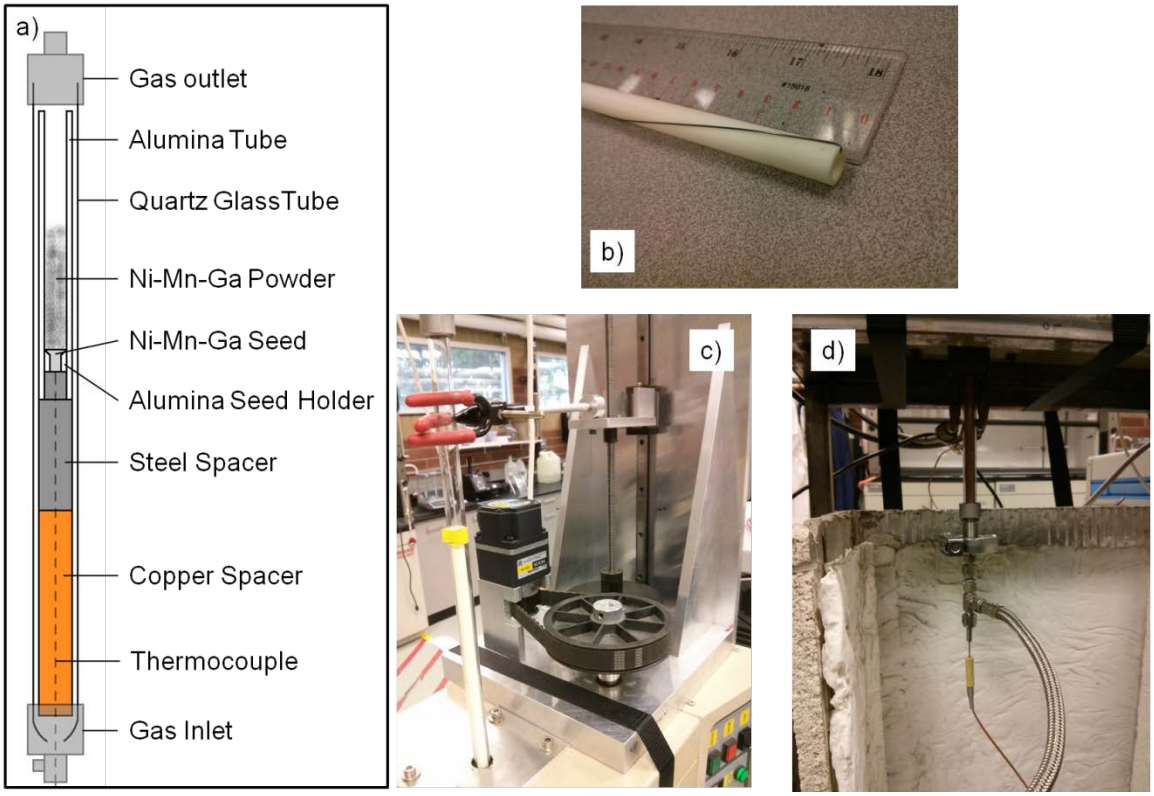

Figure 4.2 Single crystal growth assembly. a) Schematic of the single crystal growth assembly (not drawn to scale). The tantalum wire that separates the quartz tube from the alumina tube is not shown. b) Tantalum wire wrapped around alumina tube. c) The assembly used to drive the single crystal into and out of the hot zone. d) The bottom of the single crystal assembly showing the gas inlet adapter and the thermal couple inserted through the assembly.

The single crystal Ni-Mn-Ga seed was placed in an alumina seed holder and pushed into the alumina assembly tube with the steel spacer. To prevent reaction of quartz and α-alumina at temperatures below 1100 ˚C, a tantalum wire was wrapped around the alumina tube as a spacer between the alumina and quartz [76]. The assembly

was placed in the fused quartz tube and slid through the tube furnace. A finger clamp was used to attach the assembly to a linear actuator located on top of the furnace. Machined aluminum heat sinks were positioned on the outside of the quartz tube at the openings of the furnace. The top and bottom of the quartz tube were connected to a vacuum and inert gas purging system. A thermocouple was inserted through the bottom vacuum system connector until the tip of the thermocouple touched the bottom of the Ni-Mn-Ga seed. The temperature of the bottom of the Ni-Mn-Ga seed was monitored with this thermocouple throughout the growth process.

A copper cooling jacket was located at the bottom of the furnace to create a thermal gradient that will aid in the growth of a crystal. Again copper was used for its high thermal conductivity. A water-glycol mixture at a temperature of 18 °C was circulated through the copper cooling jacket. The temperature of the cooling jacket face was 23 °C when the temperature of the hot zone was at 1000 °C. The assembly was positioned inside the furnace so that the seed and crushed powder were below the hot zone of the furnace. The system was evacuated to a pressure of 1×10^{-2} mbar. The furnace was set to 1200 °C and the assembly was driven into the hot zone at a speed of 0.56 mm/min. When the thermocouple at the bottom of the seed reached a temperature of 850 °C, the assembly was stopped. At this point the powder and top part of the single crystal seed were molten. The assembly was now driven down at a speed of 0.08 mm/min. The vacuum pump was stopped and $Ar/H_2(6\%)$ was introduced and allowed to flow through the system at a rate of approximately 1 standard cubic feet per hour (SCFH) during the growth of the crystal. $Ar/H_2(6\%)$ was used to prevent oxidation at high temperature by purging oxygen from the system and any remaining oxygen reacts

with the hydrogen. As the crystal exited the hot zone, the solid-liquid interface traveled from the tip of the seed to the top of the crystal.

4.1.3 Annealing

In order to obtain a highly ordered structure, a long term heat treatment is necessary [77]. After the crystal exited the hot zone and had completely solidified, the temperature of the furnace was reduced to 950 ˚C. The Ar/H_2(6%) gas was switched to pure argon to reduce hydrogen embrittlement of the crystal during annealing. The crystal was raised back into the hot zone to anneal for 48 hours. The temperature was then further reduced to 750 ˚C and the crystal was left to anneal for 12 hours. The first annealing step aids in homogenization of the crystal and the second step aids in short-range ordering [75]. The furnace was then turned off and the crystal was cooled to room temperature in the furnace with the argon flowing continuously.

4.2 Characterization

The crystals were characterized using a number of methods including X-Ray Diffraction (XRD), Energy Dispersive X-Ray Spectroscopy (EDS), Vibrating Sample Magnetometer (VSM), compression testing, and optical profilometry. These characterization methods were used to determine crystallographic structure and orientation, composition, magnetic properties, mechanical properties, and surface roughness, respectively. These methods will be described in detail below.

4.2.1 X-Ray Diffraction (XRD)

A Bruker D8 Discover X-Ray Diffractometer with a Cu Kα source and area detector was used in determining the crystallographic structure, orientation, and lattice parameters of single crystals; see Figure 4.3. Incident x-rays will interact with the atoms

in the surface layers of a material. When the atoms occupy a periodic structure, constructive interference of scattered radiation occurs in certain directions. There will be an increase in the intensity of the x-rays reaching the detector due to coherent interference when the Bragg condition is met. The Bragg condition is met when

$$n\lambda = 2dSin\theta \tag{4.1}$$

where n is an integer, λ is the wavelength of the x-ray, d is the spacing between crystal planes, and θ is the angle between the incident x-ray and the lattice plane. Destructive interference occurs when the Bragg condition is not met. XRD scans allow for the measurement of plane d-spacing by simply measuring the angle at which diffraction occurs and by knowing the wavelength of the x-ray source.

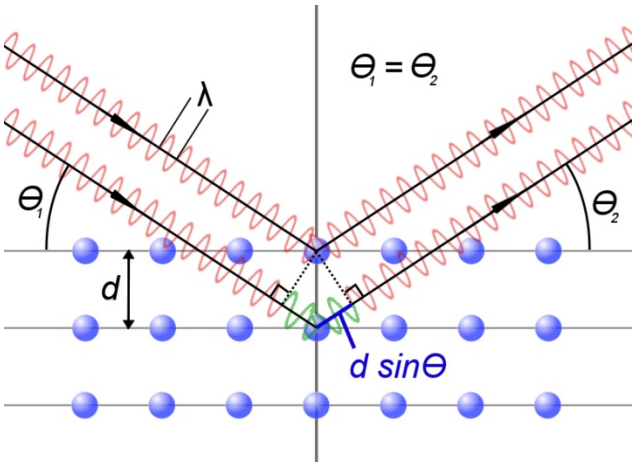

Figure 4.3 Coherent interference of incident x-rays will occur when the Bragg condition is satisfied, nλ = 2d sinΘ. This will only occur at specific angles that depend on the periodic structure of the material.

Polycrystalline materials contain many randomly oriented grains, which make it easy to perform XRD on because the incident beam will always satisfy the Bragg condition with some grains. With a single crystal, this is not the case. The crystal must be specifically oriented in order to satisfy the Bragg law. The crystals were grown with the [001] direction parallel to the long axis of the crystal. The crystals were rotated about the

long axis of the crystal incrementally and scanned until the signal intensity of the {400} peaks was maximized; see Figure 4.4. XRD scans were taken along the length of the crystal in 2 mm increments to determine the crystal structure. Each scan consisted of rotating and simultaneously oscillating the sample. The 2θ angle was set to 64° because the {400} planes were used in determining the crystal structure. All of the {400} peaks for the various Ni-Mn-Ga structures fall within the range of the area detector at this angle. Peak positions were determined at the highest intensity of the peak with an error of $\pm$ 0.01°. The scans were analyzed to determine the crystal structure based off of diffraction patterns created in CrystalMaker software.

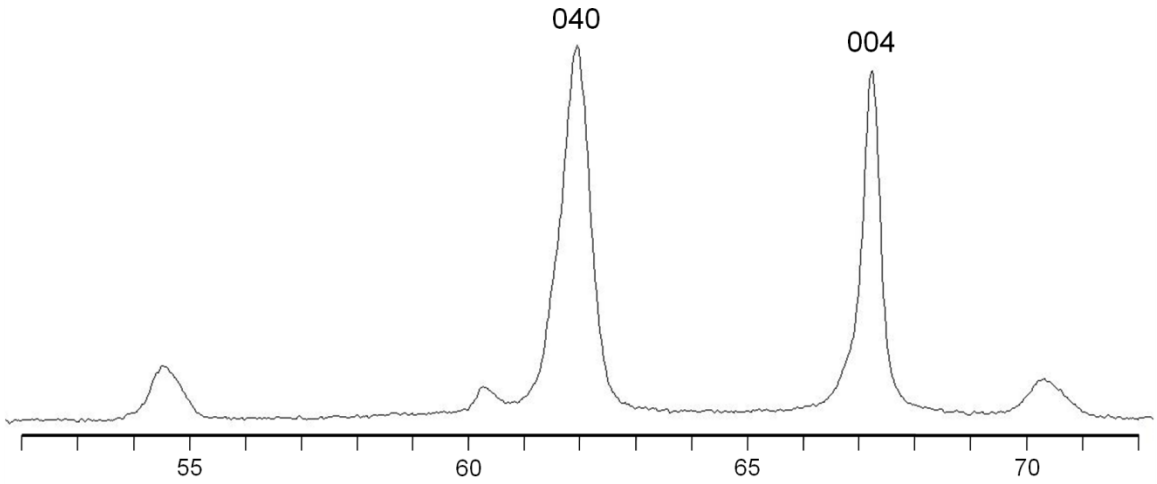

Figure 4.4 XRD scan of 10M Ni-Mn-Ga single crystal. Crystal was oriented such that the [004] was parallel to the stage plane and the [040] was normal to the stage plane.

4.2.2 Energy Dispersive X-Ray Spectroscopy (EDS)

The composition of the final alloys and single crystals were measured in a Hitachi S-3400N Scanning Electron Microscope (SEM) equipped with an Oxford X-Max 50mm^2 EDS detector. The Hitachi 3400N SEM utilized a Tungsten filament as an electron

source. When the electrons contact the bulk specimen, they are scattered throughout the sample. As they interact and bounce off of atoms in the specimen, they lose energy. Some electrons will lose enough energy to be absorbed into the material. Others will be scattered away from the surface; these are backscattered electrons. The primary incident electron can contain enough energy to eject an electron from the electron shell of an atom. When an electron from an outer electron shell moves to fill the missing electron in an inner shell, a characteristic x-ray is emitted. The energy of this x-ray is specific to the type of shell transfer of electrons as well as the type of atom. An EDS detector can be used to determine composition of elements in an alloy based on relative peak intensities.

The EDS detector was calibrated using a 99.999% nickel standard. A face was ground into the side of the crystal with 1200 grit SiC to obtain a uniform flat surface for scanning. The flat face was parallel to the (100) plane. An area EDS scan was performed every 2 mm along the length of the crystal to determine the composition. Figure 4.5 shows an example of a compositional EDS scan along the length of the crystal, including XRD data. The 10M portion of crystals was used in experiments.

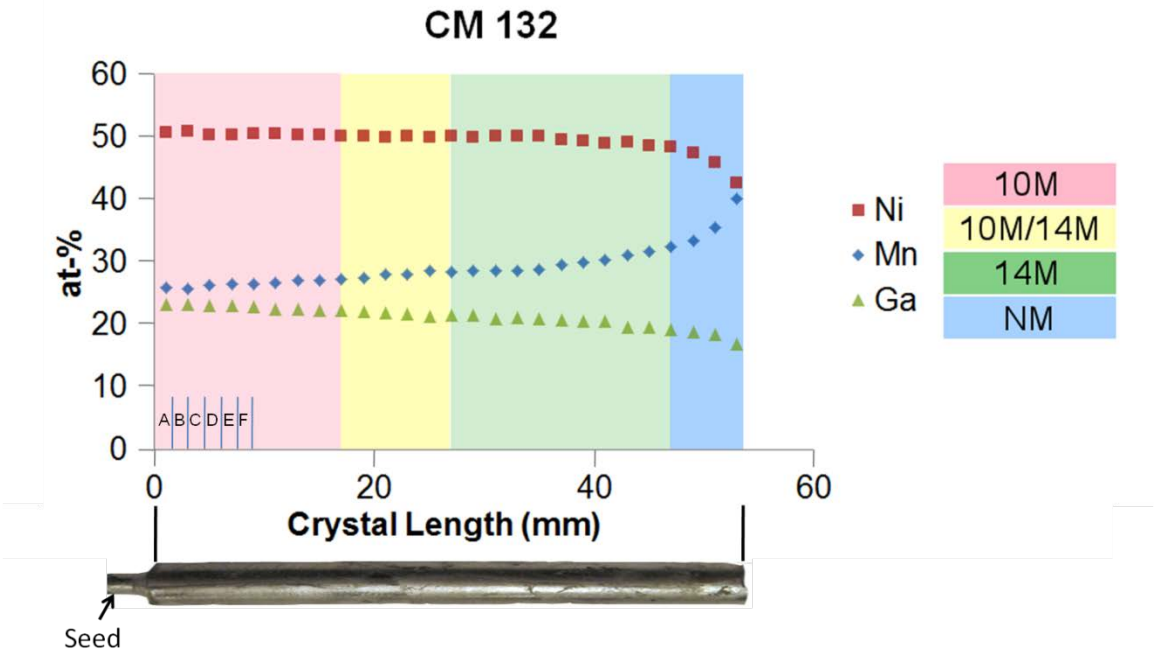

Figure 4.5 XRD and EDS diagram for CM132 a $Ni_{51.2}Mn_{26.6}Ga_{22.2}$ (at-%) single crystal used in fatigue testing. Data points represent crystal composition and shaded areas represent crystal structure. The face of the $(001)_S$ plane at crystal length 0 mm is the face that was exposed from cutting the seed off of the crystal. The data was obtained along the length of the crystal corresponding to the image of the crystal shown below the diagram. The letters in the bottom left corner of the diagram correspond to the locations of samples that were cut from the crystal. Reference Table A.3 for EDS and XRD pertaining to the other single crystals used in this thesis.

4.2.3 Sample Preparation

Five single crystals named CM132, CM142, CM143, CM154, and CM158 were used in rotary fatigue testing. The number in CMXYZ refers to the sequential growth number of a single crystal. The designation $[XYZ]_S$ or $(XYZ)_S$ will be used in this thesis to designate directions and planes related to the sample coordinate systems (Figure 4.6). See Table A.3 in the appendix for a list of all samples and their respective preparation method.

The seed was cut from the base of the crystal with a Princeton Scientific precision wire saw to expose a face parallel to $(100)_S$. The wire saw was used to cut cylindrical

wafers with an approximate thickness of 1.5 mm and a 6 mm diameter along the length of the 10M portion of the crystal. The location of samples cut from their respective single crystal is indicated in the bottom left corner of Figure 4.5 and Figures A.1-A.3 in the appendix. The complete list of samples used in testing is provided in Table A.3 in the appendix. The wafers were cut along the {001} plane normal to the <001> growth direction of the cylindrical crystal; see Figure 4.6. 45 samples were mechanically polished with SiC and water down to 4000 grit then diamond slurry polished down to 3 µm using a Struers LaboPol. Three samples were further polished down to 1 µm and 5 were polished down to 0.04 µm. 10 samples were electropolished in a solution of 17 ml of nitric acid and 33 ml of methanol. The power supply settings were set to 15 volts and 1 amp. The temperature of the solution was cooled to -20 °C using liquid nitrogen. The samples were submerged for 30 seconds.

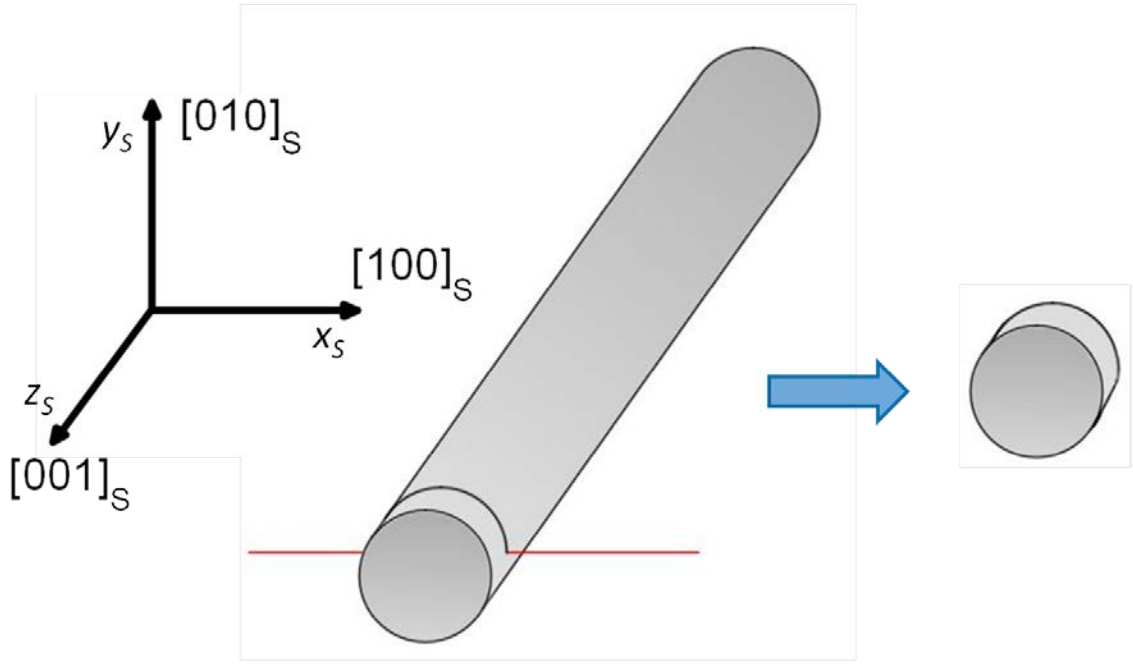

Figure 4.6 Cylindrical wafers were cut along the (001) plane for fatigue testing using a Princeton Scientific wire saw. The coordinate axes indicate the sample coordinate system.

1 ± 0.2 mm notches were introduced to six mechanically polished samples and five electropolished samples using a Princeton Scientific precision wire saw. A notch was introduced in the $[100]_S$ direction and are in the $[110]_S$ direction on each of the eleven samples; see Figure 4.7.

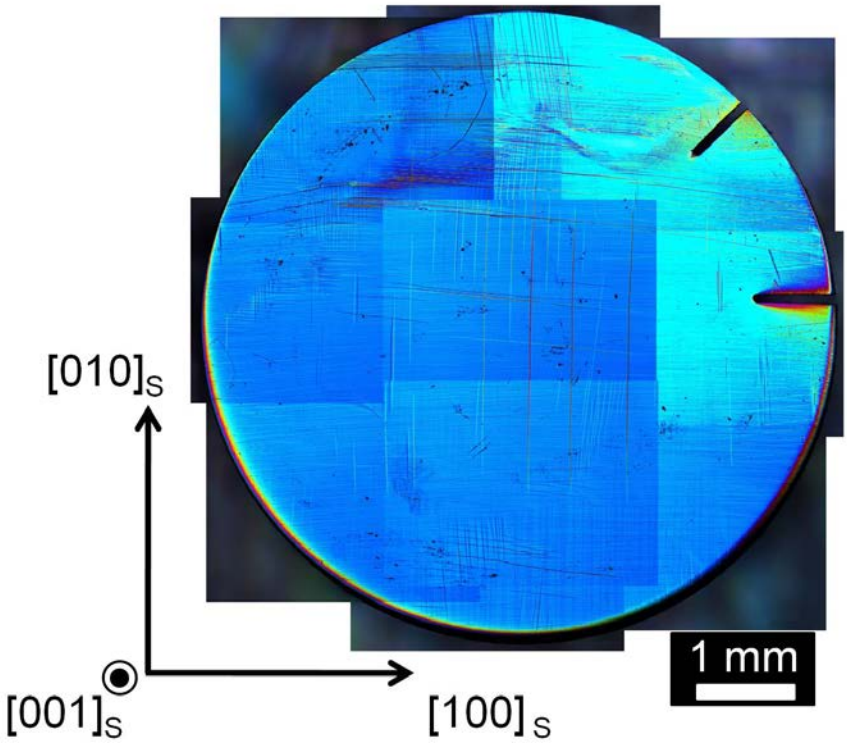

Figure 4.7 DIC mosaic image of a sample notched with a Princeton Scientific precision wire saw in the $[100]_S$ and $[110]_S$ directions to control fatigue crack initiation points.

Magnetomechanical training was effectively performed on the fatigue samples through measuring the magnetic properties of the samples in different orientation. The procedure for testing for these properties is discussed in the next section. After training, the samples were predominantly a single martensite variant.

Rectangular samples were cut from the 10M portion of an additional single crystal, CM161, to be used in compression experiments to determine the twinning stress

for the specified composition of $Ni_{51.2}Mn_{26.6}Ga_{22.2}$ (at-%). The five samples used in testing were named A1-C1. The samples were cut so that the {100} (austenite) planes were parallel to the sample faces. The faces of the samples were mechanically polished to 1 μm.

4.2.4 Vibrating Sample Magnetometer (VSM)

Prior to fatigue testing, each cylindrical sample was tested to analyze its magnetic properties in a vibrating sample magnetometer (VSM) DSM Model 10; see Figure 4.8. The VSM measures the magnetization of a sample by vibrating the sample in between a pair of pickup coils at a frequency of 75 Hz, inducing a voltage in the pickup coils according to Faraday's law. The instrument was calibrated prior to making measurements by using a Nickel standard with a known magnetization of 54.9 emu/g. The induced voltage can then be converted into magnetization because the change in voltage is proportional to the change in magnetic flux density.

Phase transformation and magnetic properties of samples from each crystal were measured in the VSM by recording the magnetization as a function of temperature with an applied magnetic field of 0.02 MA/m. This was done by heating a sample with proportional integral derivative (PID) controlled resistively heated air at a rate of 3.7 °C/min to a temperature of 130 °C. The sample was then cooled with nitrogen gas back down to a temperature of 20 °C.

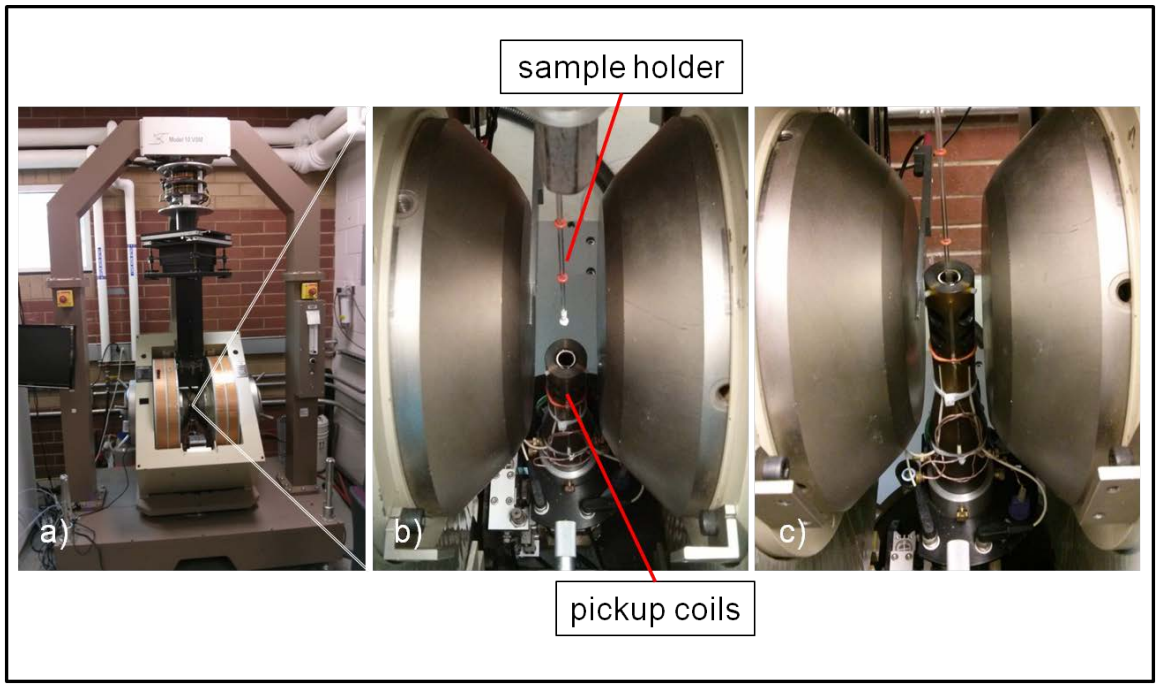

Figure 4.8 a) Vibrating Sample Magnetometer. b) Sample holder shown in between electromagnetic poles with the pickup coils lowered. c) Pickup coils raised and now surrounding the sample.

Each fatigue sample was loaded into the instrument so that the $[010]_S$ direction was parallel with the applied magnetic field, and the $[100]_S$ direction was parallel to the sample holder rod. An increasing magnetic field up to 1.6 MA/m was applied parallel to the $[010]_S$ direction and the sample was magnetized to saturation. This is known as the virgin curve and indicates the saturation magnetization in a magnetic field. It is necessary because when cooled through the Curie temperature, a magnetic sample is demagnetized. If there are any twins in the sample, they will reorient so that the *c*-axis or easy axis of magnetization aligns with the applied magnetic field.

The magnetization of Ni-Mn-Ga will be highest if the crystal structure is completely homogeneous and the easy axis of magnetization of each unit cell is aligned parallel to each other. An increasing applied magnetic field perpendicular to the easy axis of magnetization will induce a stress on the magnetic moments of the material.

Eventually the magnetic field will cause the easy axis of magnetization of the crystal structure to become reoriented parallel with the magnetic field. The threshold magnetic field required to reorient the crystal structure is known as the switching field. When the reorientation occurs the magnetization increases discontinuously (Figure 4.9).

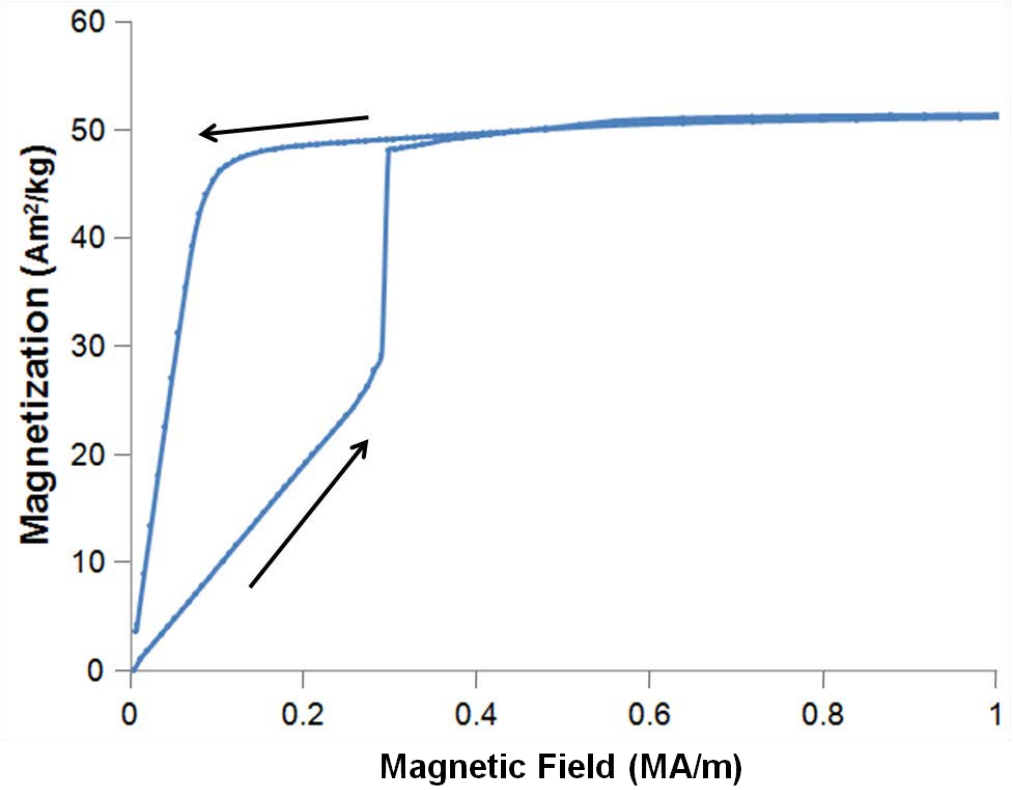

Figure 4.9 Switching field diagram for a cylindrical sample with the magnetic field applied parallel to the sample face. The sharp increase in magnetization correlates with the reorientation of the crystal structure. The arrows indicate the path of magnetization as the magnetic field is increased and subsequently decreased.

After measuring the virgin curve, the sample was then rotated by 90° so that the $[001]_S$ direction of the sample was aligned parallel to the direction of the applied magnetic field so that the magnetic field direction was perpendicular to the sample face. The switching field was measured by applying an increasing magnetic field up to 0.8 MA/m. The sample was then rotated back by 90° so that the $[010]_S$ direction was again aligned with the magnetic field, i.e. so the magnetic field was parallel with the sample

face. When the field was applied, the twins reoriented again and the switching field was measured in this orientation. In this way, the switching field was measured three times in each direction, effectively training the samples into mostly a single martensite variant. Switching field measurements were taken for every sample prior to fatigue testing. Switching field measurements were performed prior to fatigue testing and at intervals of 10,000 revolutions for samples CM154 J-O and Q.

4.2.5 Compression Testing

The designation $[XYZ]_{CT}$ or $(XYZ)_{CT}$ will be used to indicate directions and planes related to the compression sample coordinate systems (Figure 4.10). Five parallelepiped samples with dimensions approximately 2 mm x 3 mm x 6 mm were tested in uniaxial compression experiments. Compression tests were performed to measure the twinning stress. Prior to testing, the samples were magnetized along the short *x*-axis in the $[100]_{CT}$ direction of the crystal so that the easy axis of magnetization was parallel to the $[100]_{CT}$ direction and the crystal extended as much as possible in the $[001]_{CT}$ direction. The dimensions of the sample were measured before and after compression testing.

Samples were loaded into a Zwick compression testing instrument equipped with a 500 N load cell so that the long axis of the crystal or the $[001]_{CT}$ direction was parallel to the axis of compression. The samples were initially loaded to 0.05 MPa at a crosshead speed of 8.3×10^{-6} m/s to preload the sample. Mechanical compression testing was performed at a constant crosshead speed of 2×10^{-6} m/s until a maximum stress of 5 MPa was achieved. The samples were then unloaded at a constant crosshead speed of 4×10^{-6} m/s until a minimum stress of 0.05 MPa was reached. The resolution of the instrument

was better than 0.5 N in force and 10 nm in displacement. Three compression tests were performed on each sample. In between compression testing, a magnetic field was applied in the $[100]_{CT}$ direction to elongate the sample in the $[001]_{CT}$ direction for the next test.

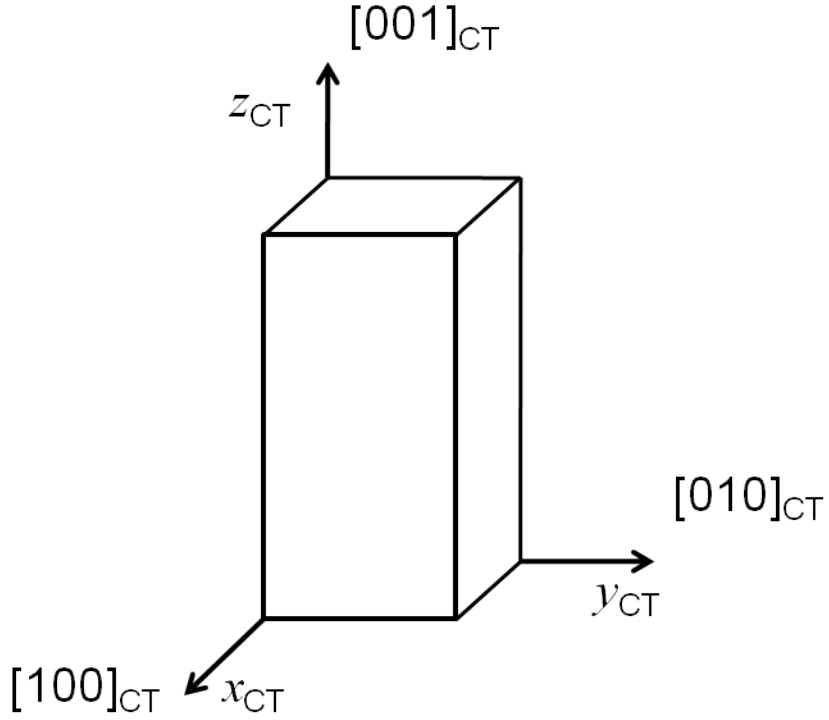

Figure 4.10 Schematic identifying the axes and associated directions of the compression samples. The shortest side of the crystal was designated as x_{CT} and the longest axis was designated as z_{CT}.

4.2.6 Optical Profilometry

The surface roughness of the rotary fatigue samples was measured using a Veeco Wyko NT1100 optical profilometer. An optical profilometer measures height differences in the topography of the surface over a defined area. A path of light is split in the instrument directing light towards a reference surface, which is made to be as flat as possible, and the test surface. The two beams reflect off of the two surfaces and recombine as the beam is focused towards a digital camera. The phase shift of the two beams is proportional to the path difference. Constructive and destructive interference

patterns from the two beams appear lighter and darker to the camera, respectively. The profiler scans the surface of the material vertically. The software identifies when a specific area is in perfect focus and contrast by analyzing the fringe patterns while scanning. With this information, a height map can be created for a specified area. Three measurements were taken per side for every single crystal and averaged. The measurements were taken within a single twin domain to ensure that the average surface roughness measurement was not taking the twin relief of multiple twin boundaries into account.

4.2.7 Differential Interference Contrast (DIC) Microscopy

DIC optical microscopy was used to image samples throughout testing. Polarized light and light wave interference emphasize differences in topography and slope of surfaces. Different twin domains have their own orientation and will reflect the light differently. Polarized light is split using a Nomarski prism and focused on the sample. Due to differences in topography, the length of the reflected beams will vary slightly compared to one another as they are combined back together at the Nomarski prism on the way to the eye piece or camera. Different polarizing filters can be used to adjust the contrast and colors that appear on the image; see Figure 4.11.

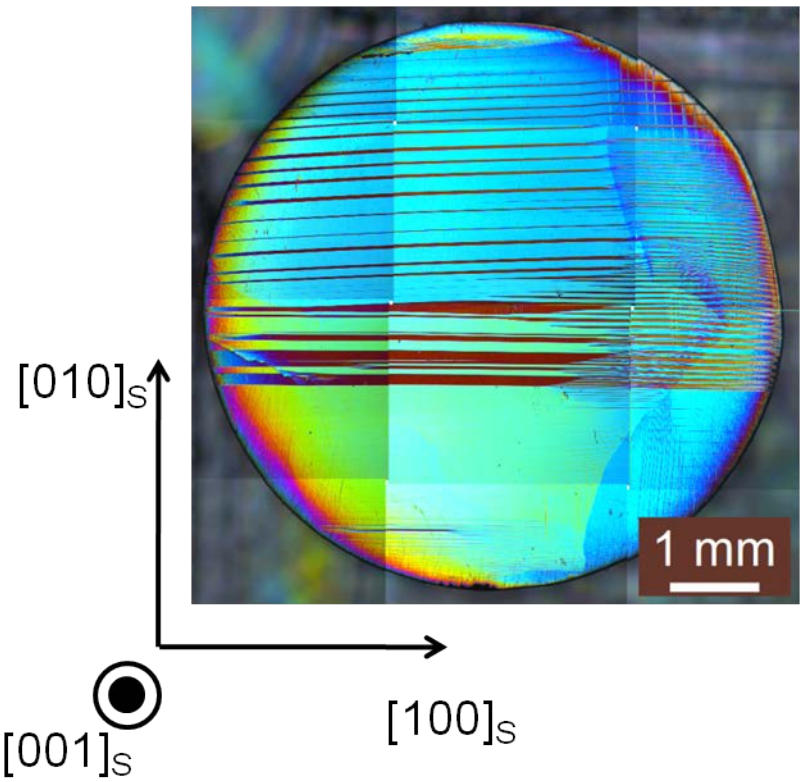

Figure 4.11 Differential interference contrast image of a cylindrical Ni-Mn-Ga single crystal used in rotary fatigue testing. The contrast in colors between the different twin variants is useful for analyzing images of twinned samples.

4.3 Fatigue Testing

Rotary fatigue testing was performed in a modified Jet lathe; see Figure 4.12. The tailstock was replaced by a machined Delrin polymer sample holder. The sample holder accommodated up to 60 samples that could be tested simultaneously. Samples were held in place with rubber o-rings on each face of the sample and are not constrained on their ends, which would prevent complete reorientation of the twin variants [19, 71, 78]. The samples were positioned in the slots of the sample holder so that $[100]_S$ was parallel to the axis of rotation. A piece of foam and tape held the o-rings and sample inside of the pockets in the sample holder. The active twin boundaries were parallel to the $[100]_S$ direction, so the sample could be removed and replaced by aligning the horizontal twin boundaries such that they were parallel to the axis of rotation.

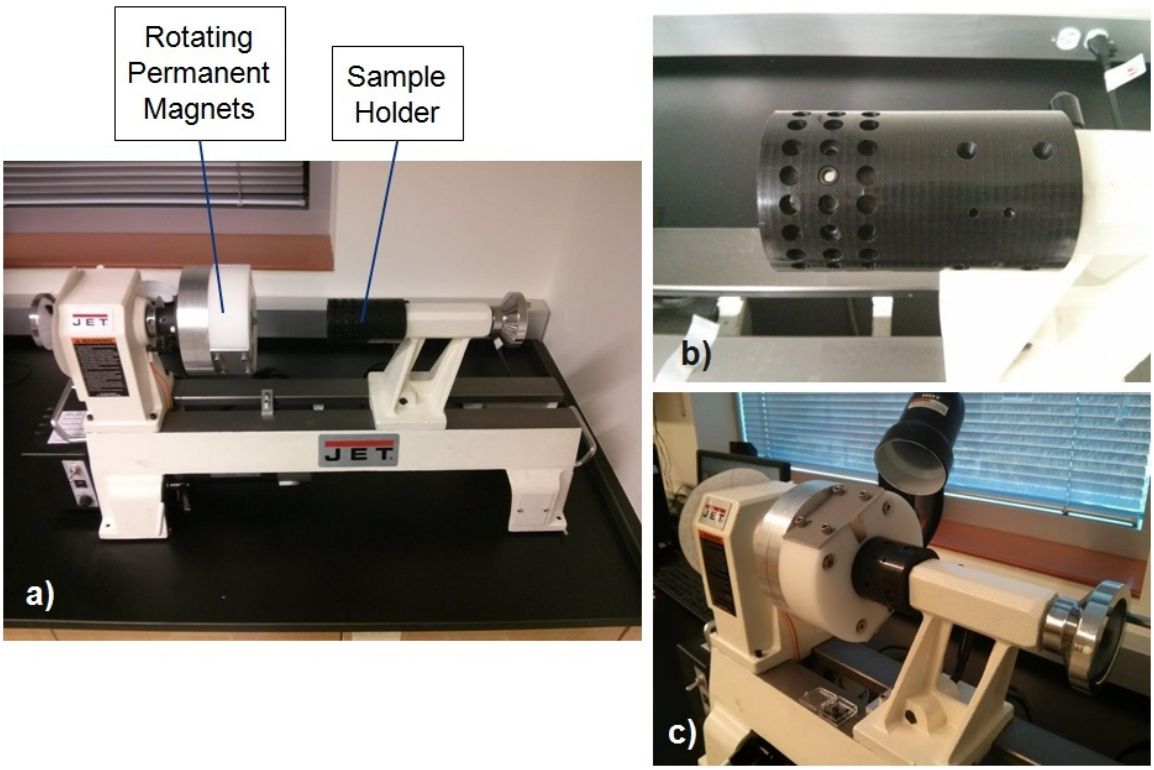

Figure 4.12 a) Rotary fatigue testing instrument. b) Sample holder retaining samples in a stationary position during testing. c) The sample holder slides into the sleeve containing the rotating permanent magnets.

The spindle of the lathe was modified to contain several permanent magnets that rotated around the samples. A large diametrically aligned magnet was mounted in the center with two rectangular magnets placed in a Delrin polymer sleeve surrounding the central magnet; see Figure 4.13. The sleeve containing the rectangular magnets was oriented such that the magnetic flux through the magnets was parallel with that of the diametrically aligned magnet. The sleeve increased the magnetic field that was applied parallel to the sample face during testing; see Figure 4.14. Figure 4.15 displays the magnetic field as a function of angle and compares the test set up with and without the sleeve containing the rectangular magnets providing an extra 0.16 MA/m to the magnetic field applied parallel to the sample face. The peaks are also thinner, resulting in a more concentrated application of the magnetic field.

The frequency of the rotary magneto-mechanical cycling was 17 Hz. The frequency in Aaltio's linear fatigue experiments ranged from 75-344 Hz [17, 72]. Frequency in rotary fatigue tests performed by Müllner and Chmielus was approximately 130 Hz [7, 67, 68]. Actuation response has been measured to be as low as 250 μs [38]. Therefore, the samples used in these fatigue tests and tests performed by others were actuated well below the maximum actuation frequency.

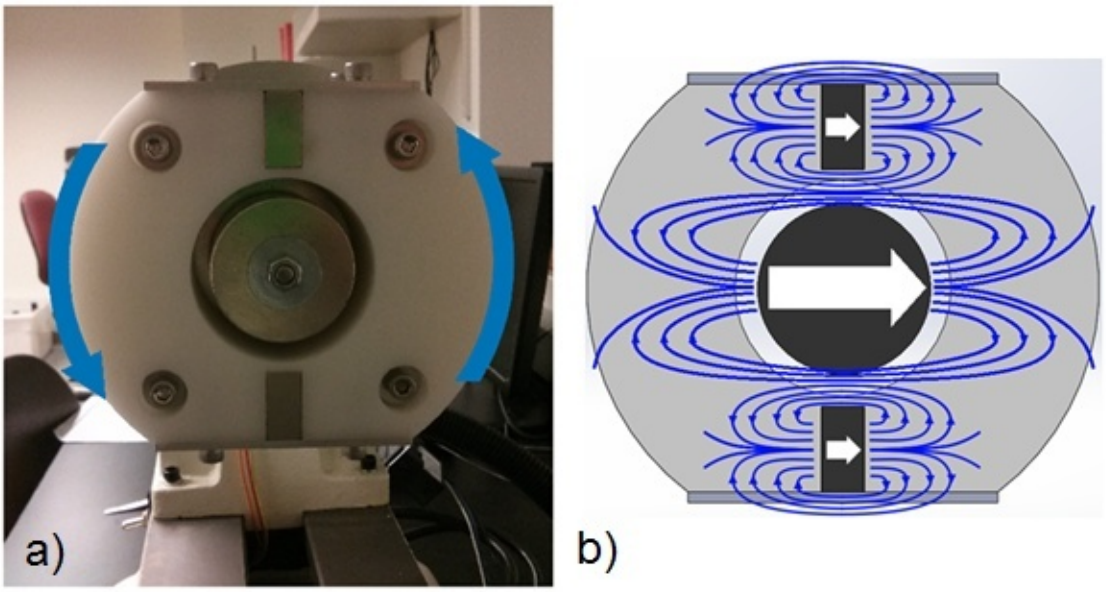

Figure 4.13 a) Rotating permanent magnets. The sample holder sleeve fits into the slot between the cylindrical and rectangular magnets. b) The magnets consist of a cylindrical diametrically aligned magnet and two rectangular magnets that help increase the magnetic field that is applied parallel to the sample face.

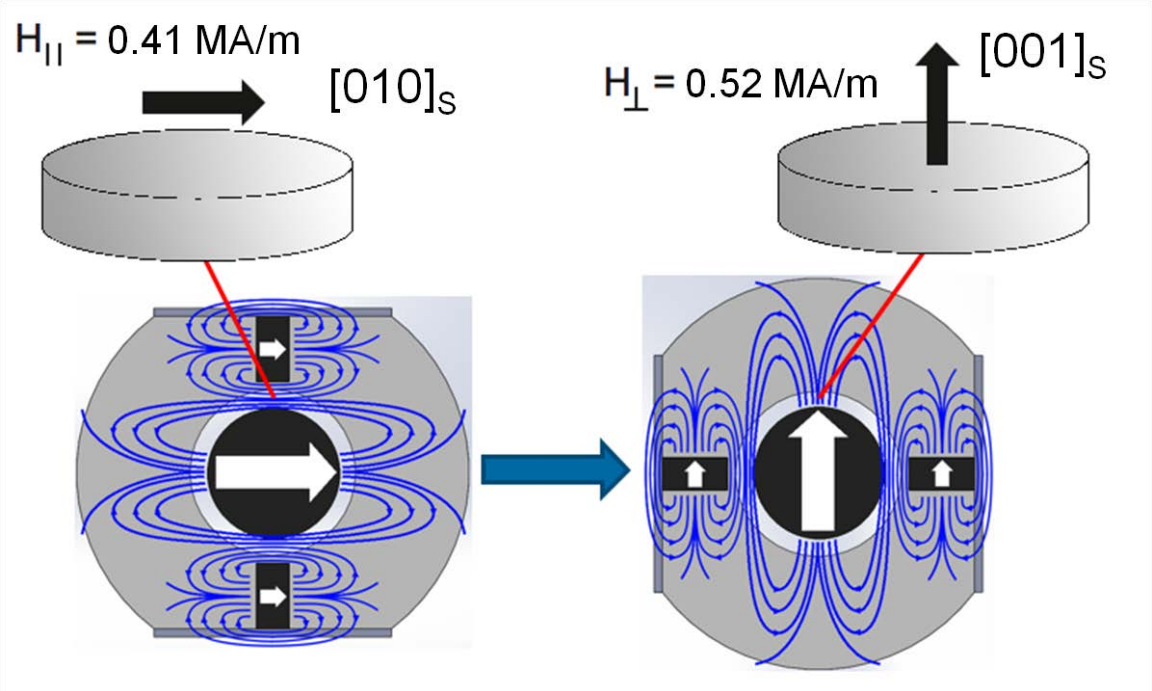

Figure 4.14 As the magnetic sleeve rotates, a maximum field of 0.41 MA/m is applied parallel to the sample face in the $[010]_S$ direction. When the sleeve rotates 90°, a maximum field of 0.52 MA/m will be applied perpendicular to the sample face in the $[001]_S$ direction.

Over the course of one revolution, the sample will endure two magneto-mechanical cycles [39]. This means that the crystal structure will reorient 4 times per revolution, resulting as the easy axis of magnetization rotates to remain parallel with the magnetic field lines. As the magnet is rotated, a maximum field of 0.41 MA/m is applied parallel to the sample face in the $[010]_S$ direction, and after rotating another 90° a maximum field of 0.52 MA/m is applied perpendicular to the sample face in the $[001]_S$, direction; see Figure 4.15. In both directions, the maximum magnetic field was at least two times the typical switching field measured in fatigue samples.

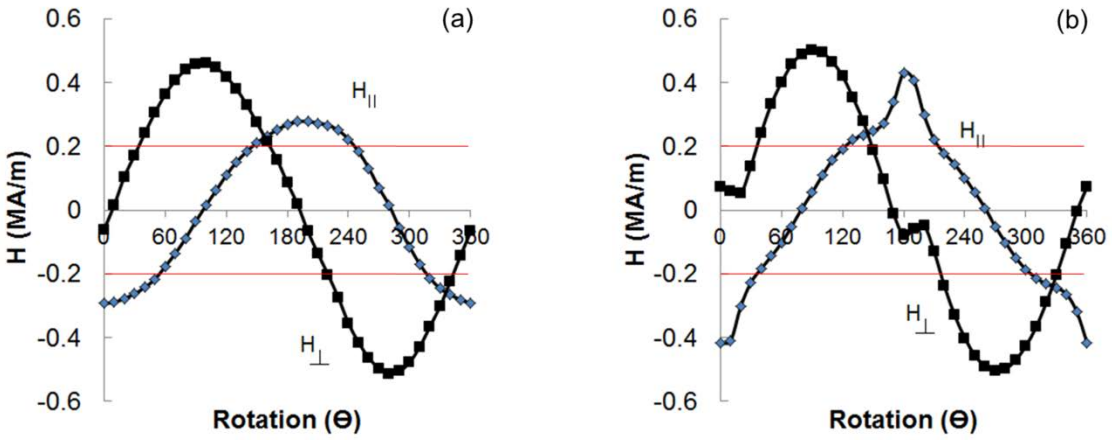

Figure 4.15 Diagrams representing the magnetic field as a function of angle for the magnetic field applied parallel to the sample face (blue dots) and the magnetic field applied perpendicular to the sample face (black dots). (a) The magnetic field as a function of angle only including the diametrically aligned magnet. (b) The magnetic field as a function of angle including all three permanent magnets. The red lines indicate the typical switching field required to reorient twin boundaries.

The maximum possible effective stress was approximately 2.5 MPa parallel to the sample face and approximately 3.5 MPa perpendicular to the sample face for unconstrained samples; see Figure 4.16. The maximum magnetostress depends on the geometry of the sample, the saturation magnetization, and magnetic saturation field. In a cylindrical sample where the thickness is less than the diameter, an increase in thickness or diameter results in a larger magnetic field required to achieve the same magnetostress. An increase in saturation magnetization or magnetic field saturation results in an increase in the maximum effective magnetostress.

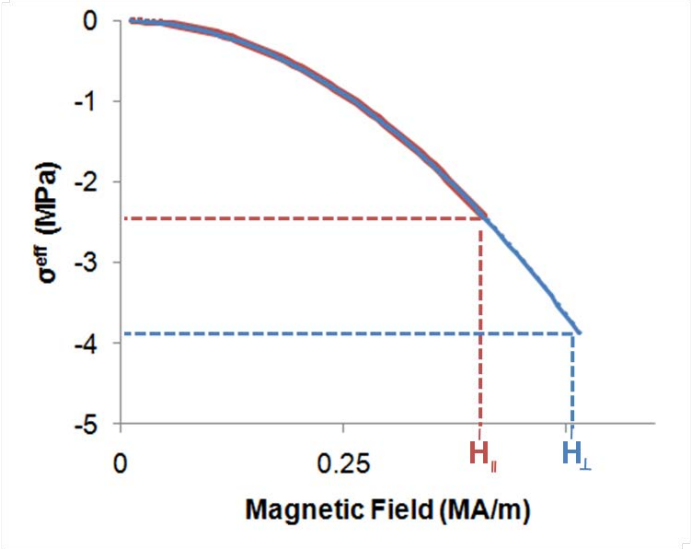

Figure 4.16 Diagram representing the maximum possible effective magnetostress as a function of magnetic field for CM154 G prior to fatigue testing. The maximum field applied parallel to the sample face in the $[010]_S$ direction is 0.41 MA/m (red). The maximum field applied perpendicular to the sample face in the $[001]_S$ direction is 0.52 MA/m (blue).

CHAPTER FIVE: RESULTS

This chapter presents the results from XRD, EDS, and VSM characterization in the first section. The second section contains the results from rotary fatigue testing, including crack propagation and fatigue life. Supplemental tables and figures related to the results are located in the appendix.

5.1 Characterization

5.1.1 XRD and EDS

X-Ray diffraction of the single crystals at room temperature was used to determine the lattice parameters, orientation, and crystal structure. The lattice parameters are listed in Table 5.1 and range from 5.937-5.964 Å for *a* and 5.568-5.591 Å for *c*. The crystals were oriented so that they could be placed in the fatigue setup with the $[100]_S$ direction of the crystal parallel to the axis of rotation of the spinning magnets.

Table 5.1 Lattice parameters for single crystals used in fatigue tests and compression tests. The short axis, *c*, is aligned with the easy axis of magnetization. Using the pseudo-tetragonal unit cell for the 10M structure, two axes, *a*, will be of equal length.

Single Crystal	Lattice Parameter, *a* (Å)	Lattice Parameter, *c* (Å)
CM132	5.964 ± 0.002	5.569 ± 0.002
CM142	5.937 ± 0.002	5.569 ± 0.002
CM143	5.943 ± 0.002	5.569 ± 0.002
CM154	5.944 ± 0.002	5.582 ± 0.002
CM158	5.950 ± 0.002	5.591 ± 0.002
CM161	5.950 ± 0.002	5.568 ± 0.002

The range in composition calculated from EDS data for the 10M portions of the single crystals used in fatigue testing and compression testing is listed in Table 5.2. The

range starts at the location closest to the seed end of the crystal and ends at the location farthest away from the seed within the portion of the crystal corresponding to a specific crystal structure.

Table 5.2 Compositional range (atomic-%) over the length of the 10M portions of single crystals used in fatigue tests and compression tests. The first value in each column corresponds to the composition of the 10M portion nearest to the seed end of the crystal and the second value corresponds to the composition of the 10M portion farthest away from the seed.

Single Crystal	Ni (at-%)	Mn (at-%)	Ga (at-%)
CM132	50.8-50.4 ± 0.2	25.9-27.2 ± 0.2	23.3-22.4 ± 0.2
CM142	51.1-50.1 ± 0.2	24.8-25.6 ± 0.2	24.1-23.7 ± 0.2
CM143	51.2-50.9 ± 0.2	24.8-25.4 ± 0.2	24.0-23.7 ± 0.2
CM154	51.5-51.1 ± 0.2	25.0-26.6 ± 0.2	23.5-22.3 ± 0.2
CM158	51.7-51.6 ± 0.2	25.5-26.5 ± 0.2	22.8-22.0 ± 0.2
CM161	51.6-51.4 ± 0.2	25.8-27.2 ± 0.2	22.7-21.4 ± 0.2

The composition of nickel and gallium decreases towards the end opposite of the seed while manganese increases as seen in Figure5.1. See the appendix for additional EDS/XRD diagrams of single crystals used in experiments. Samples used in testing were cut from the 10M region of the single crystals, shown in pink, in the diagrams. Single crystals that were grown longer than 100 mm exhibited a more gradual change in the composition of elements. CM158 did not appear to have the same type of variation in composition towards the end of the crystal. CM158 did not contain any non-modulated structure at the end of the crystal, however it did contain the most variation within each portion of the crystal. The 10M/14M regions are identified when diffraction peaks from both crystal structures are present in XRD measurements. Typical single crystals with this composition, exemplified by CM132 in Figure 5.1, start with a 10M structure and

progress into a mixture of 10M and 14M, followed by 14M, and finally a small section of non-modulated structure at the opposite end of the crystal.

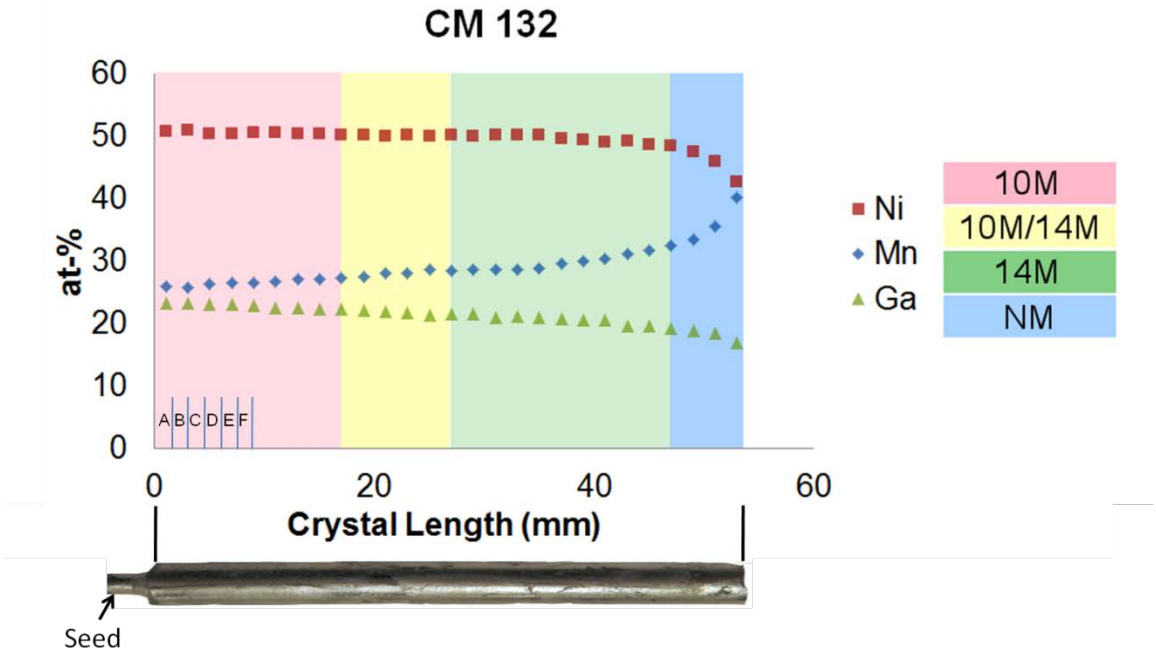

Figure 5.1 XRD and EDS diagram for CM132 a $Ni_{51.2}Mn_{26.6}Ga_{22.2}$ (at-%) single crystal used in fatigue testing. Data points represent crystal composition and shaded areas represent crystal structure. The face of the $(001)_S$ plane at crystal length 0 mm is the face that was exposed from cutting the seed off of the crystal. The data was obtained along the length of the crystal corresponding to the image of the crystal shown below the diagram. The letters in the bottom left corner of the diagram correspond to the locations of samples that were cut from the crystal. Reference Table A.3 for list of samples tested in the rotary instrument.

Table 5.3 presents the average absolute deviation from the nominal composition of each single crystal in the 10M and 14M portions. The maximum average absolute deviation in the 10M portions of the crystals was 0.6 at-%, 1.8 at-%, and 1.9 at-% for nickel, manganese, and gallium, respectively. The maximum average absolute deviation in the 14M portions of the crystals was 1.7 at-%, 3.4 at-%, and 1.9 at-% for nickel, manganese, and gallium, respectively. The crystal composition deviates more towards the

end furthest away from the seed end due to chemical segregation at the liquid-solid interface during melting.

Table 5.3 Average absolute deviation from the nominal composition of $Ni_{51.2}Mn_{26.6}Ga_{21.2}$ for the 10M portion and 14M portion for each single crystal used in this thesis.

	10M			14M		
	Ni (at-%)	Mn (at-%)	Ga (at-%)	Ni (at-%)	Mn (at-%)	Ga (at-%)
CM132	0.6	0.4	0.7	1.7	3.4	1.7
CM142	0.2	1.8	1.9	0.8	1.2	0.4
CM143	0.3	1.5	1.7	0.8	1.4	0.5
CM154	0.2	0.9	0.9	1.0	2.1	1.1
CM158	0.4	0.4	0.3	0.9	0.8	0.3
CM161	0.3	0.4	0.3	0.8	2.7	1.9

5.1.2 Magnetic Properties

Due to the anisotropy of the crystal structure, the magnetization of the sample measured by the pickup coils in the VSM will depend on how the twin variants are oriented. The magnetization of the sample was the highest when the element was in a single variant state and the easy axis of magnetization was parallel with the applied magnetic field. A table containing the average initial switching field measurements for all fatigue samples is located in the appendix. The as measured switching field for samples measured with the magnetic field applied parallel to the sample face, $[010]_S$, was lower than the switching field measured with the field perpendicular to the sample face, $[001]_S$; see Figure 5.2. The effective switching field was determined by factoring in the demagnetizing field. The effect is more prevalent in the case of the switching field measured perpendicular to the sample face because of the larger demagnetization factor. The difference is due to the geometry of the sample.

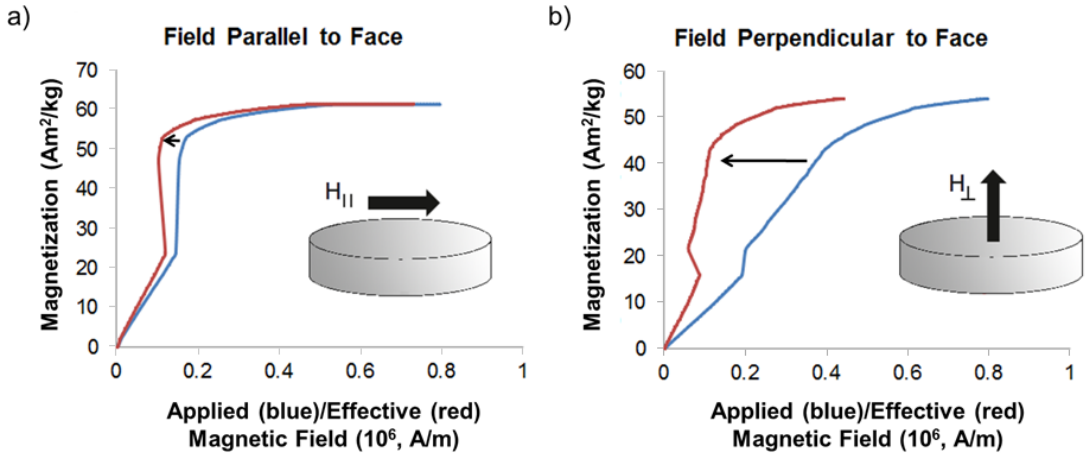

Figure 5.2 a) Switching field test performed with the magnetic field applied parallel to the face of the sample. b) Switching field test performed with the magnetic field applied perpendicular to the sample face. The blue curve represents the magnetization as a function of applied magnetic field. The red curve represents the magnetization of the sample as a function of the effective magnetic field considering the demagnetization factor.

The switching field measurements in Figure 5.2 depict a sudden increase in magnetism when the crystal structure reorients. The slope of the increase switches from positive to negative when the demagnetization factor is included in the applied magnetic field. This is due to the demagnetizing field increasing from the increase in magnetization while the applied magnetic field increases very little. It is necessary to include the demagnetizing field in calculations for magnetostress on the reorientation of Ni-Mn-Ga crystal structures.

The effective compressive stress, in a domain with the *c*-axis perpendicular to the magnetic field, as a function of magnetic field was calculated using models based on [10, 40-42]; refer to Section 3.3.2. See the appendix for a list of fatigue samples including the effective twinning stress. By including the demagnetization field, the stress required to initiate twin boundary motion corresponds with the jump in the switching field measurements; see Figure 5.3. In the presented magnetostress vs. field image, there is a

shift in magnetic field that corresponds to the switching field required to reorient the twin variant.

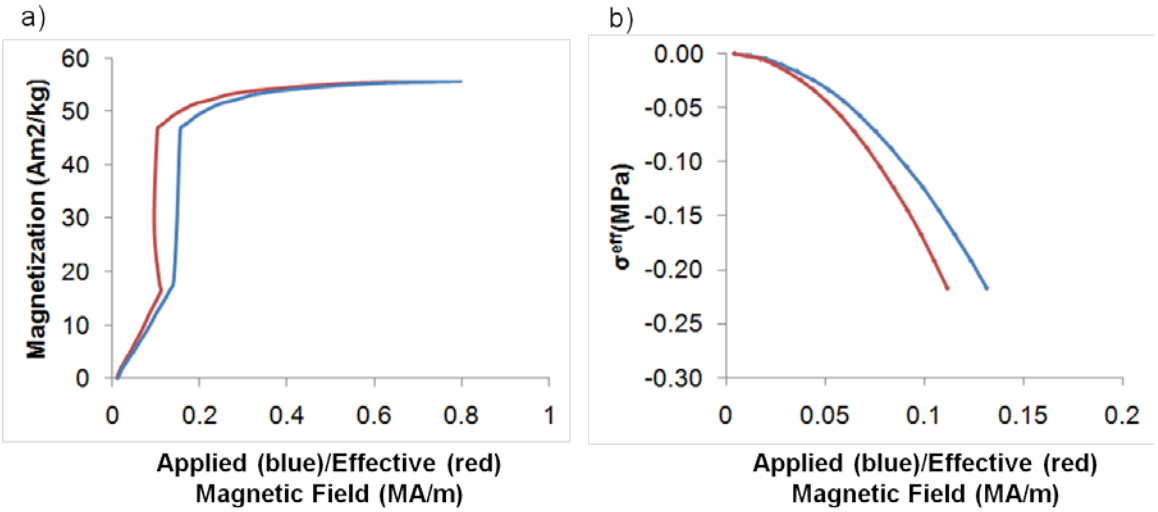

Figure 5.3 a) Depicts the switching field measurement for CM154 J. b) Magnetostress diagram corresponding to an increasing magnetic field up to the point of reorientation. The magneto stress diagram in a) correlates to the switching field diagram in a). The blue curve represents the applied magnetic field. The red curve represents the effective magnetic field considering the demagnetization factor.

Figure 5.4 presents the switching field results of CM154 V prior to rotational fatigue testing and after the sample had been cycled to 405,000 revolutions. There are no large jumps in magnetization after the sample has been cycled to 405,000 revolutions. The effective magnetic field is essentially zero until the applied magnetic field overcomes the demagnetizing field of the sample. At a high number of cycles, when a sample contains many cracks the ability for twin variants to reorient decreases.

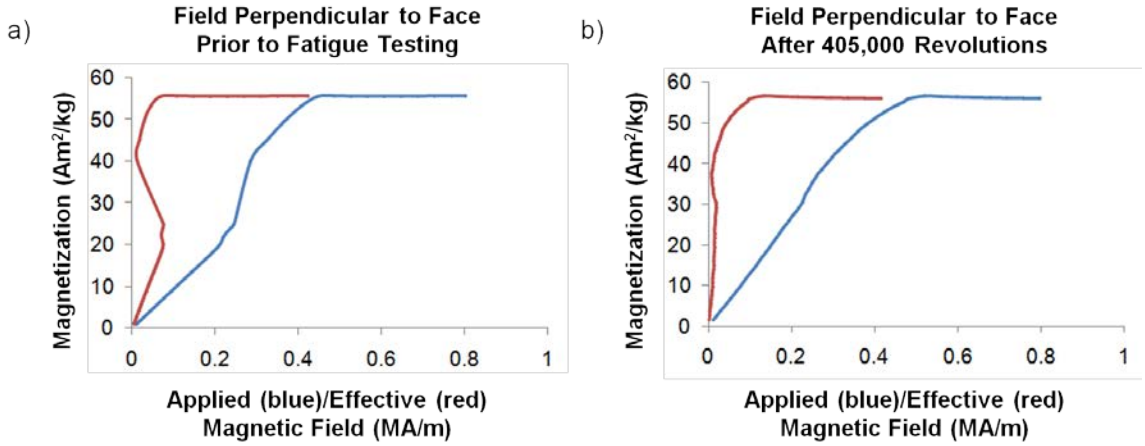

Figure 5.4 a) Switching field measurement from CM154 V with the magnetic field applied perpendicular to the sample face prior to any fatigue. b) Switching field measurement from CM154 V after being cycled to 405,000 revolutions with the magnetic field applied perpendicular to the sample face. The blue curve represents the magnetization as a function of applied magnetic field. The red curve represents the magnetization of the sample as a function of the effective magnetic field considering the demagnetization factor.

The effective twinning stress calculated from switching field measurements for each sample can be found in the appendix in Table A.4. The average twinning stress calculated for samples with similar preparation methods is located in Table 5.4. Electropolished samples had the highest average twinning stresses due to their respective high surface roughness. For a majority of the samples that were monitored throughout testing, the slope of the magnetostress curves is steeper at higher cycles; see Figure 5.5. See Appendix Figures A.4-A.10 for details regarding the rest of the samples that were analyzed throughout testing.

Table 5.4 Effective twinning stress for groups of samples with a specified surface preparation pertaining to a respective single crystal. Measurements were made prior to fatigue testing. See appendix for individual sample results.

Single Crystal	Sample Preparation	Effective Twinning Stress Parallel to Sample Face (MPa)	Effective Twinning Stress Perpendicular to Sample Face (MPa)
CM132	3µm	-0.4 ± 0.2	-0.6 ± 0.2
CM132	1µm	-0.20 ± 0.07	-0.66 ± 0.02
CM142	3µm	-0.3 ± 0.1	-0.3 ± 0.2
CM143	3µm	-0.3 ± 0.2	-0.7 ± 0.4
CM154	3µm	-0.30 ± 0.09	-0.5 ± 0.2
CM154	HNO_3	-0.20 ± 0.08	-1.0 ± 0.3
CM154	0.04µm	-0.27 ± 0.07	-0.50 ± 0.07
CM158	3µm	-0.3 ± 0.1	-0.24 ± 0.06

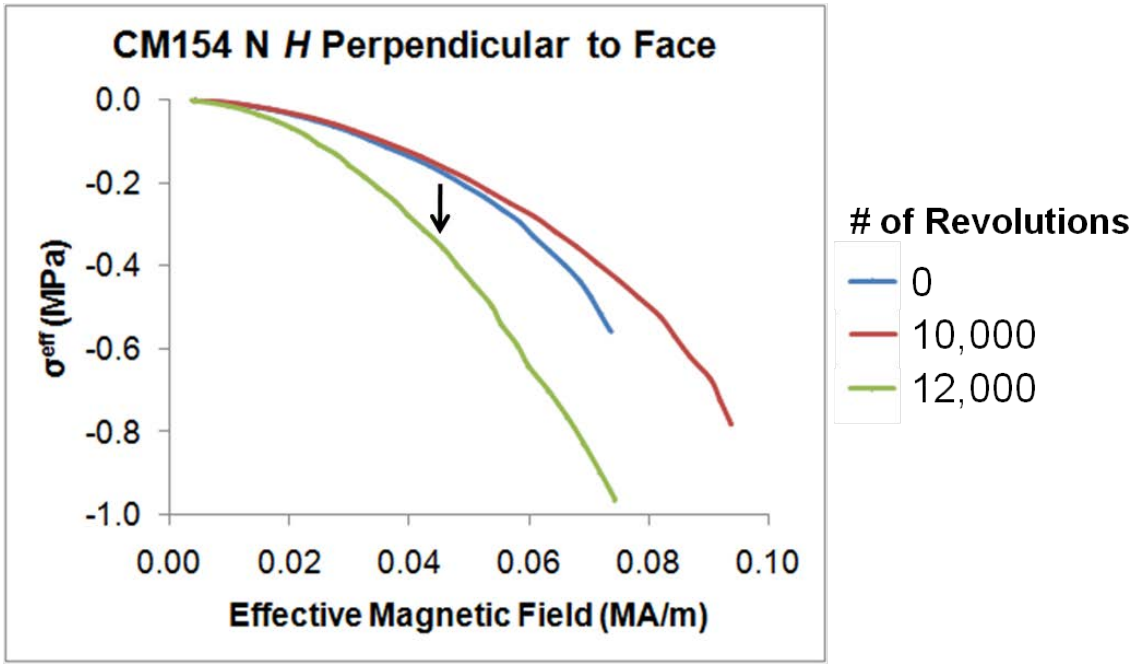

Figure 5.5 Effective magnetostress calculated from switching field data as a function of effective magnetic field for three stages of fatigue testing for CM154 N. The data is plotted to the point at which the switching field is reached. The maximum compressive magnetostress is the effective twinning stress.

5.1.3 Compression Testing

The results for the compression tests from single crystal CM161 are listed in Table 5.5. The average twin plateau stress was calculated from the average stress from strain ranging arbitrarily from 1% to 5%. The average maximum twin nucleation stress occurred below 1%. The stress required to initiate twin boundary motion was very low, suggesting that there were multiple martensite variants present in the crystal structure, so a large stress was not required to initiate twin boundary motion. The twinning plateau stress is below 1 MPa for all crystals, which is typical of single crystals with 10M structure that are grown with high purity elements [40]. The stress-strain curves for the samples were similar in characteristics regarding the twin nucleation stress and twin plateau stress; see Figure 5.6. There was an initial threshold stress that must be overcome due to nucleation of twin boundaries and the stress required to initiate twin boundary movement [69]. As the twin boundaries moved and the variant was reoriented, the stress remained constant. The plateau region extended to just over 6% strain, which means the crystal was nearing its theoretical strain limit. As the strain approaches 6%, there is a sharp increase in the stress because the sample has completely reoriented and the stress is only inducing elastic deformation at this point.

Table 5.5 Average blocking stress and twinning stress for compression samples cut from CM161.

Single Crystal	Compression Sample	Average Maximum Twin Nucleation Stress (MPa)	Average Twin Plateau Stress (MPa)
CM161	A1	0.96 ± 0.09	0.5 ± 0.2
CM161	A2	1.15 ± 0.07	0.3 ± 0.2
CM161	B1	1.2 ± 0.1	0.8 ± 0.1
CM161	B2	1.1 ± 0.2	0.8 ± 0.1
CM161	C1	1.44 ± 0.08	0.45 ± 0.08

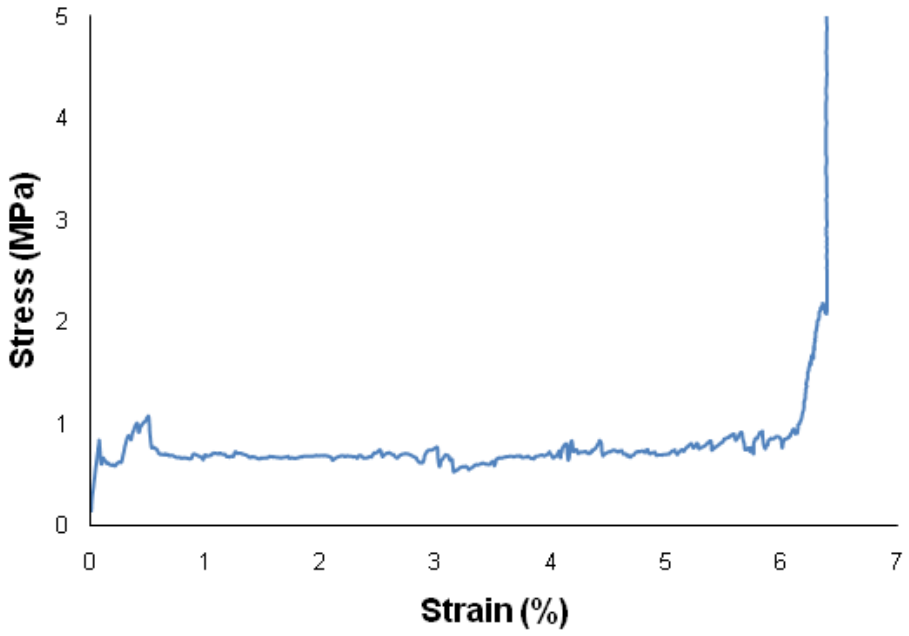

Figure 5.6 Stress-Strain diagram for uniaxially compressed rectangular prism CM161 B1. Average twin plateau stress is 0.8 ± 0.1 MPa. Once the initial barrier stress is overcome, the stress remains relatively constant while twin boundaries are moving and the twin variant is reorienting. When the element has completely reoriented, the stress increases sharply at the onset of elastic deformation.

A1 and A2 were cut from the section of crystal that was closest to the seed. This section had the lowest average twin plateau stress. B1 and COMP 4 were cut from the next section of grown single crystal and had the highest average twin plateau stress. C1 was cut from the last useable section of single crystal and the average twin plateau was lower than the previous section.

5.1.4 Surface Roughness

The average surface roughness was measured for each group of samples with similar preparation methods; see Table 5.6. The samples exhibiting the highest surface roughness were those that were electropolished prior to testing. Samples prepared by mechanically polishing to 1 μm and 0.04 μm had the lowest average surface roughness.

See Table A.3 in the appendix for a complete list of the average surface roughness of each sample used in fatigue testing.

Table 5.6 Average surface roughness and standard deviation of samples with a specified surface preparation pertaining to a respective single crystal. See appendix for individual sample results.

Single Crystal	Sample Preparation	Ra, Average Surface Roughness (nm)	Surface Roughness Range (nm)
CM132	3µm	22 ± 5	17-26
CM132	1µm	14 ± 7	9-19
CM142	3µm	35 ± 16	25-51
CM143	3µm	29 ± 6	25-35
CM154	3µm	77 ± 44	20-125
CM154	HNO_3	128 ± 66	84-232
CM154	0.04µm	16 ± 6	13-22
CM158	3µm	19 ± 9	13-31

5.2 Fatigue Results

5.2.1 Crack Propagation

Samples tested in the rotary fatigue instrument exhibited three different characteristic cracks; see Figure 5.7. The first type of crack (type-a) tended to propagate straight in the $<110>_S$ direction; see Figure 5.8. Aaltio reported that cracking occurs on twinning planes [17, 72]. However, the cracking occurring in these fatigue experiments is not only occurring on the active twinning planes. The active twinning planes in Figure 5.8 are parallel to $(011)_S$, yet the crack direction is $<110>_S$ and the macroscopic fracture planes are close to $\{111\}_S$. This is schematically represented in Figure 5.9.

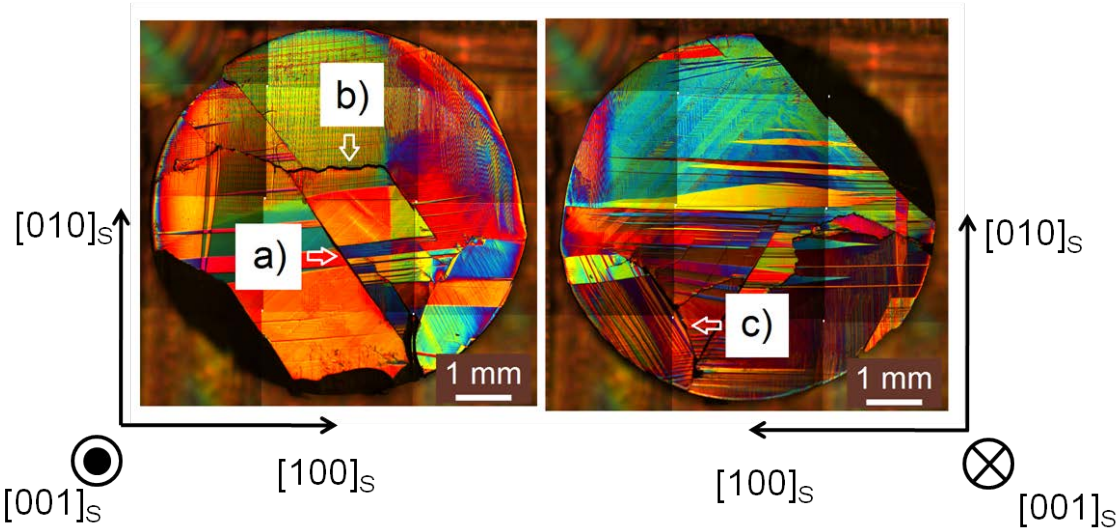

Figure 5.7 DIC microscopy mosaic images of CM143F after 30,000 revolutions. The left image is the top of the sample and the right image is the bottom of the sample. Three different types of cracks are present on the faces of the samples. a) Cracks propagating in the <110>$_S$ direction. b) Cracks propagating in a general [100]$_S$ direction. c) Cracks that follow low angle grain boundaries.

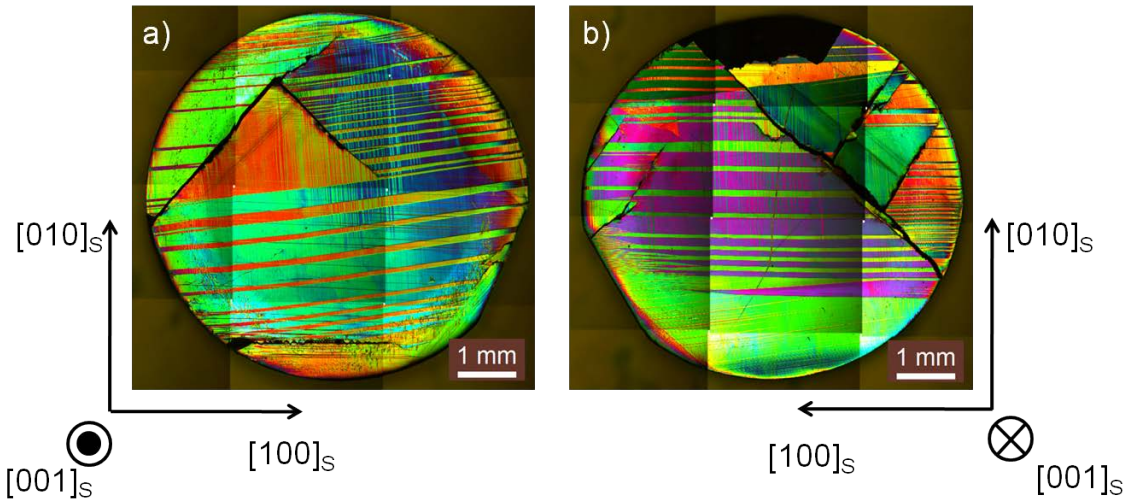

Figure 5.8 DIC microscopy mosaic images of CM132B after 90,000 revolutions. a) Top of the sample. b) Bottom of the sample. Cracking occurring on the surface follows <110>$_S$ and a macroscopic {111} plane.

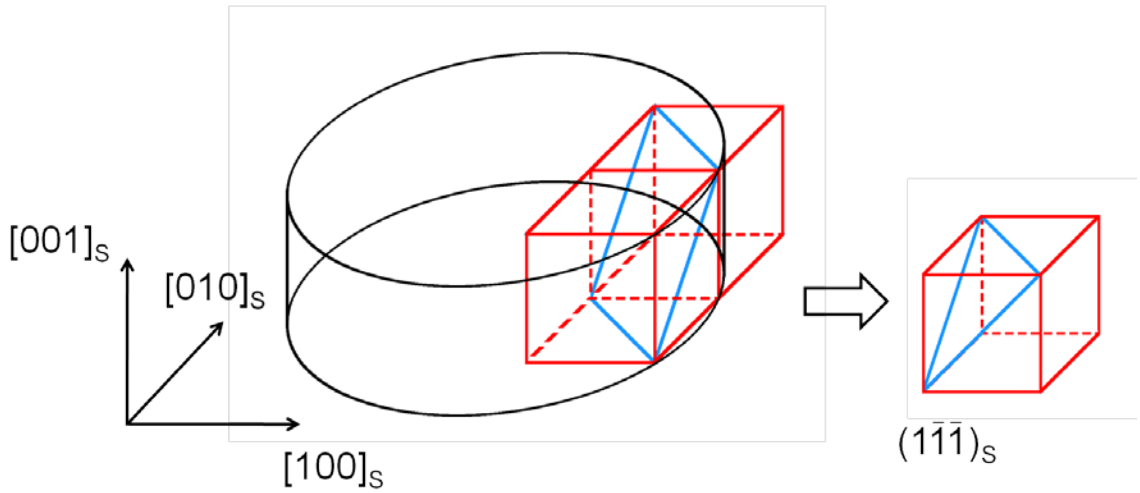

Figure 5.9 Schematic illustrating the fracture plane in reference to a unit cell. The black cylinder represents the sample. The red cubes represent the orientation of the unit cell (austenite). The blue plane represents the fracture plane and is characteristic of $\{111\}_S$ planes. The unit cell depicted on the right represents the intersection of the fracture plane with the unit cell.

The second type of crack (type-b) tended to propagate macroscopically along $[100]_S$. On a smaller scale, type-b cracks propagated in the $<110]_S$ direction zigzagging back and forth horizontally across the sample face; see Figure 5.10. The pink horizontal lines in the top part of Figure 5.10 are twins. There are no twin boundaries in the bottom portion of the image; lines in the bottom portion are due to surface topography from polishing.

The third type of crack (type-c) tended to occur in samples that were close to the seed end of the crystal (Figure 5.7). These type of cracks were observed in single crystals CM143, CM154, and CM158. On many of the samples, low angle grain boundaries were present, suggesting that the material is not completely single crystalline. The cracks appear to follow small angle grain boundaries (SAGB) that can be seen in Figure 5.11.

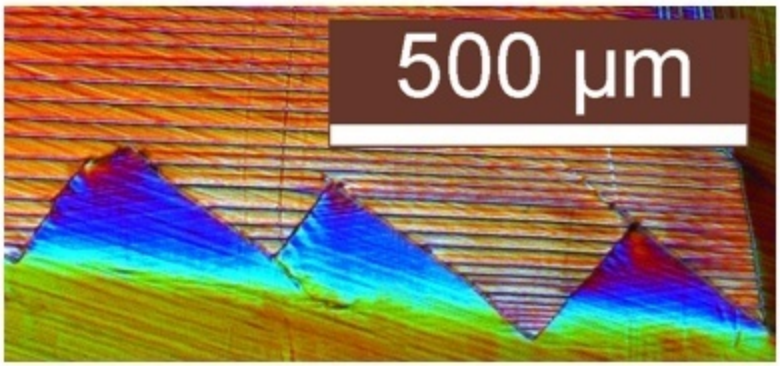

Figure 5.10 DIC microscopy image of CM158N after 2,000 revolutions. Fatigue cracks propagating in a general $[100]_S$ direction, but following $[110]_S$ crack directions.

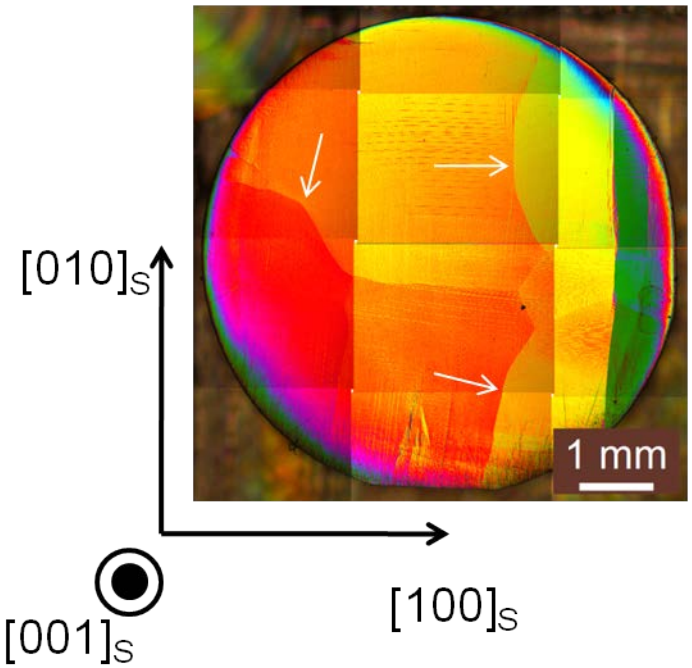

Figure 5.11 DIC microscopy mosaic images of CM154A prior to fatigue cycling. Small angle grain boundaries are indicated by white arrows.

The twin boundaries still move freely between two areas separated by SAGBs, however it is clear that the grain boundaries influence the structure of the twin boundaries locally; see Figure 5.12. In the first image, the twin boundaries on the right are vertically higher than those on the left and the twins running across the boundary divide up into smaller twins. In the bottom image, the twins are clearly kinked across the SAGB.

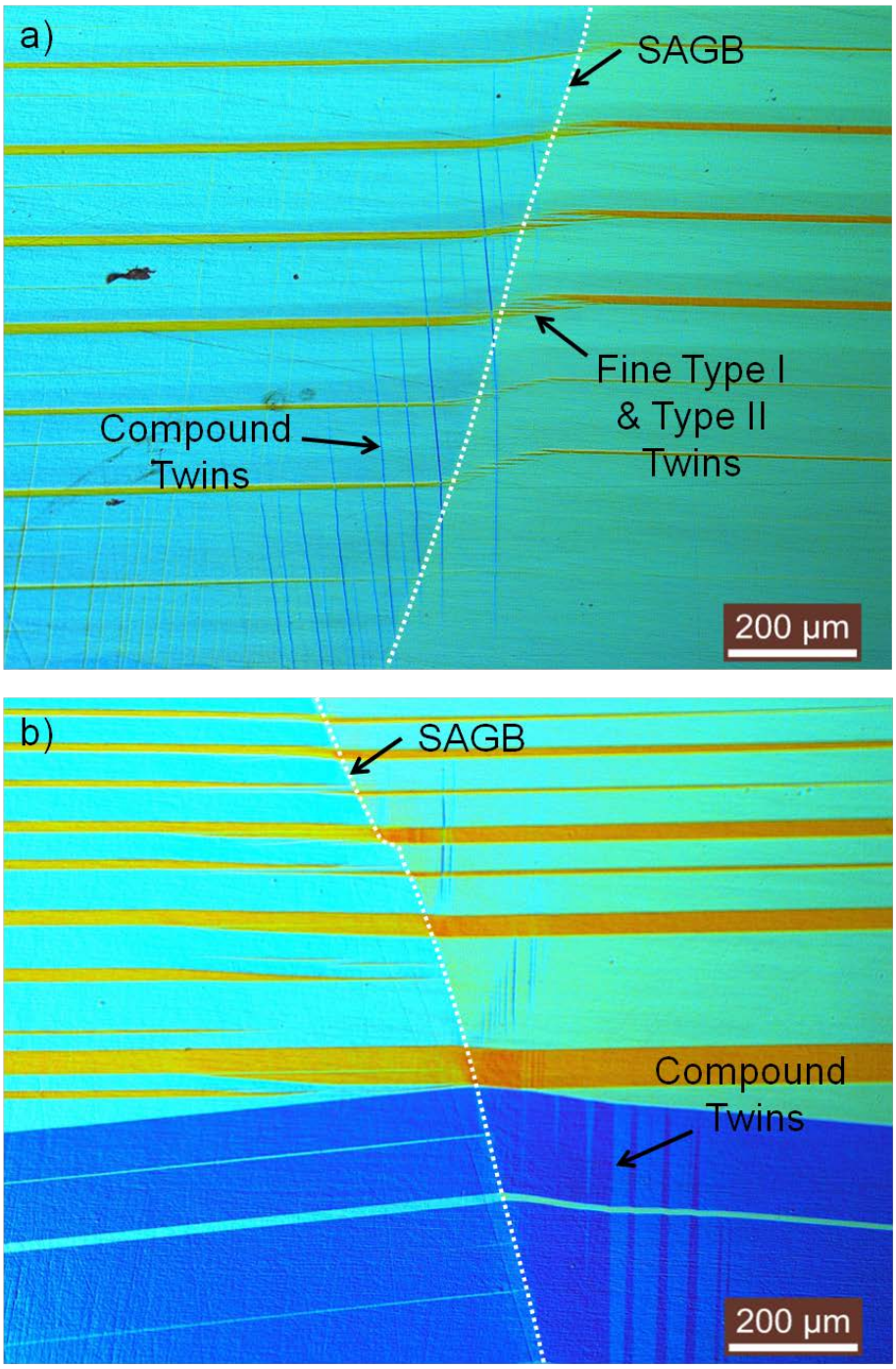

Figure 5.12 DIC microscopy images of CM54A after 20,000 revolutions. a) Twins decompose into multiple fine twins across the SAGB. b) Twin boundaries are kinked where they cross over SAGBs. SAGBs indicated by white dotted line.

Fracture initiated from within the bulk of the material as well as from the edges of the samples; see Figure 5.13. Crack initiation occurring in the middle of the sample

tended to occur when a sample had been cycled to a higher number. Cracks propagated from the edges of samples most prominently. Cracking from the edges occurred after only 2,000 revolutions for some samples.

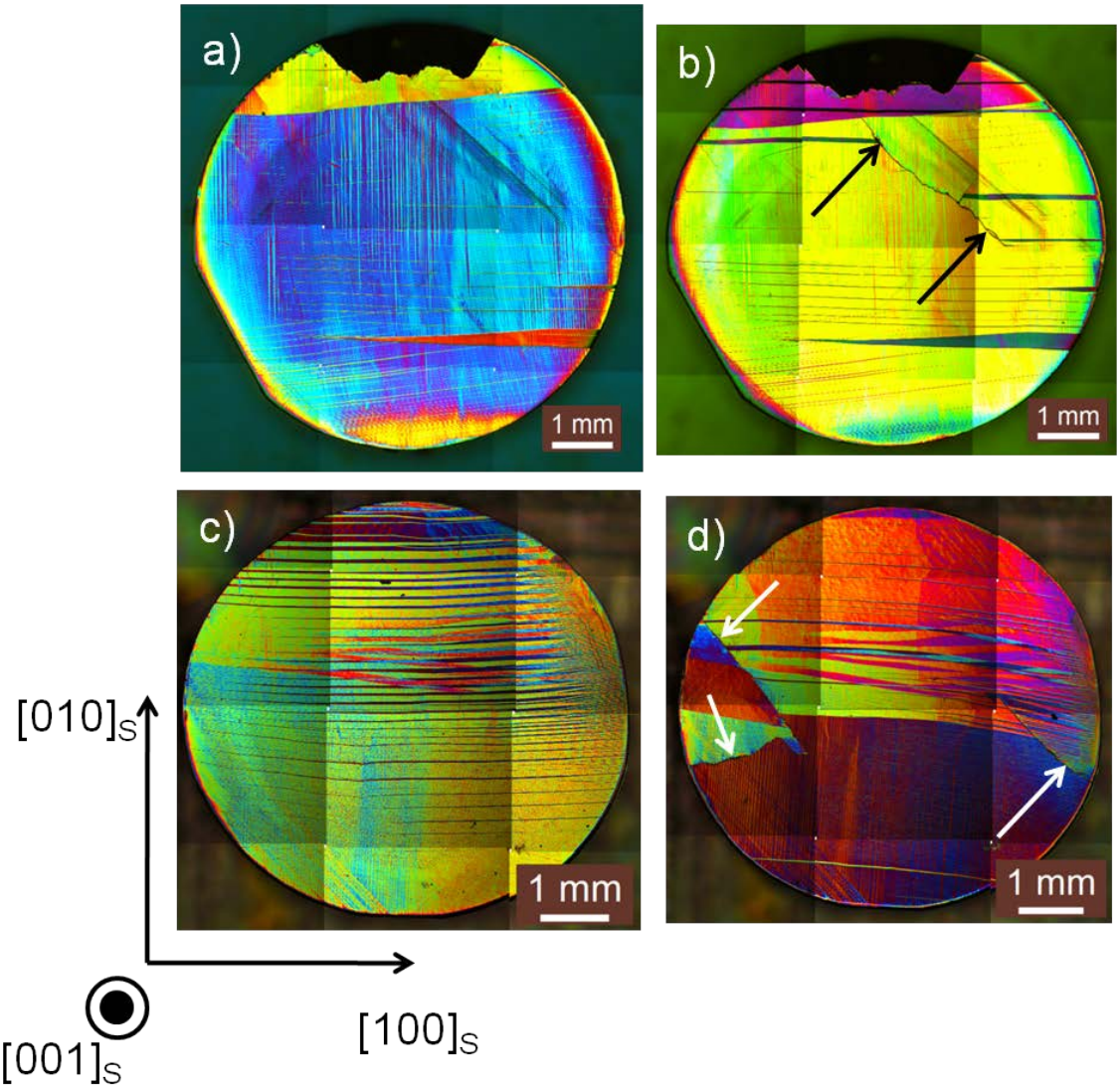

Figure 5.13 DIC microscopy mosaic images of fatigue samples indicating crack initiation points. a) CM132 B after 50,000 revolutions. b) CM132 B after 60,000 revolutions. Cracks initiating in the central part of the sample indicated by black arrows. c) CM154 T after 10,000 revolutions. d) CM154 T after 20,000 revolutions. Multiple cracks initiating from the edges of the samples indicated by white arrows.

While the fracture plane of fatigue sample was macroscopically close to {111}, the actual fracture plane is more complex; see Figure 5.14. The fracture markings 'point'

towards internal defects. The topography was characterized by long sharp striations and was indicative of brittle fracture. Further away from the defect, the striations were parallel with one another. At the surface of the sample, twin boundaries were found to be pinned at jagged intersections of the fracture surface; see Figure 5.15.

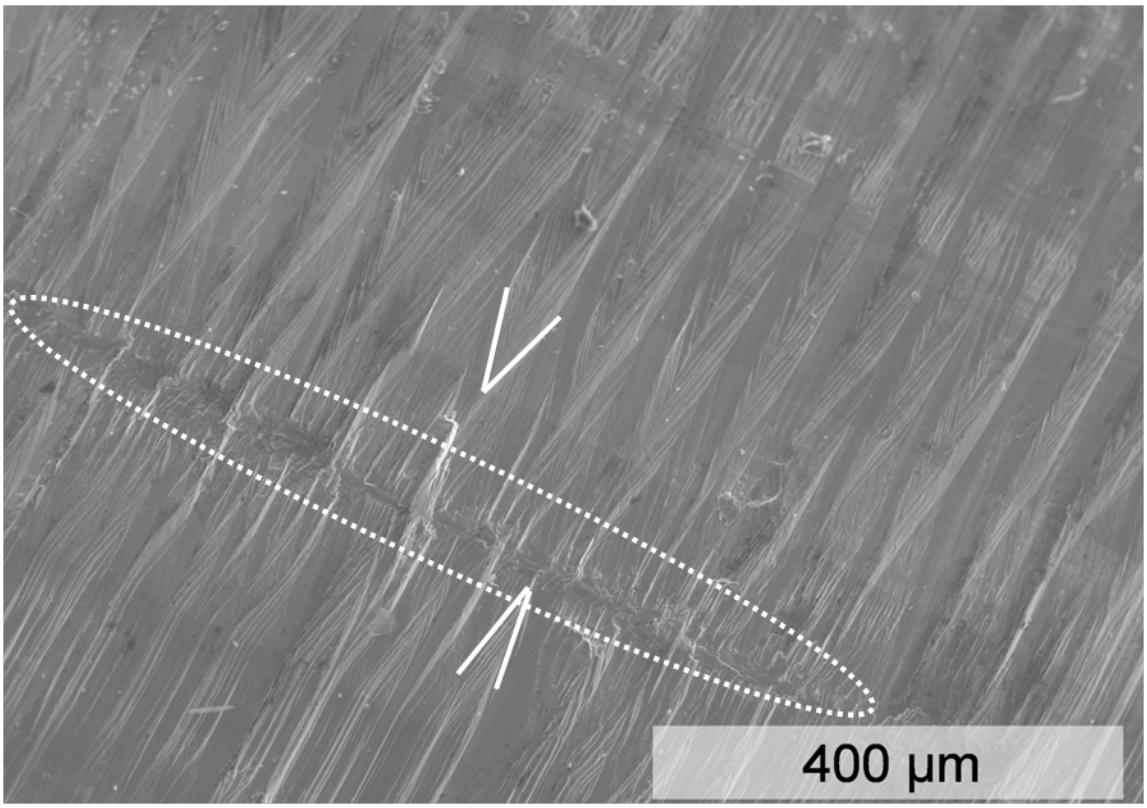

Figure 5.14 SEM image of CM132 E {111} macroscopic fracture plane. Fracture plane is characterized by jagged striations indicating brittle fracture. The river marking on the fracture surface point towards internal defects as indicated by the white arrows. The internal defect is circled by the dotted line.

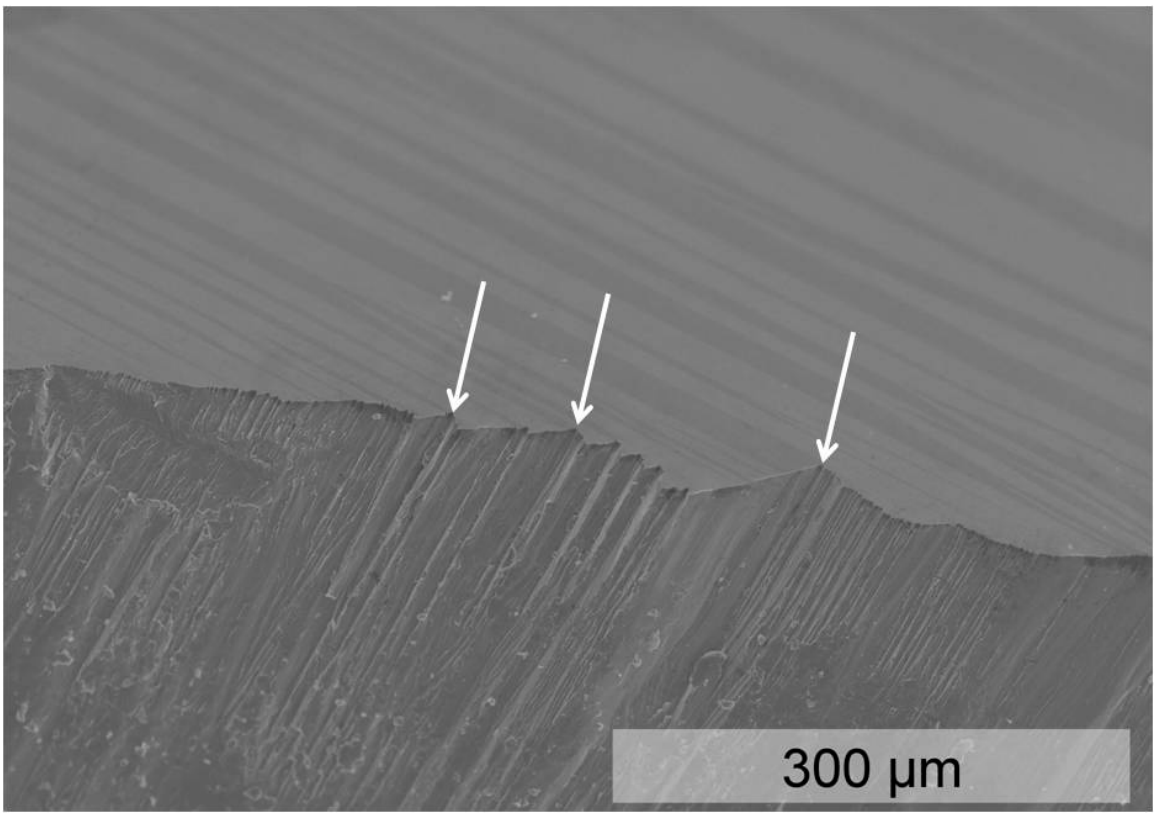

Figure 5.15 SEM image of CM32 E sample surface and fracture surface. Twin boundaries are pinned at the corners of the jagged fracture surface. Examples are indicated by the white arrows. The fracture surface impedes twin boundary motion.

5.2.2 Notched Fatigue Samples

Several samples from CM154 and CM158 were notched in the $[100]_S$ direction and $[110]_S$ direction. The notches induce stress concentrations allowing cracks to propagate at low cycle numbers and in a controlled location. Fatigue induced cracks tended to propagate either across the sample in a general $[100]_S$ direction or in a linear $[110]_S$ in unmolested samples. Cracks preferentially propagated from the $[100]_S$ notches in $<110>_S$ directions; see Figure 5.16. The fracture plane separates portions of the crystals that react independently to an applied field. This can be seen in Figure 5.17 where the large dark red twin is only present in the right portion of the crystal. CM154 J in Figure 5.16 also shows separation of microstructures where compound twins are

present on the left portion of the crack, but they are not present on the right portion. Cracks at the notch tip occurred in as few as 2,000 revolutions.

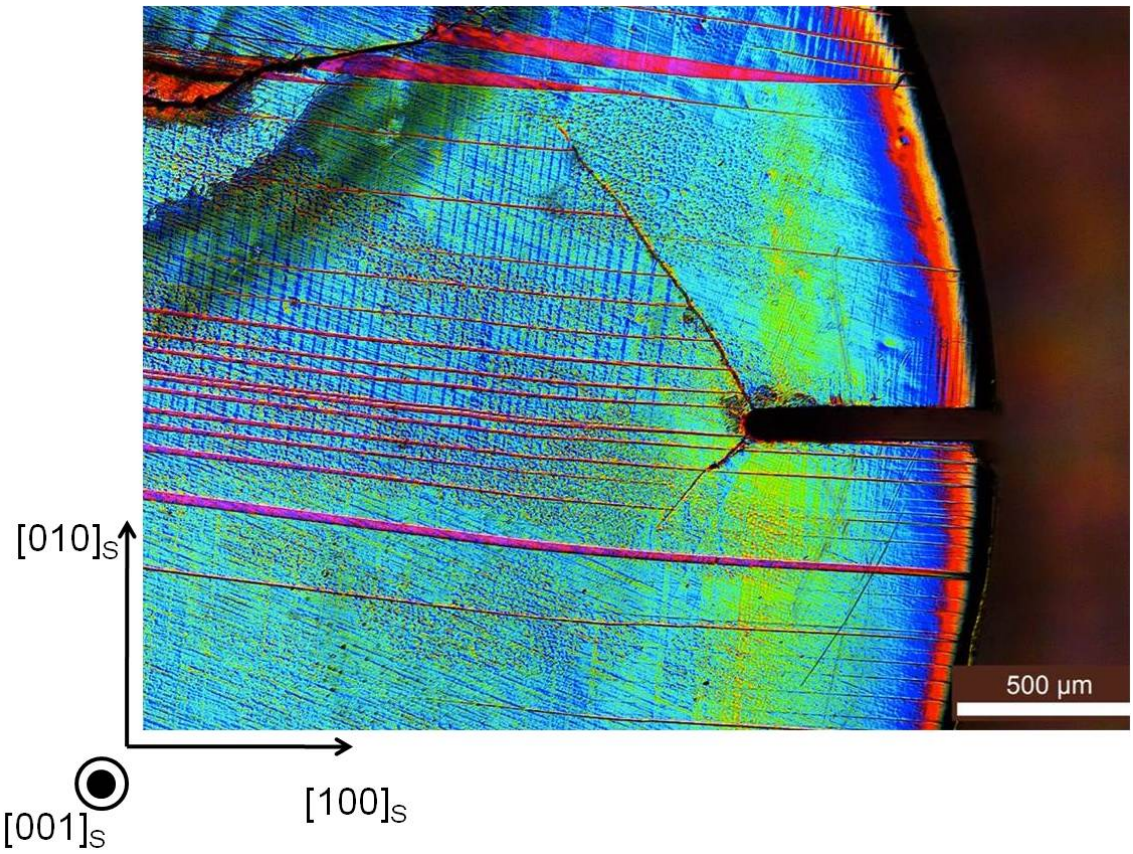

Figure 5.16 DIC microscopy image of CM154J after 10,000 revolutions. Cracks propagated in the $[\bar{1}10]_S$ and the $[\bar{1}\bar{1}0]_S$ directions outward from the $[100]_S$ notch.

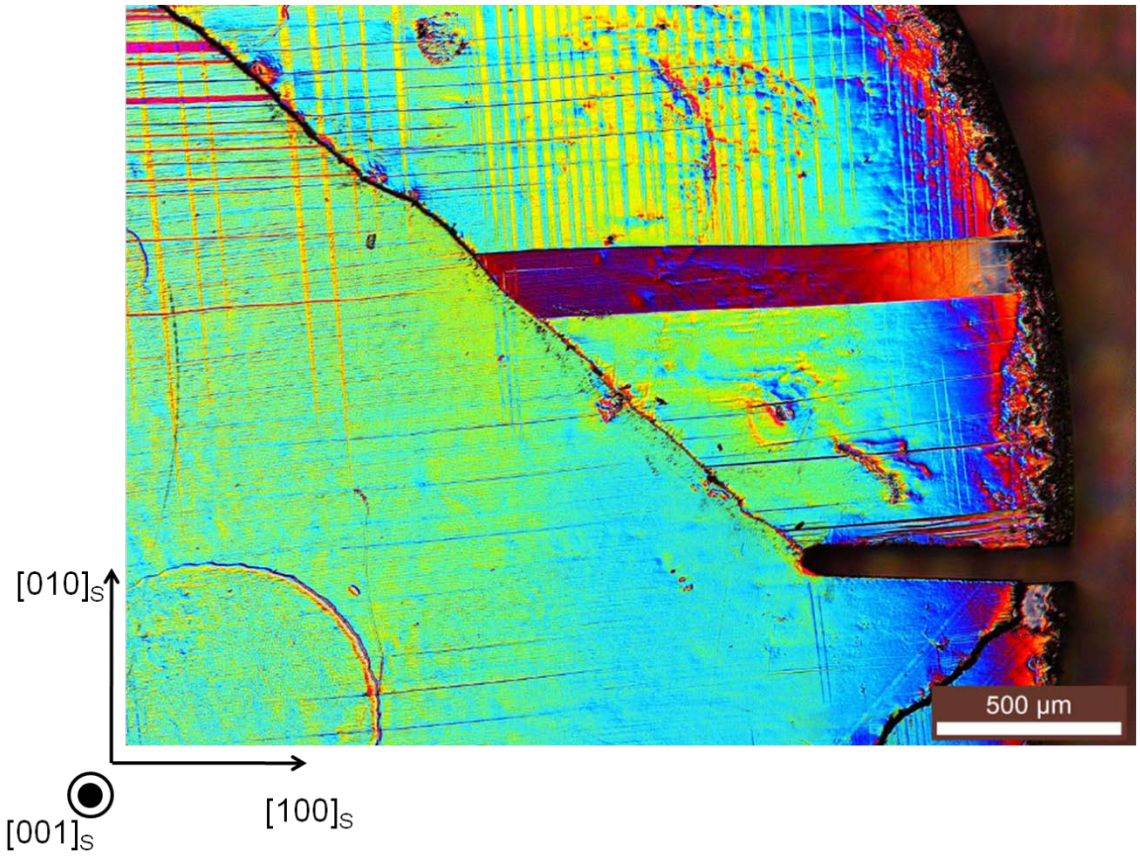

Figure 5.17 DIC microscopy image of CM154N after 10,000 revolutions. The fracture plane separates two active portions of the sample.

5.2.3 Microstructure

The twin structure near fracture surfaces were much more complex than in the bulk area which, was dominated by large mobile twins; see Figure 5.18. The large horizontal mobile twin boundaries are type II twin boundaries. Near the cracks, the twin structure is a mixture of type I and II twins. Type I twin boundaries are parallel to the $[100]_S$ direction while Type II twins deviate from $[100]_S$ by approximately 6^0 [33]. The twin structure near the fracture surfaces is refined with thinner twins, while the central area in between cracks contained thicker Type II twins.

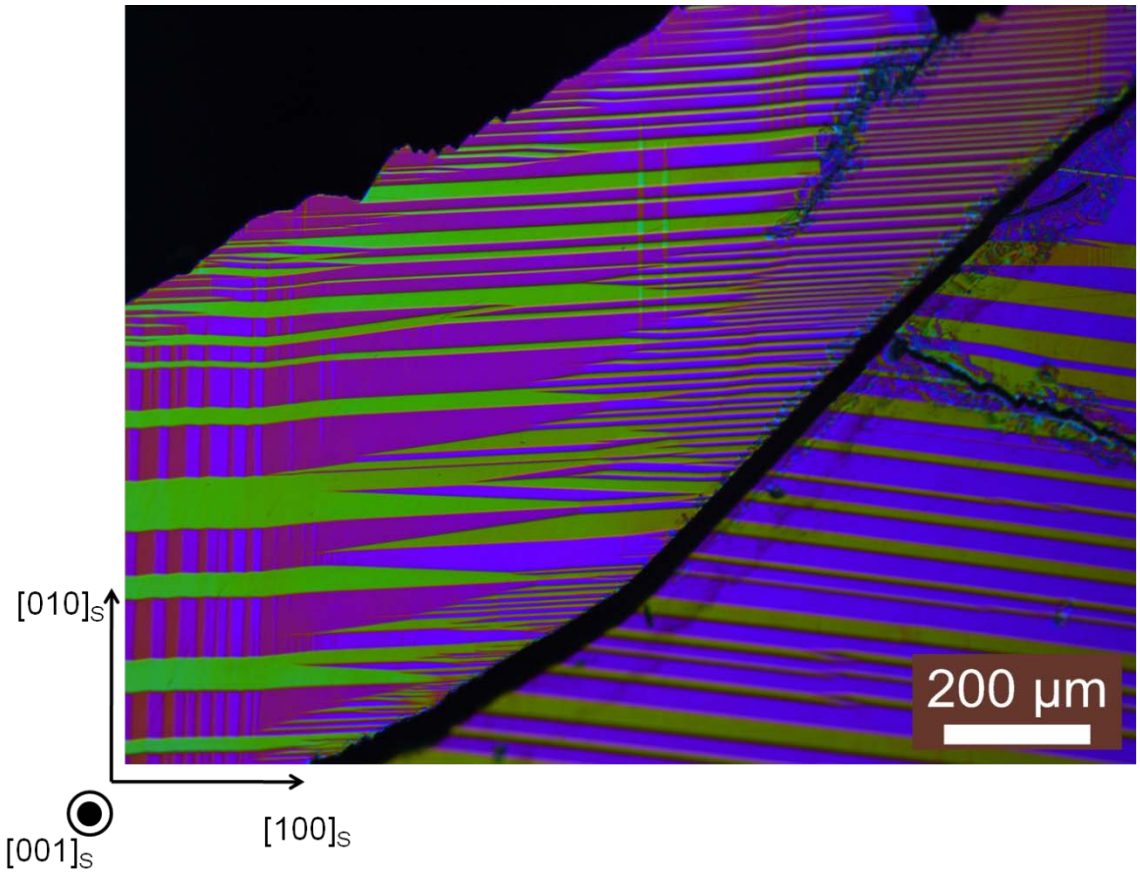

Figure 5.18 DIC microscopy image of CM132 E after 40,000 revolutions. Twin microstructure near fracture surface is composed of fine Type I and II twins. Farther away from the fracture surface, the active twin variants are relatively thicker Type II twins.

Compound twins run vertically and can only be seen in the single martensite variant where *c* is parallel to $[010]_S$ in Figure 5.19. The compound twin boundaries are visible in the pink and orange twins because the modulation directions in this orientation cause a surface relief of approximately 0.8° across the twinning plane [33]. Compound twin boundaries are not perfectly linear and do not extend across the entire sample. Near the ends of the boundaries, the edges form wedge-like domains; see Figure 5.20.The *c*-axis of the unit cell of the variants containing visible compound twins is oriented so that it is parallel to the face of the sample and in the $[010]_S$ direction [33]. The *c*-axis is perpendicular to the sample face in the $[001]_S$ direction in the variants where the

compound twins are not visible. The compound twins indicate domains containing different modulation directions of the unit cell.

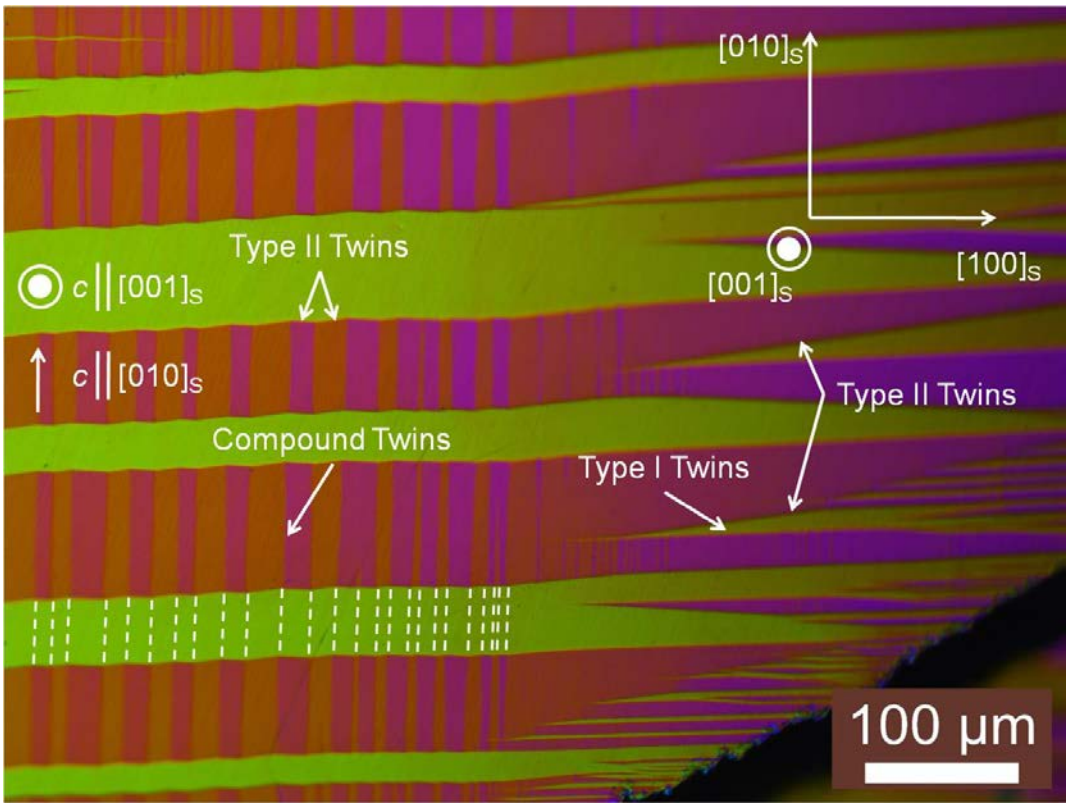

Figure 5.19 DIC microscopy image of CM132 E after 40,000 revolutions. Twin microstructure farthest from the fracture surface is composed of compound twins within thick type II twins. The compound twins are continuous and extend across the type II twin boundaries as indicated by the white dashed lines. Near the fracture surface the twins decompose into a mixture of type I and II twins. The *c*-axis of the unit cell is parallel to $[001]_S$ within the green twin and parallel to $[010]_S$ within the pink and orange twins.

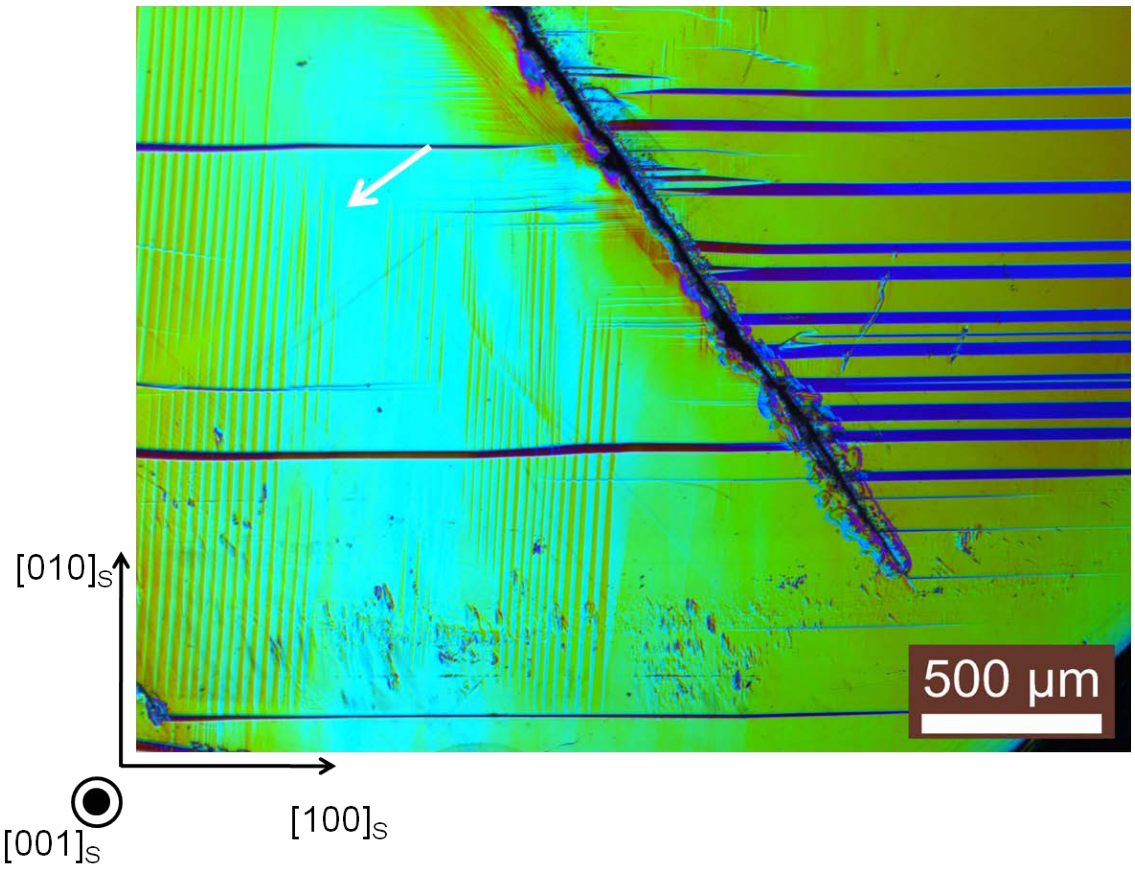

Figure 5.20 DIC microscopy image of CM132 F after 60,000 revolutions. The wedge shape of the vertical compound twins running parallel to $[010]_S$ can clearly be seen on the left side of the image indicated by the white arrow. The compound twins do not extend completely across the sample in the way that type I or II twins do.

The twin structure became highly refined with increased cycling. The larger twins decomposed into many thin twins. The microstructural areas with a large number of twin boundaries did not appear to evolve throughout testing while areas with large twins changed throughout testing; see Figure 5.21. Compound twins appeared in regions where they previously did not exist; see Figure 5.22. The compound twins developed perpendicularly to the active twin boundaries.

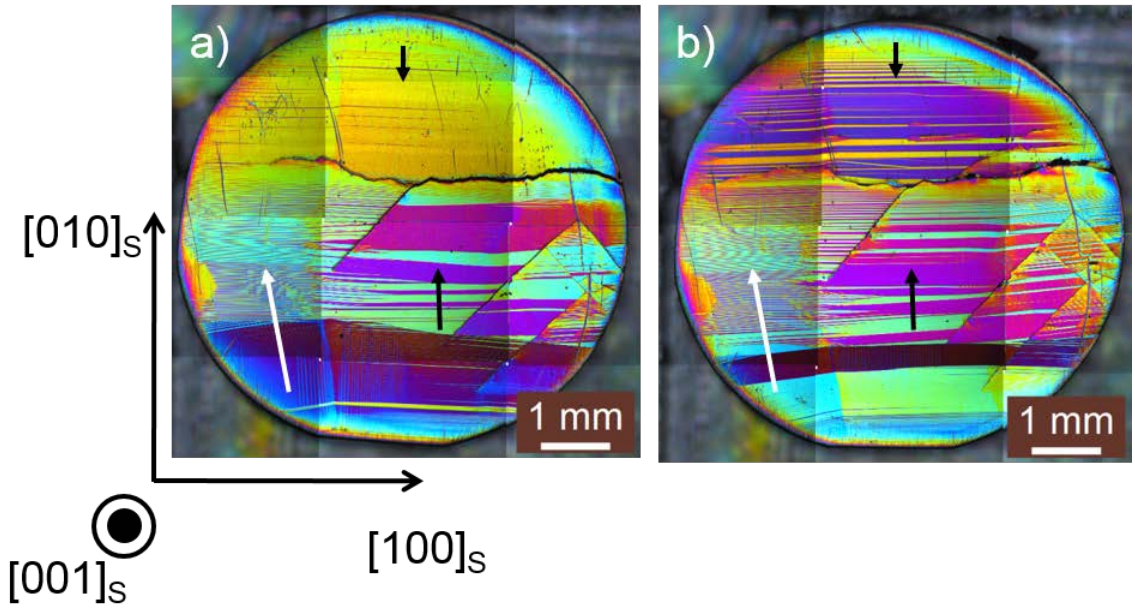

Figure 5.21 DIC microscopy mosaic images of CM154 A. a) Cycled to 10,000 revolutions. b) Cycled to 30,000 revolutions. The refined twin structure indicated by white arrows is composed of many thin twins and does not evolve through fatigue testing. The larger twins on the right side and top portion of the sample indicated by black arrows remain mobile.

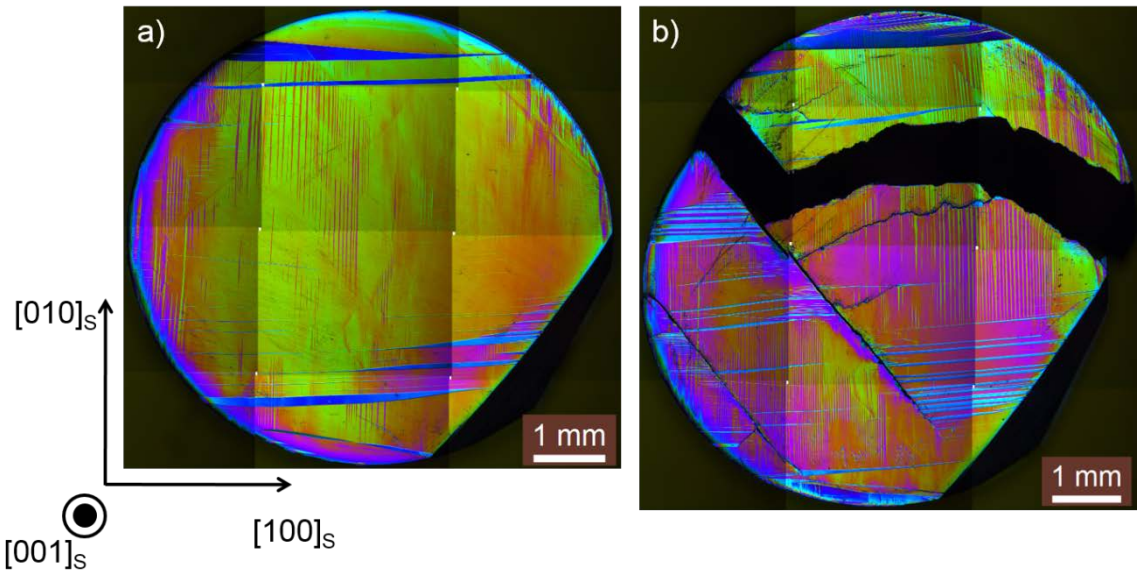

Figure 5.22 DIC microscopy images of CM132F. a) Image taken after 10,000 revolutions. b) Image taken after 70,000 revolutions. Compound twins developed in areas that they were previously absent. The compound twins were perpendicular to the active Type I and II twin boundaries.

5.2.4 Fatigue Life

When a sample disintegrated into many pieces or a portion larger than one-third of the sample fractured off, the sample was no longer cycled. Figure 5.23 presents the number of samples that reached a specified number of revolutions in the rotary fatigue instrument. The revolutions in the histogram were rounded to the nearest 10,000. A majority of the samples were cycled to failure in less than 100,000 revolutions. A small portion of samples lasted to more than 100,000. The largest number of samples only lasted to 20,000 revolutions, so the life of samples is relatively short and inconsistent.

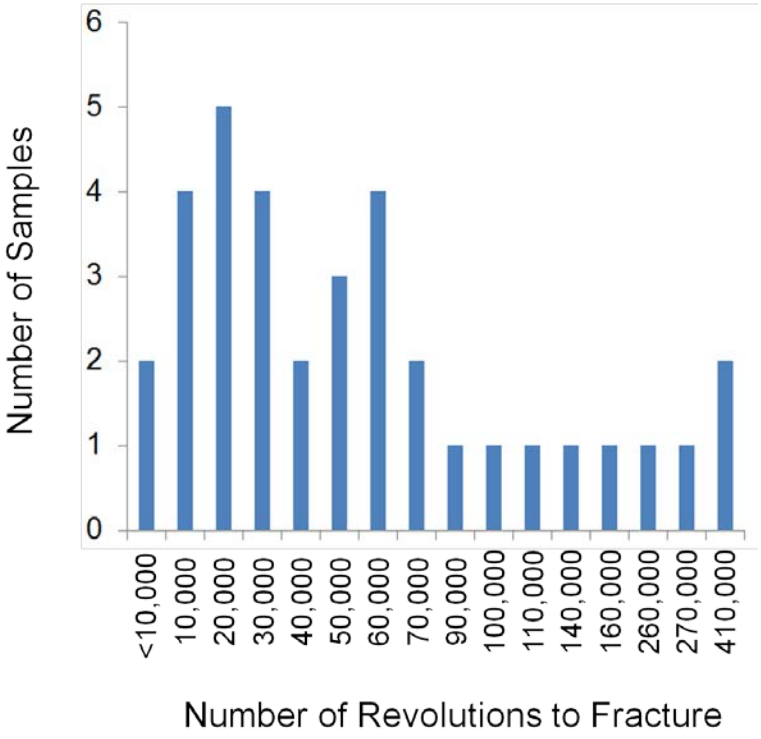

Figure 5.23 Diagram identifying the total number of samples reaching a threshold number of revolutions. The number of revolutions achieved per sample was rounded to the nearest 10,000 revolutions.

Three groups of surface roughness ranges were chosen to compare fatigue life; see Figure 5.24. Samples with average surface roughness lower than 30 nm tended to exhibit the highest fatigue life. The samples that had an average surface roughness

between 30 nm and 50 nm exhibited a median fatigue life. The samples that had the shortest average fatigue had surface roughness larger than 50 nm. Samples that were electropolished exhibited the highest average surface roughness due to pitting and samples that were mechanically polished with fine diamond slurry resulted in the lowest average surface roughness.

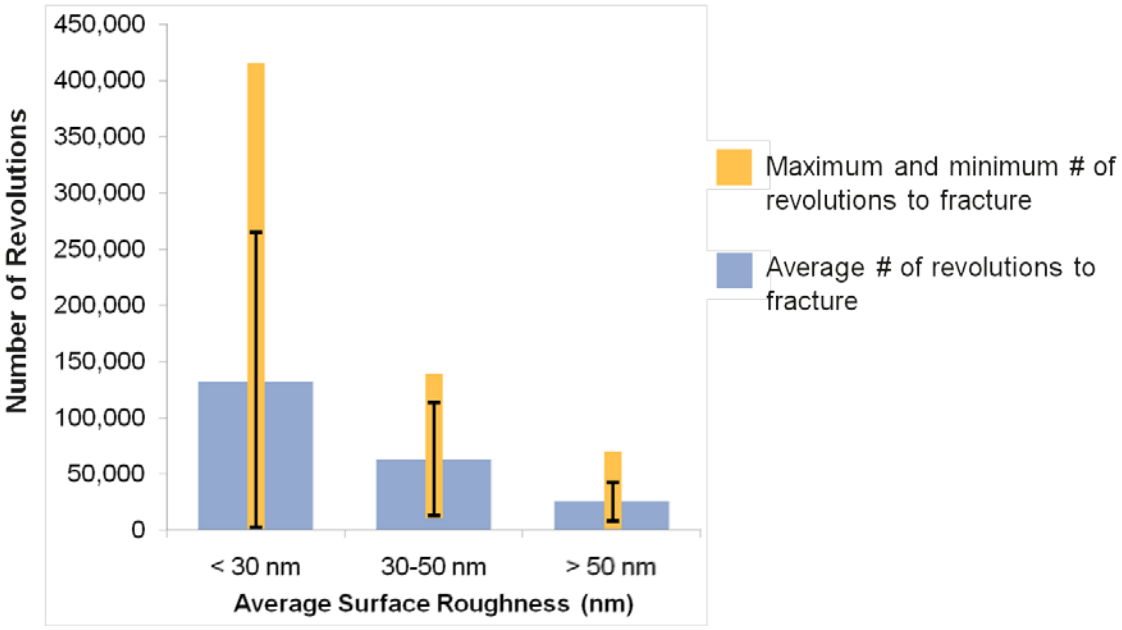

Figure 5.24 Diagram representing the average number of revolutions by samples with a specific average surface roughness indicated by the blue bars. The black error bars represent the standard deviation in the average. The minimum and maximum number of revolutions achieved by a sample in each group is represented by the gold bars.

CHAPTER SIX: DISCUSSION

When a sample has reached the limit of its fatigue life, there are many factors that prevent a twin variant from reorienting. Fracture planes interfere with twin boundaries moving throughout the sample, and therefore there is a higher stress fluctuation when the magnetic field oscillates from parallel to perpendicular to the easy axis of magnetization. The fracture surface hinders twin boundary motion and the twins require higher magnetic fields to initiate motion (Figure 5.15). Higher fields lead to higher field induced stress.

The average calculated magnetostress was the highest at 1.0 ± 0.3 MPa for electropolished samples. This is due to the high surface roughness relative to the other samples; see Figure 6.1. The high surface roughness required a higher switching field to initiate reorientation because twin boundaries tend to get pinned on areas with high stress concentrations [79].

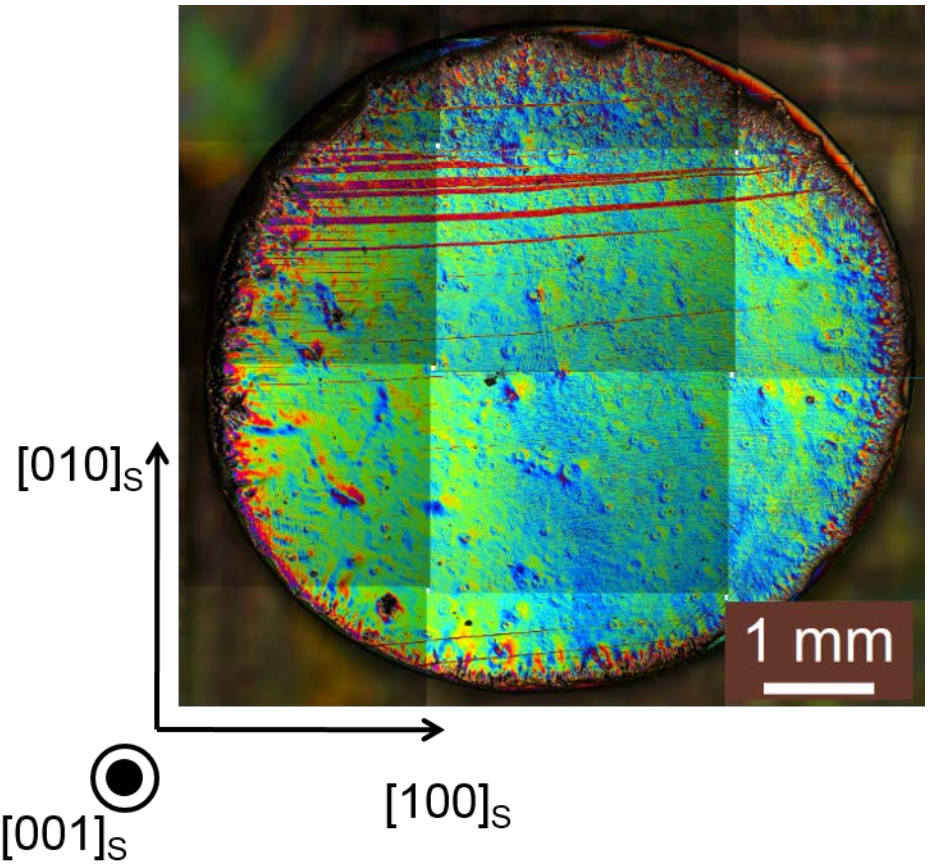

Figure 6.1 DIC mosaic image of CM154 Q after 10,000 cycles. CM154 Q was electropolished and the surface is rough and heavily pitted along the outer edge of the sample.

The range in strain in Aaltio's tests was 0.5-3.8% with crystals exhibiting a maximum strain of 6.5% [17, 72]. The crystal reaching the highest number of cycles, 2×10^9, was tested with a controlled strain of 2%, and other crystals tested at low strain as well lasted on the order of 10^6 cycles [17, 72]. By controlling and limiting the strain only, the twins with the highest mobility will be active contributing to a maximum reported stress of 2 MPa at the end of fatigue testing [17].

In rotary cycling with permanent magnets, the sample is allowed to expand to the maximum possible strain depending on the applied field and condition of the sample. Higher strain results in a longer range of motion in twin boundaries, exposing twinning

dislocations to a higher number of surface defects. This increases the probability of dislocations piling up at high local stress areas leading to crack initiation and propagation [15]. If a twin boundary is impeded, the stress in that twin increases up to the maximum magnetostress of about 3.5 MPa because the magnetic field applied is higher than the saturation magnetic field. If the force is strong enough to overcome the barrier, the twin boundary will move and the magnetostress will be relieved. If the magnetic field is not capable of reorienting the variant due to barriers, then the maximum effective magnetostress (Equation 3.9) will be imposed if the magnetic field, H is larger than H_s as is the case in the present experiments. This means an immobile twin in these samples will experience cyclical magnetostresses of approximately 3.5 MPa compared to the maximum stress reported in [17] measuring below 2 MPa. The stress is lower in strain controlled linearly actuated samples because the sample is not being elongated to its full potential minimizing the encounter of barriers to twin boundary motion.

Chmielus utilized rotary induced fatigue similar to this study, however fatigue life was reported to be over one-hundred million cycles at strains near 1% [19]. The sample in those experiments was constrained on both ends and therefore limited the maximum strain of the sample. In addition, samples that endured the highest amount of cycling started out with a finely twinned self-accommodated structure as opposed to magneto-mechanical and thermo-mechanically trained samples, which fail in as little as 1,000 cycles [15]. The un-trained samples developed a coarse mobile structure with mobile twins within the bulk. Near the constraints, the microstructure remained locked in place, limiting the maximum strain. Therefore, training that was effectively performed on

samples during measurement of magnetic properties prior to fatigue testing could have caused the low fatigue life of the samples.

In notched samples, the stress concentration is higher for the horizontal notches parallel to the [100] direction. Furthermore, the [100] notches are located closer to the bulk motion of twin boundaries within the center of the crystal. The cracks propagated from these notches for a majority of the samples as opposed to the [110] notches. A refined twin structures near defects are indicative of areas with high stress concentrations; see Figure 6.2. The notch induced stress concentrations in the material as indicated by the preferential crack propagation at the notch tip.

At higher cycles a majority of the samples exhibited increased magnetostress at lower applied magnetic fields. This is due to hardening of the material from twinning dislocation pile-up near areas of high stress concentration. Some samples did exhibit a softening, meaning the switching field and magnetostress decreased at higher revolutions due to training in the sample. A larger collection of samples should be tested to higher revolutions to create a better statistical analysis of hardening through fatigue testing.

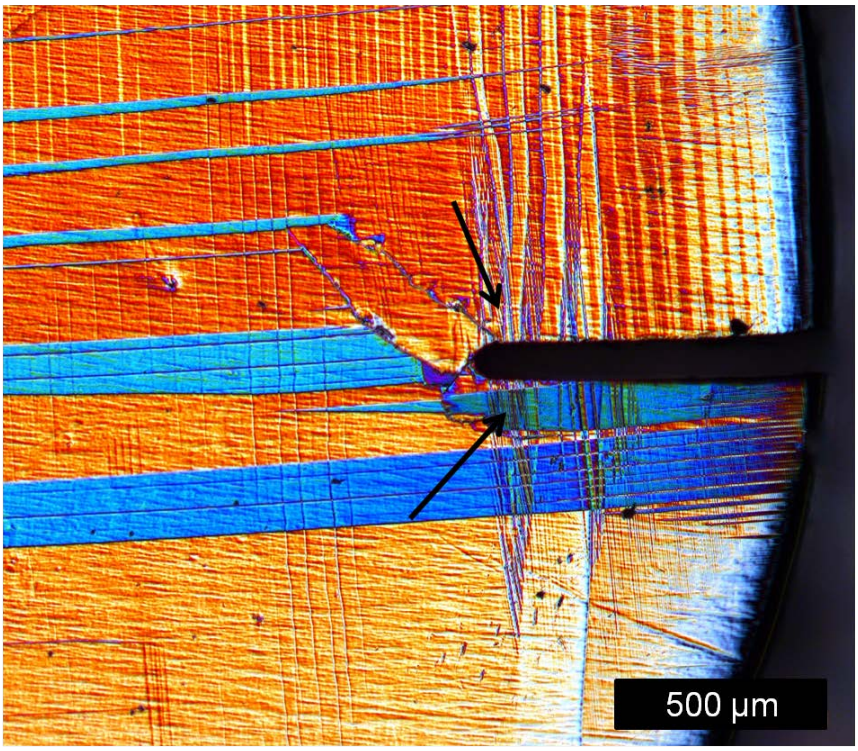

Figure 6.2 DIC image of CM154 L after 12,000 cycles. The twin structure near the notch is refined containing Type I and II twin boundaries in a variety of orientations; location indicated by black arrows. The twin structure within the bulk material contains larger mobile twins.

The twin structure becomes complex near fracture surfaces and SAGBs. Near areas of high stress concentration, the microstructure evolves into a refined structure in order to accommodate for the stress increase and results in localized stress concentrations. This refined structure presents obstacles for the motion of the mobile twin boundaries. The refined twin structure prevents reorientation due to high concentrations of twinning dislocations, resulting in higher cyclical effective stress in immobile twins and resulting in crack formation.

The SAGBs do not appear to completely hinder twin boundary motion. As a twin crosses an SAGB, it has been observed as breaking up into many smaller twins. The higher number of twin boundaries located on the SAGB will lead to higher localized stress concentrations due to an increased number of twinning dislocations. The twinning

plane can also kink across a SAGB, which involves heavy distortion of the unit cells locally at the SAGB. These areas of high stress concentration lead to crack formation and growth.

The fatigue life in samples magnetomechanically cycled in the rotary testing instrument experienced low fatigue life due to a number of factors. DIC microscopy indicated that the microstructure of the samples was not completely symmetrical indicating that the samples were not perfect single crystals, but contained a small number of SAGBs. High surface roughness due to pitting or mechanical polishing marks resulted in high concentrations of stress, inducing a complex twin structure and piling up of twinning dislocations. The high concentration of dislocations increased the probability for crack nucleation and propagation. There is an indication that high surface roughness leads to shorter fatigue life (Figure 5.24), however more data is required to perform a detailed quantitative analysis. There is a large range of the fatigue life between samples within each arbitrary surface roughness group leading to higher error and overlap between the groupings.

The conditions for Ni-Mn-Ga actuators to exhibit long fatigue life include improving crystal quality through optimizing crystal growth and to minimize or eliminate SAGBs and internal defects. It is important to prepare samples with the highest quality surface treatment available to reduce high stress concentration areas. Training should be minimized to prevent large mobile twins and large strains. A refined twin structure can be stabilized via coating samples in TiN, coating with an elastomer, or ion implantation [80]. Finally, by controlling strain through the use of constraints or localized MFIS, samples can be expected to exhibit longer fatigue live.

CHAPTER SEVEN: CONCLUSIONS

A testing device was developed to simultaneously expose many samples to a rotating field while minimally constraining the samples. Ni-Mn-Ga single crystals were cycled in a rotating magnetic field to determine the fatigue life and fracture mechanics of samples with minimal constraints to allow for large actuation strains. 45 samples were prepared with different surface treatments to determine the effect of surface roughness on fatigue life. A rotating magnetic field was used to induce actuation in order to mimic the method that would be used in commercial applications. Notched samples indicated that cracks will initiate in areas of high local stress concentration. Magnetomechanicaly cycled samples experienced low fatigue life due to a number of factors. DIC microscopy indicated that the microstructure of the samples was not completely symmetrical, indicating that the samples were not perfect single crystals, but contained a small number of SAGBs. There is an indication that samples with lower surface roughness exhibit a longer fatigue life, however more data is required to perform a detailed statistical analysis. A highly mobile twin structure and unconstrained twin boundary motion resulted in a higher propensity for crack propagation. The fatigue life of Ni-Mn-Ga MSMAs exposed to a rotating field is highly sensitive to stress concentrations. To achieve a long fatigue life, Ni-Mn-Ga crystals must be free of defects such as notches, small angle grain boundaries, and other sources of stress concentrations.

CHAPTER EIGHT: FUTURE WORK

The quality of single crystals plays an important role in fatigue life. Single crystals used in this thesis appeared to contain SAGBs that impacted the fracture mechanisms and microstructure. An effort must be made to understand why the single crystals grown in this thesis exhibited SAGBs. Highly perfect crystals are required to minimize stresses within the crystal and interaction with twin boundaries. Areas that should be investigated are growth speed, temperature of the bottom of the seed before the crystal is driven out of the furnace, and the effect of using different materials in place of the steel and copper spacers to increase the temperature gradient at the solidification front.

In terms of gaining a more quantitative understanding of surface roughness on fatigue life, the number of samples tested should be increased. The quality of the surface of the samples also needs to be more uniform. The electropolishing process needs to be refined because the result from electropolishing in this study produced surfaces that were heavily pitted, leading to high surface roughness.

In applications like a micro-pump, the sample is constrained on its ends and the MFIS is induced locally. It is necessary to prove the reliability of these applications, so it would be helpful to be able to perform fatigue testing of actual working devices. However, the devices are time intensive to construct, so preliminary testing on large numbers of stand-alone samples will be more beneficial in the short term.

REFERENCES

[1] D. Jiles, *Introduction to magnetism and magnetic materials*: CRC, 1998.

[2] K. Ullakko, J. K. Huang, C. Kantner, R. C. O'Handley, and V. V. Kokorin, "Large magneticfieldinduced strains in Ni2MnGa single crystals," *Applied Physics Letters,* vol. 69, p. 1966, 1996.

[3] A. G. Olabi and A. Grunwald, "Design and application of magnetostrictive materials," *Materials & Design,* vol. 29, pp. 469-483, 2008.

[4] A. Sozinov, N. Lanska, A. Soroka, and W. Zou, "12% magnetic field-induced strain in Ni-Mn-Ga-based non-modulated martensite," *Applied Physics Letters,* vol. 102, p. 021902 2013.

[5] R. C. O'Handley, S. J. Murray, M. Marioni, H. Nembach, and S. M. Allen, "Phenomenology of giant magnetic-field-induced strain in ferromagnetic shape-memorymaterials (invited)," *Journal of Applied Physics,* vol. 87, pp. 4712-4717, 2000.

[6] K. Ullakko, L. Wendell, A. Smith, P. Müllner, and G. Hampikian, "A magnetic shape memory micropump:contact-free, and compatible with PCR and human DNA profiling," *Smart Materials and Structures,* vol. 21, p. 115020, 2012.

[7] M. Chmielus, X. X. Zhang, C.Witherspoon, D. C. Dunand, and P. Müllner, "Giant magnetic-field-induced strains in polycrystalline Ni–Mn–Ga foams," *Nature Materials,* vol. 8, p. 863, 2009.

[8] N. M. Bruno, C. Ciocanel, H. P. Feigenbaum, and A. Waldauer, "A theoretical and experimental investigation of power harvesting using the NiMnGa martensite reorientation mechanism," *Smart Materials and Structures,* vol. 21, p. 094018, 2012.

[9] C. S. Watson, C. Hollar, K. Anderson, W. B. Knowlton, and P. Müllner, "Magnetomechanical Four-State Memory," *Advanced Functional Materials,* vol. 23, pp. 3995-4001, 2013.

[10] A. N. Vasil'ev, A. D. Bozhko, V. V. Khovailo, I. E. Dikshtein, V. G. Shavrov, V. D. Buchelnikov, *et al.*, "Structural and magnetic phase transitions in shape-memory alloys Ni_{2+x} Mn_{1-x} Ga," *Physical Review B* vol. 59, p. 1113, 1999.

[11] V. A. Chernenko, J. Pons, C. Seguí, and E. Cesari, "Premartensitic phenomena and other phase transformations in Ni–Mn–Ga alloys studied by dynamical mechanical analysis and electron diffraction," *Acta Materialia,* vol. 50, pp. 53-60, 2002.

[12] E. Pagounis, R. Chulist, M. J. Szczerba, and M. Laufenberg, "Over 7% magnetic field-induced strain in a Ni-Mn-Ga five-layered martensite," *Applied Physics Letters* vol. 105, p. 052405, 2014.

[13] A. Sozinov, A. A. Likhachev, N. Lanska, O. Söderberg, K. Ullakko, and V. K. Lindroosa, "Stress and magnetic-field-induced variant rearrangement in Ni–Mn–

Ga single crystals with seven-layered martensitic structure," *Materials Science and Engineering: A,* vol. 378, pp. 399–402, 2004.

[14] X. Zhou, W. Li, H. P. Kunkel, and G. Williams, "A criterion for enhancing the giant magnetocaloric effect: (Ni–Mn–Ga)—a promising new system for magnetic refrigeration," *Journal of Physics: Condensed Matter,* vol. 16, p. L39, 2004.

[15] P. Müllner, V. A. Chernenko, D. Mukherji, and G. Kostorz, "Cyclic magnetic-field -induced deformation and magneto-mechanical fatigue of Ni-Mn-Ga ferromagnetic martensites," in *MRS Proceedings*, 2003.

[16] S. A. Wilson, R. P. J. Jourdain, Q. Zhang, R. A. Dorey, C. R. Bowen, M. Willander, *et al.*, "New materials for micro-scale sensors and actuators: An engineering review," *Materials Science and Engineering: R: Reports,* vol. 56, pp. 1-129, 2007.

[17] I. Aaltio, A. Soroka, Y. Ge, O. Söderberg, and S.-P. Hannula, "High-cycle fatigue of 10M Ni–Mn–Ga magnetic shape memory alloy in reversed mechanical loading " *Smart Materials and Structures,* vol. 19, p. 075014, 2010.

[18] I. Aaltio, O. Söderberg, Y. Ge, and S.-P. Hannula, "Long-Term Cyclic Loading of 10M Ni-Mn-Ga Alloys," *Materials Science Forum,* vol. 684, pp. 203-214, 2011.

[19] M. Chmielus, V. A. Chernenko, W. B. Knowlton, G. Kostorz, and P. Müllner, "Training, constraints, and high-cycle magneto-mechanical properties of Ni-Mn-Ga magnetic shape-memory alloys," *The European Physical Journal Special Topics,* vol. 158, pp. 79-85, 2008.

[20] "magnetic susceptibility," in *Encyclopaedia Britannica. Encyclopaedia Britannica Online*, ed: Encyclopædia Britannica Inc., 2014.

[21] W. Palmer, "Magnetocrystalline Anisotropy of Magnetite at Low Temperature," *Physical Review,* vol. 131, pp. 1057-1062, 1963.

[22] G. B. Kauffman and I. Mayo, "The Story of Nitinol: The Serendipitous Discovery of the Memory Metal and Its Applications," *The Chemical Educator,* vol. 2, p. 1, 1997.

[23] S. A. Thompson, "An overview of nickel–titanium alloys used in dentistry," *International Endodontic Journal,* vol. 33, p. 297, 2000.

[24] K. Bhattacharya, *Microstructure of Martensite*. New York: Oxford University Press Inc., 2003.

[25] J. S. Bowles, "The crystallography of martensite transformations III. Face-centred cubic to body-centred tetragonal transformations," *Acta Metallurgica,* vol. 2, p. 224, 1954.

[26] V. V. Khovailo, V. Novosad, T. Takagi, D. A. Filippov, R. Z. Levitin, and A. N. Vasil’ev, "Magnetic properties and magnetostructural phase transitions in Ni2+x Mn1−x Ga shape memoryalloys," *Physical Review B,* vol. 70, p. 174413, 2004.

[27] B. Verlinden, J. Driver, I. Samajdar, and R. D. Doherty, *Thermo-Mechanical Processing of Metallic Materials*. Linacre House, Jordan Hill, Oxvord OX2 8DP, UK: Elsevier, 2007.

[28] P. Müllner and A. H. King, "Deformation of hierarchically twinned martensite," *Acta Materialia,* vol. 58, pp. 5242-5261, 2010.

[29] A. Kelly, G. W. Groves, and P. Kidd, *Crystallography and Crystal Defects*. Baffins Lane, Chichester, West Sussex, PO19 1UD, England: John Wiley and Sons Ltd., 2000.

[30] F. C. Frank and J. H. v. d. Merwe, "One-Dimensional Dislocations. I. Static Theory," *Proceedings of the Royal Society of London Series a-Mathematical andPhysical Sciences,* vol. 198, pp. 205-216, 1949.

[31] P. Müllner, V. A. Chernenko, and G. Kostorz, "A microscopic approach to the magnetic-field-induced deformation of martensite (magnetoplasticity)," *Journal of Magnetism and Magnetic Materials,* vol. 267, pp. 325-334, 2003.

[32] R. Chulist, L. Straka, N. Lanska, A. Soroka, A. Sozinov, and W. Skrotzki, "Characterization of mobile type I and type II twin boundaries in 10M modulated Ni–Mn–Ga martensite by electron backscatter diffraction," *Acta Materialia,* vol. 61, pp. 1913-1920, 2013.

[33] L. Straka, O. Heczko, H. Seiner, N. Lanska, J. Drahokoupil, A. Soroka, *et al.*, "Highly mobile twinned interface in 10M modulated Ni–Mn–Ga martensite: Analysis beyond the tetragonal approximation of lattice," *Acta Materialia,* vol. 59, pp. 7450-7463, 2011.

[34] L. Straka, A. Soroka, H. Seiner, H. Hänninen, and A. Sozinov, "Temperature dependence of twinning stress of Type I and Type II twins in 10M modulated Ni-Mn-Ga martensite," *Scripta Materialia,* vol. 67, pp. 25-28, 2012.

[35] A. Sozinov, N. Lanska, A. Soroka, and L. Straka, "Highly mobile type II twin boundary in Ni-Mn-Ga five-layered martensite," *Applied Physics Letters* vol. 99, p. 124103, 2011.

[36] H. E. Karaca, I. Karaman, B. Basaran, Y. I. Chumlyakov, and H. J. Maier, "Magnetic field and stress induced martensite reorientation in NiMnGa ferromagnetic shape memory alloy single crystals," *Acta Materialia,* vol. 54, pp. 233-245, 2006.

[37] V. V. Kokorin, V. V. Martynov, and V. A. Chernenko, "Stress - induced martensitic transformations in Ni_2MnGa," *Scripta Metallurgica et Materialia,* vol. 26, pp. 175-177, 1992.

[38] M. A. Marioni, R. C. O'Handley, and S. M. Allen, "Pulsed magnetic field-induced actuation of Ni–Mn–Ga single crystals," *Applied Physics Letters,* vol. 83, pp. 3966-3968, 2003.

[39] P. Müllner, V. A. Chernenko, M. Wollgarten, and G. Kostorz, "Large cyclic deformation of a Ni-Mn-Ga shape memory alloy induced by magnetic fields," *Journal of Applied Physics,* vol. 92, p. 6708, 2002.

[40] A. A. Likhachev and K. Ullakko, "Magnetic-field-controlled twin boundaries motion and giant magneto-mechanical effects in Ni–Mn–Ga shape memory alloy," *Physics Letters A,* vol. 275, pp. 142-151, 2000.

[41] A. A. Likhachev and K. Ullakko, "Quantitative model of large magnetostrain effect in ferromagnetic shapell memory alloys," *The European Physical Journal B - Condensed Matter and Complex Systems,* vol. 14, pp. 263-267, 2000.

[42] R. C. O'Handley, "Model for strain and magnetization in magnetic shape-memory alloys," *Journal of Applied Physics,* vol. 83, pp. 3263-3270, 1998.

[43] V. A. Chernenko, V. A. L'vov, and E. Cesari, "Martensitic transformation in ferromagnets: experiment and theory " *Journal of Magnetism and Magnetic Materials,* vol. 196-197, pp. 859-860, 1999.

[44] V. A. L'vov, E. V. Gomonaj, and V. A. Chernenko, "A phenomenological model of ferromagnetic martensite," *Journal of Physics: Condensed Matter,* vol. 10, pp. 4587–4596, 1998.

[45] V. A. L'vov, S. P. Zagorodnyuk, and V. A. Chernenko, "A phenomenological theory of giant magnetoelastic responsein martensite," *The European Physical Journal B,* vol. 27, pp. 55-62, 2002.

[46] V. Chernenko, V. L'vov, E. Cesari, and P. McCormick, "Effect of Magnetic Field on Phase Transformations in MnAs and Ni_2MnGa Compounds," *Materials Transactions,* vol. 8, pp. 928-932, 2000.

[47] V. A. Chernenko, V. A. L'vov, P. Müllner, G. Kostorz, and T. Takagi, "Magnetic-field-induced superelasticity of ferromagnetic thermoelastic martensites: Experiment and modeling," *Physical Review B,* vol. 69, p. 134410, 2004.

[48] V. Chernenko, V. L'Vov, E. Cesari, J. Pons, R. Portier, and S. Zagorodnyuk, "New aspects of structural and magnetic behaviour of martensites in Ni-Mn-Ga alloys," *Materials Transactions,* vol. 43, pp. 856-860, 2002.

[49] F. Heusler, W. Starck, and E. Haupt, "Uber magnetische Manganlegrierungen," *Verhandlungen der Deutschen Physikalischen Gesellschaft,* vol. 5, 1903.

[50] P. J. Webster, "Heusler Alloys," *Journal of Contemporary Physics,* vol. 10, p. 559, 1969.

[51] P. J. Webster and K. R. A. Ziebeck, "Magnetic and chemical order in Heusler alloys containing cobalt and titanium," *Journal of Physics and Chemistry of Solids,* vol. 34, p. 1647, 1972.

[52] F. A. Hames, "Ferromagnetic-Alloy Phases Near the Compositions Ni2MnIn,Ni2MnGa, Co2MnGa, Pd2MnSb, and PdMnSb," *Journal of Applied Physics,* vol. 31, pp. s370-s371, 1960.

[53] P. J. Webster, K. R. A. Ziebeck, S. L. Town, and M. S. Peak, "Magnetic order and phase transformation in Ni_2MnGa," *Philosophical Magazine Part B,* vol. 49, pp. 295-310, 1984.

[54] J. Pons, V. A. Chernenko, R. Santamarta, and E. Cesari, "Crystal structure of martensitic phases in Ni–Mn–Ga shape memory alloys," *Acta Materialia* vol. 48, pp. 3027–3038, 2000.

[55] L. Righi, F. Albertini, L. Pareti, A. Paoluzi, and G. Calestani, "Commensurate and incommensurate ‘‘5M’’ modulated crystal structures in Ni–Mn–Ga martensitic phases " *Acta Materialia,* vol. 55, pp. 5237–5245, 2007.

[56] L. Righi, F. Albertini, E. Villa, A. Paoluzi, G. Calestani, V. Chernenko, *et al.*, "Crystal structure of 7M modulated Ni–Mn–Ga martensitic phase," *Acta Materialia,* vol. 56, pp. 4529–4535, 2008.

[57] O. Heczko, A. Sozinov, and K. Ullakko, "Giant field-induced reversible strain in magnetic shape memory NiMnGa alloy," *Magnetics, IEEE Transactions,* vol. 36, pp. 3266-3268, 2000.

[58] S. J. Murray, M. Marioni, S. M. Allen, and R. C. O'Handley, "6% magnetic-field-induced strain by twin-boundary motionin ferromagnetic Ni–Mn–Ga," *Applied Physics Letters,* vol. 77, p. 886, 2000.

[59] A. Sozinov, A. A. Likhachev, N. Lanska, O. Söderberg, K. Ullakko, and V. K. Lindroos, "Effect of crystal structure on magnetic-field-induced strain in Ni-Mn-

Ga," in *Smart Structures and Materials 2003: Active Materials: Behavior and Mechanics*, 2003, pp. 586-594.

[60] A. Sozinov, A. A. Likhachev, N. Lanska, and K. Ullakko, "Giant magnetic-field-induced strain in NiMnGa seven-layeredmartensitic phase," *Applied Physics Letters*, vol. 80, pp. 1746-1748, 2002.

[61] L. Straka and O. Heczko, "Magnetic anisotropy in Ni–Mn–Ga martensites," *Journal of Applied Physics*, vol. 93, pp. 8636-8638, 2003.

[62] O. Heczko, L. Straka, and K. Ullakko, "Relation between structure, magnetization process and magnetic shape memory effect of various martensites occurring in Ni-Mn-Ga alloys," *Journal of Physics IV France*, vol. 112, p. 959, 2003.

[63] P. Mullner, V. A. Chernenko, and G. Kostorz, "Large cyclic magnetic-field-induced deformation in orthorhombic (14M) Ni–Mn–Ga martensite," *Journal of Applied Physics*, vol. 95, p. 1531, 2004.

[64] A. Sozinov, A. A. Likhachev, N. Lanska, and K. Ullakko, "Giant magnetic-field-induced strain in NiMnGa seven-layered martensitic phase," *Applied Physics Letters*, vol. 80, p. 1746, 2002.

[65] A. Sozinov, A. A. Likhachev, and K. Ullakko, "Crystal Structures and Magnetic Anisotropy Properties of Ni–Mn–Ga Martensitic Phases With Giant Magnetic-Field-Induced Strain " *IEEE Transactions on Magnetics*, vol. 38, pp. 2814-2816, 2002.

[66] N. Lanska, O. Söderberg, A. Sozinov, Y. Ge, K. Ullakko, and V. K. Lindroos, "Composition and temperature dependence of the crystal structure of Ni–Mn–Ga alloys," *Journal of Applied Physics*, vol. 95, pp. 8074-8078, 2004.

[67] P. Müllner, V. A. Chernenko, and G. Kostorz, "Large magnetic-field-induced deformation and magneto-mechanical fatigue of ferromagnetic Ni–Mn–Ga martensites," *Materials Science and Engineering: A*, vol. 387-389, pp. 965-968, 2004.

[68] P. Müllner, V. A. Chernenko, D. Mukherji, and G. Kostorz, "Cyclic magnetic-field -induced deformation and magneto-mechanical fatigue of Ni-Mn-Ga ferromagnetic martensites," in *MRS Proceedings*, 2003, p. 785.

[69] I. Aaltio, O. Söderberg, Y. Ge, and S.-P. Hannula, "Twin boundary nucleation and motion in Ni–Mn–Ga magnetic shape memory material with a low twinning stress," *Scripta Materialia*, vol. 62, pp. 9-12, 2010.

[70] A. A. Cherechukin, V. V. Khovailo, R. V. Koposov, E. P. Krasnoperov, T. Takagi, and J. Tani, "Training of the Ni–Mn–Fe–Ga ferromagnetic shape-memory alloys due cycling in high magnetic field," *Journal of Magnetism and Magnetic Materials*, vol. 258–259, pp. 523-525, 2003.

[71] M. Chmielus, I. Glavatskyy, J.-U. Hoffmann, V. A. Chernenko, R. Schneider, and P. Müllner, "Influence of constraints and twinning stress on magnetic field-induced strain of magnetic shape-memory alloys," *Scripta Materialia*, vol. 64, pp. 888-891, 2011.

[72] I. Aaltio, Y. Ge, H. Pulkkinen, A. Sjöberg, O. Söderberg, X. W. Liu, *et al.*, "Crack growth of 10M Ni-Mn-Ga material in cyclic mechanical loading " *Physics Procedia*, vol. 10, pp. 87-93, 2010.

[73] P. Lázpita, G. Rojo, J. Gutiérrez, J. M. Barandiaran, and R. C. O'Handley, "Correlation Between Magnetization and Deformation in a NiMnGa Shape Memory Alloy Polycrystalline Ribbon," *Sensor Letters*, vol. 5, p. 65, 2007.

[74] R. W. Overholser, M. Wuttig, and D. A. Neumann, "Chemical ordering in Ni-Mn-Ga Heusler alloys," *Scripta Materialia*, vol. 40, pp. 1095–1102, 1999.

[75] D. Kellis, A. Smith, K. Ullakko, and P. Müllner, "Oriented single crystals of Ni–Mn–Ga with very low switching field," *Journal of Crystal Growth*, vol. 359, pp. 64-68, 2012.

[76] H. Schneider and S. Komarneni, *Mullite*. Germany: Wiley-VCH Verlag GmbH & Co., 2006.

[77] G. Erdelyi, H. Mehrer, A. W. Imre, T. A. Lograsso, and D. L. Schlagel, "Self-diffusion in Ni_2MnGa," *Intermetallics*, vol. 15, pp. 1078-1083, 2007.

[78] A. Smith, J. Tellinen, P. Müllner, and K. Ullakko, "Controlling twin variant configuration in a constrained Ni–Mn–Ga sample using local magnetic fields," *Scripta Materialia*, vol. 77, pp. 68-70, 2014.

[79] M. Chmielus, K. Rolfs, R. Wimpory, W. Reimers, P. Müllner, and R. Schneider, "Effects of surface roughness and training on the twinning stress of Ni–Mn–Ga single crystals," *Acta Materialia*, vol. 58, pp. 3952-3962, 2010.

[80] K. Ullakko, M. Chmielus, and P. Müllner, "Stabilizing a fine twin structure in Ni–Mn–Ga samples by coatings and ion implantation," *Scripta Materialia*, 2014.

APPENDIX

The following tables present the average compositions of the 10M portions of the single crystals used in experiments as well as the average composition over the entire length of the crystal. The large error associated with Table A.2 is due to chemical segregation of the crystal at the end farthest away from the seed.

Table A.1 Average composition (atomic-%) over the length of the 10M portions of single crystals used in fatigue tests and compression tests.

Single Crystal	Ni	Mn	Ga
CM132	50.6 ± 0.2	26.6 ± 0.5	22.9 ± 0.4
CM142	51.1 ± 0.2	24.8 ± 0.3	24.1 ± 0.2
CM143	51.1 ± 0.2	25.1 ± 0.4	23.9 ± 0.2
CM154	51.3 ± 0.2	25.7 ± 0.5	23.0 ± 0.4
CM158	51.6 ± 0.6	26.4 ± 0.3	22.0 ± 0.3
CM161	51.5 ± 0.2	26.4 ± 0.5	22.1 ± 0.4

Table A.2 Average composition (atomic-%) over the entire length of the crystals used in fatigue tests and compression tests.

Single Crystal	Ni	Mn	Ga
CM132	49.5 ± 1.7	29.3 ± 3.2	21.3 ± 1.6
CM142	50.4 ± 0.8	26.9 ± 2.3	22.7 ± 1.5
CM143	50.4 ± 0.8	27.1 ± 2.4	22.5 ± 1.6
CM154	50.6 ± 1.3	27.5 ± 2.9	21.9 ± 1.7
CM158	51.7 ± 0.3	26.1 ± 0.5	22.2 ± 0.3
CM161	50.9 ± 0.7	27.7 ± 1.6	21.3 ± 1.0

The following diagrams include XRD and EDS data for single crystals that were used in testing and not presented previously in the main body of this thesis.

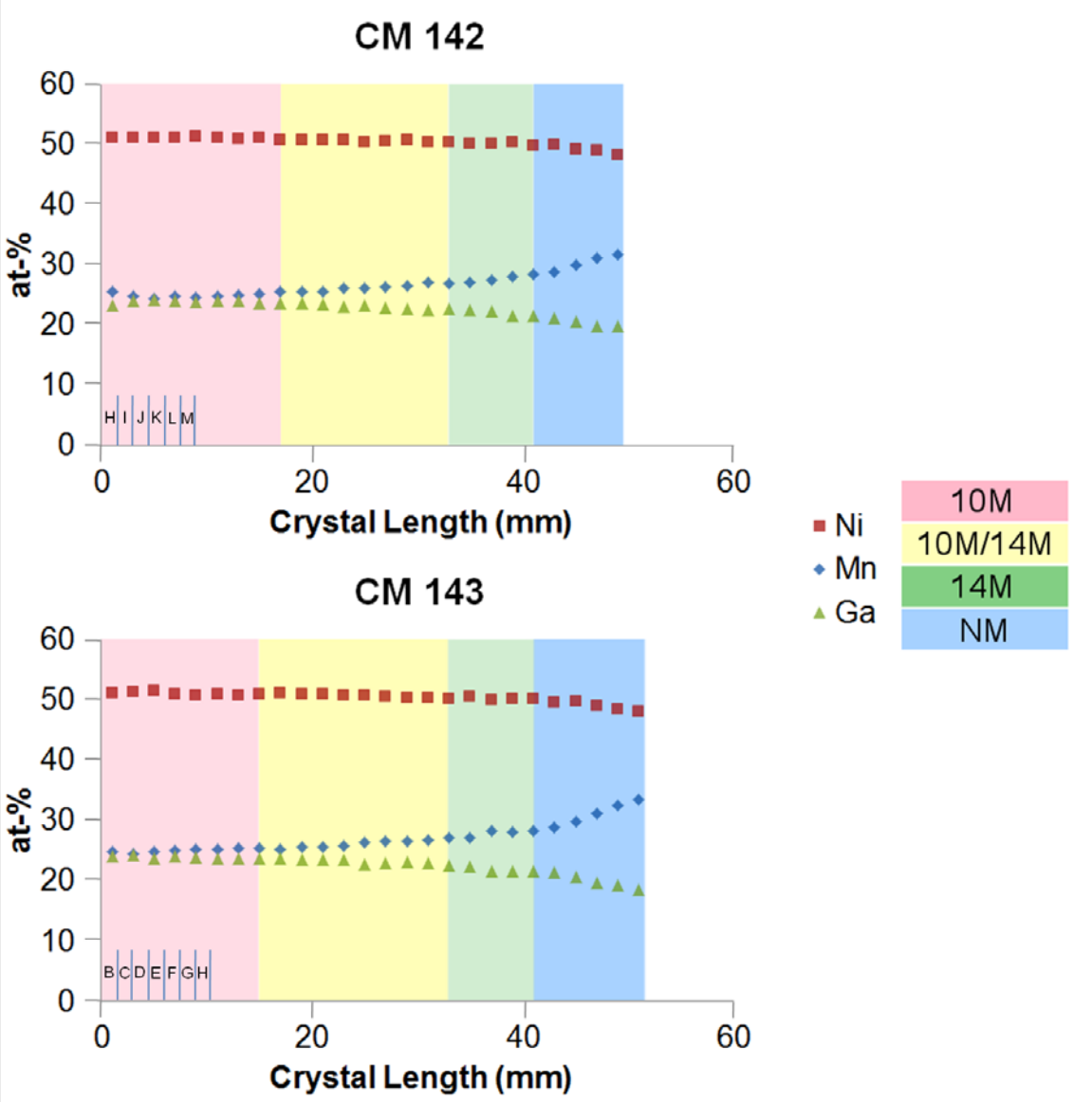

Figure A.1 XRD and EDS diagram for $Ni_{51.2}Mn_{26.6}Ga_{22.2}$ (at-%) single crystals, CM142 and CM143, with length below 100 mm used in fatigue testing. Data points represent crystal composition and shaded areas represent crystal structure. The seed end of the crystal is located at 0 mm. The letters in the bottom left corner of the diagram correspond to the locations of samples that were cut from the crystal. Reference Table A.3 for list of samples tested in the rotary instrument.

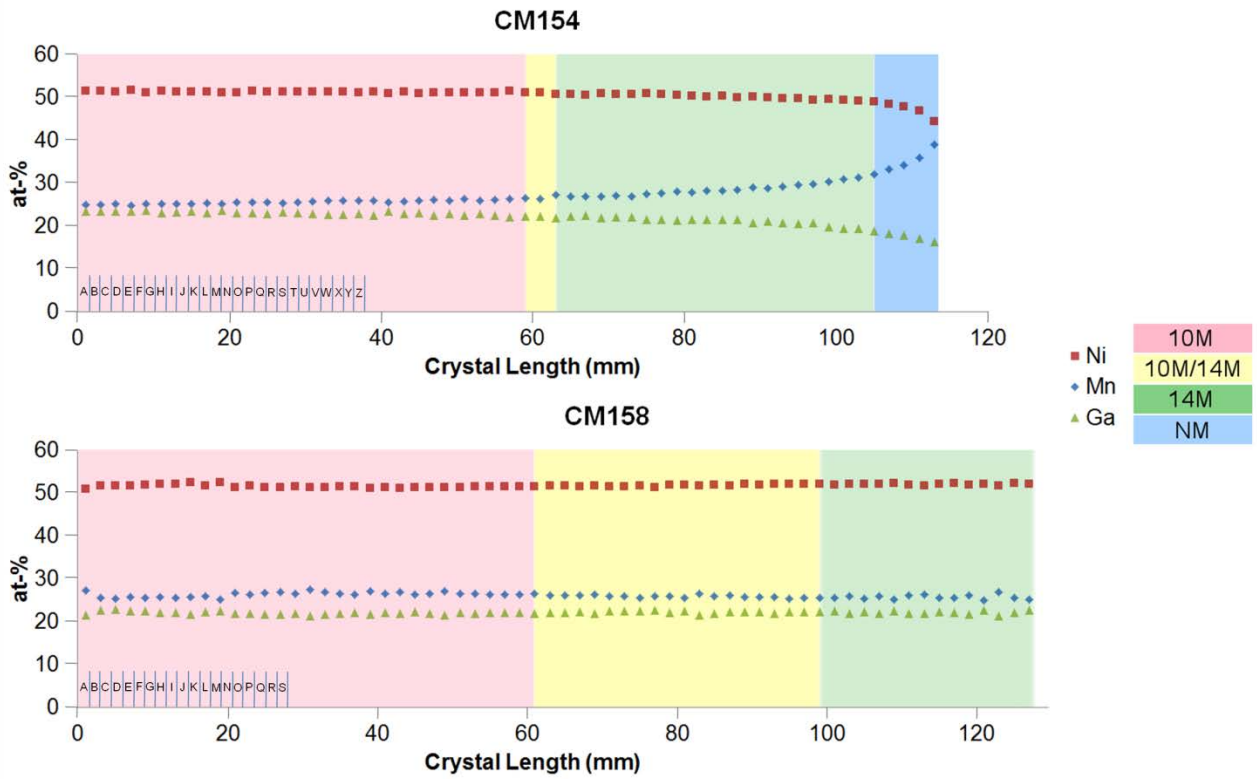

Figure A.2 XRD and EDS diagram for $Ni_{51.2}Mn_{26.6}Ga_{22.2}$ (at-%) single crystals, CM154 and CM158, with lengths longer than 100 mm used in fatigue testing. Data points represent crystal composition and shaded areas represent crystal structure. The seed end of the crystal is located at 0 mm. The letters in the bottom left corner of the diagram correspond to the locations of samples that were cut from the crystal. Reference Table A.3 for list of samples tested in the rotary instrument.

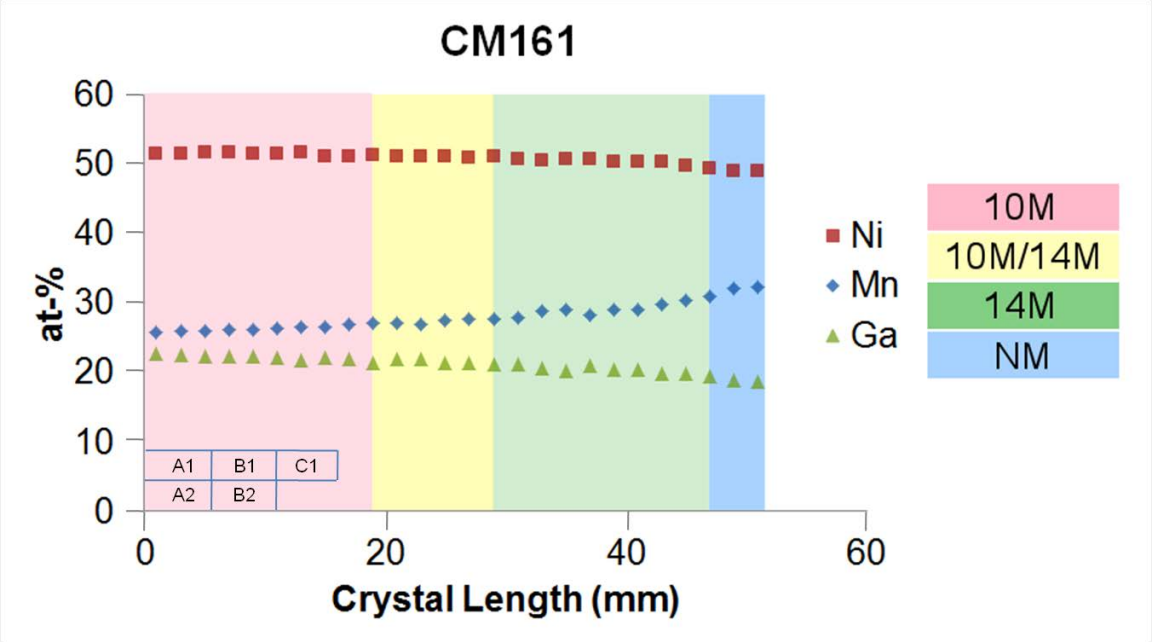

Figure A.3 XRD and EDS diagram for $Ni_{51.2}Mn_{26.6}Ga_{22.2}$ (at-%) single crystal with length below 100 mm used in compression testing. Data points represent crystal composition and shaded areas represent crystal structure. The seed end of the crystal is located at 0 mm. The letters and numbers in the bottom left corner of the diagram correspond to the locations of samples that were cut from the crystal. Reference Table 5.5 for list of compression samples.

The two tables below list the samples used in fatigue testing and include the average switching field parallel and perpendicular to the sample face, sample preparation, and average surface roughness.

Table A.3 List of samples used in fatigue testing including average switching field with *H* applied parallel and perpendicular to the sample face as well as the respective level of mechanical polish and whether or not the sample was notched.

		Average Switching Field H Parallel to Sample Face (MA/m)		Average Switching Field H Perpendicular to Sample Face (MA/m)		
Single Crystal	Sample	Measured	Effective	Measured	Effective	Sample Preparation
CM132	A	0.32	0.29	0.24	0.02	3μm
CM132	B	0.18	0.16	0.37	0.05	
CM132	C	0.23	0.21	0.29	0.11	
CM132	D	0.22	0.20	0.34	0.22	1μm
CM132	E	0.16	0.15	0.33	0.20	
CM132	F	0.16	0.15	0.34	0.21	
CM142	H	0.26	0.23	0.24	0.14	3μm
CM142	I	0.15	0.13	0.23	0.12	
CM142	J	0.16	0.15	0.28	0.17	
CM142	K	0.14	0.12	0.17	0.06	
CM142	L	0.18	0.16	0.18	0.07	
CM142	M	0.22	0.20	0.14	0.03	
CM143	F	0.23	0.21	0.30	0.15	3μm
CM143	G	0.14	0.11	0.23	0.12	
CM143	H	0.24	0.22	0.40	0.21	
CM154	A	0.25	0.18	0.32	0.07	3μm
CM154	D	0.23	0.16	0.33	0.08	
CM154	E	0.22	0.19	0.23	0.10	
CM154	F	0.18	0.16	0.23	0.14	
CM154	G	0.16	0.13	0.23	0.12	
CM154	H	0.20	0.17	0.27	0.12	
CM154	I	0.20	0.17	0.21	0.12	
CM154	J	0.14	0.11	0.31	0.19	HNO3
CM154	K	0.17	0.15	0.25	0.11	Notched
CM154	L	0.14	0.07	0.37	0.20	
CM154	M	0.15	0.14	0.41	0.20	
CM154	N	0.11	0.09	0.31	0.13	
CM154	O	0.13	0.11	0.40	0.23	HNO3
CM154	P	0.20	0.18	0.35	0.25	
CM154	Q	0.17	0.14	0.45	0.28	
CM154	R	0.16	0.12	0.45	0.28	
CM154	S	0.21	0.17	0.40	0.21	

CM154	T	0.21	0.18	0.38	0.20	
CM154	U	0.22	0.19	0.29	0.34	
CM154	V	0.17	0.12	0.24	0.07	0.04µm
CM154	W	0.19	0.17	0.27	0.04	
CM154	X	0.18	0.15	0.28	0.13	
CM154	Y	0.21	0.17	0.27	0.11	
CM154	Z	0.23	0.19	0.29	0.12	
CM158	N	0.13	0.11	0.17	0.08	3µm
CM158	O	0.20	0.18	0.21	0.03	Notched
CM158	P	0.20	0.18	0.16	0.04	
CM158	Q	0.23	0.20	0.20	0.07	
CM158	R	0.22	0.21	0.19	0.06	
CM158	S	0.23	0.20	0.16	0.05	

Table A.4 List of samples used in fatigue testing including the calculated stress required to initiate twin boundary motion, fatigue life, and average surface roughness. Notched samples were not cycled to fracture.

Single Crystal	Sample	Effective Twinning Stress Parallel to Sample Face (MPa)	Effective Twinning Stress Perpendicular to Sample Face (MPa)	Revolutions to Fracture	Surface Roughness (nm)	Sample Preparation
CM132	A	-0.62	-0.35	50000	25.62	3µm
CM132	B	-0.19	-0.81	138000	35.08	
CM132	C	-0.32	-0.49	10000	25.11	
CM132	D	-0.28	-0.67	50000	12.88	1µm
CM132	E	-0.16	-0.63	40000	18.64	
CM132	F	-0.15	-0.67	70000	9.46	
CM142	H	-0.48	-0.42	60000	30.64	3µm
CM142	I	-0.15	-0.40	30000	24.95	
CM142	J	-0.20	-0.58	10000	30.92	
CM142	K	-0.14	-0.21	50000	29.39	
CM142	L	-0.23	-0.24	10000	43.40	
CM142	M	-0.35	-0.14	20000	50.60	
CM143	F	-0.40	-0.65	94000	26.34	3µm
CM143	G	-0.14	-0.40	60000	35.08	
CM143	H	-0.43	-1.17	414000	25.11	
CM154	A	-0.44	-0.72	100000	48.31	3µm
CM154	D	-0.38	-0.74	274000	21.51	
CM154	E	-0.33	-0.38	260000	20.14	
CM154	F	-0.22	-0.37	17000	124.60	
CM154	G	-0.17	-0.35	19000	88.72	

CM154	H	-0.27	-0.51	13000	113.29	
CM154	I	-0.28	-0.32	2000	63.84	
CM154	J	-0.14	-0.66		92.92	HNO3
CM154	K	-0.19	-0.42		93.89	Notched
CM154	L	-0.14	-0.98		83.57	
CM154	M	-0.16	-1.17		117.23	
CM154	N	-0.08	-0.66		89.96	
CM154	O	-0.11	-1.13	30000	166.45	HNO3
CM154	P	-0.27	-0.88	30000	231.76	
CM154	Q	-0.20	-1.44	20000	132.73	
CM154	R	-0.17	-1.45	70000	129.84	
CM154	S	-0.31	-1.09	30000	113.41	
CM154	T	-0.30	-1.02	40000	164.94	
CM154	U	-0.33	-0.57	8000	130.10	
CM154	V	-0.19	-0.39	405000	16.19	0.04µm
CM154	W	-0.26	-0.52	25000	21.91	
CM154	X	-0.22	-0.54	155000	16.13	
CM154	Y	-0.30	-0.49	115000	12.91	
CM154	Z	-0.36	-0.57	65000	13.97	
CM158	N	-0.12	-0.21		19.93	3µm
CM158	O	-0.31	-0.33		19.70	Notched
CM158	P	-0.31	-0.19		30.81	
CM158	Q	-0.40	-0.28		13.34	
CM158	R	-0.36	-0.26		15.09	
CM158	S	-0.38	-0.18		16.95	

The figures below include average effective switching field data from three tests and the standard deviation at various intervals during testing as well as calculated effective magnetostress as a function of magnetic field. The maximum effective magnetostress is the effective twinning stress. The left column of figures corresponds to the magnetic field applied parallel to the sample face in the $[010]_S$ direction, and the right column corresponds to the magnetic field applied perpendicular to the sample face in the $[001]_S$.

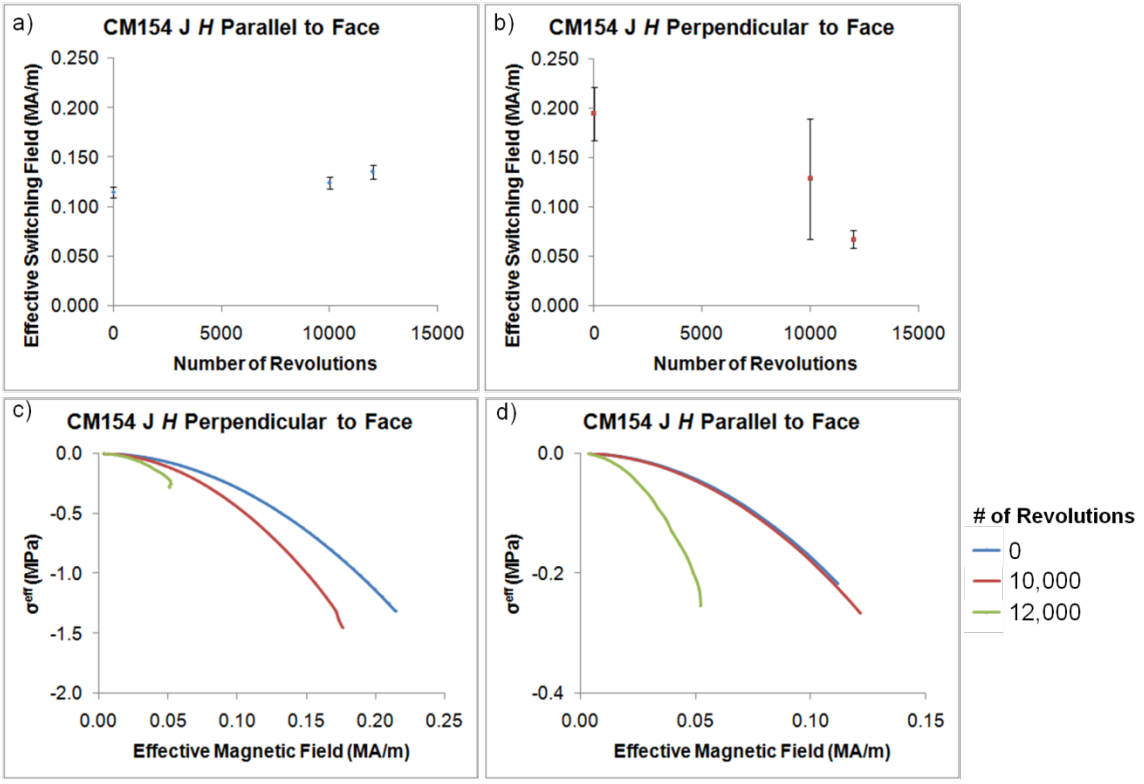

Figure A.4 CM154 J a) Effective switching field measured for prior to testing through 12,000 revolutions with the magnetic field applied parallel to the sample face in the $[010]_S$ direction. b) Effective switching field measured for prior to testing through 12,000 revolutions with the magnetic field applied perpendicular to the sample face in the $[001]_S$ direction. c) Effective compressive stress as a function of magnetic field applied parallel to the sample face in the $[010]_S$ direction prior to testing through 12,000 revolutions. d) Effective compressive stress as a function of magnetic field applied perpendicular to the sample face in the $[001]_S$ direction prior to testing through 12,000 revolutions.

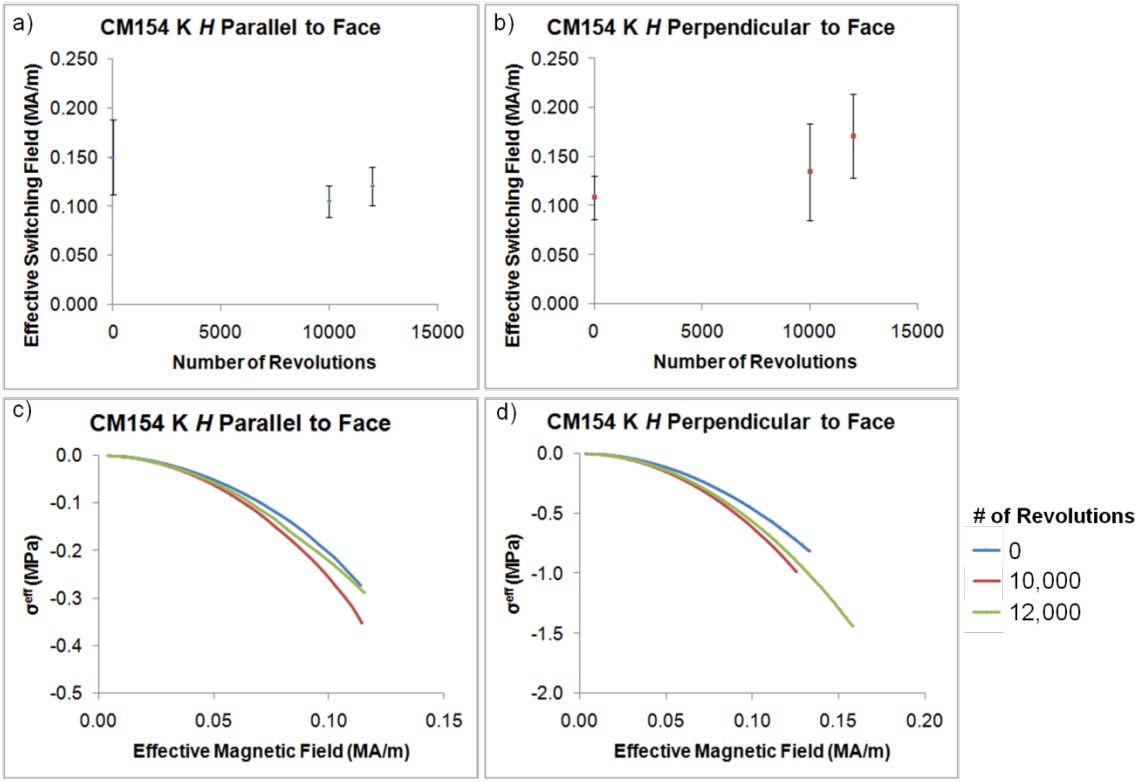

Figure A.5 CM154 K a) Effective switching field measured prior to testing through 12,000 revolutions with the magnetic field applied parallel to the sample face in the $[010]_S$ direction. b) Effective switching field measured prior to testing through 12,000 revolutions with the magnetic field applied perpendicular to the sample face in the $[001]_S$ direction. c) Effective compressive stress as a function of magnetic field applied parallel to the sample face in the $[010]_S$ direction prior to testing through 12,000 revolutions. d) Effective compressive stress as a function of magnetic field applied perpendicular to the sample face in the $[001]_S$ direction prior to testing through 12,000 revolutions.

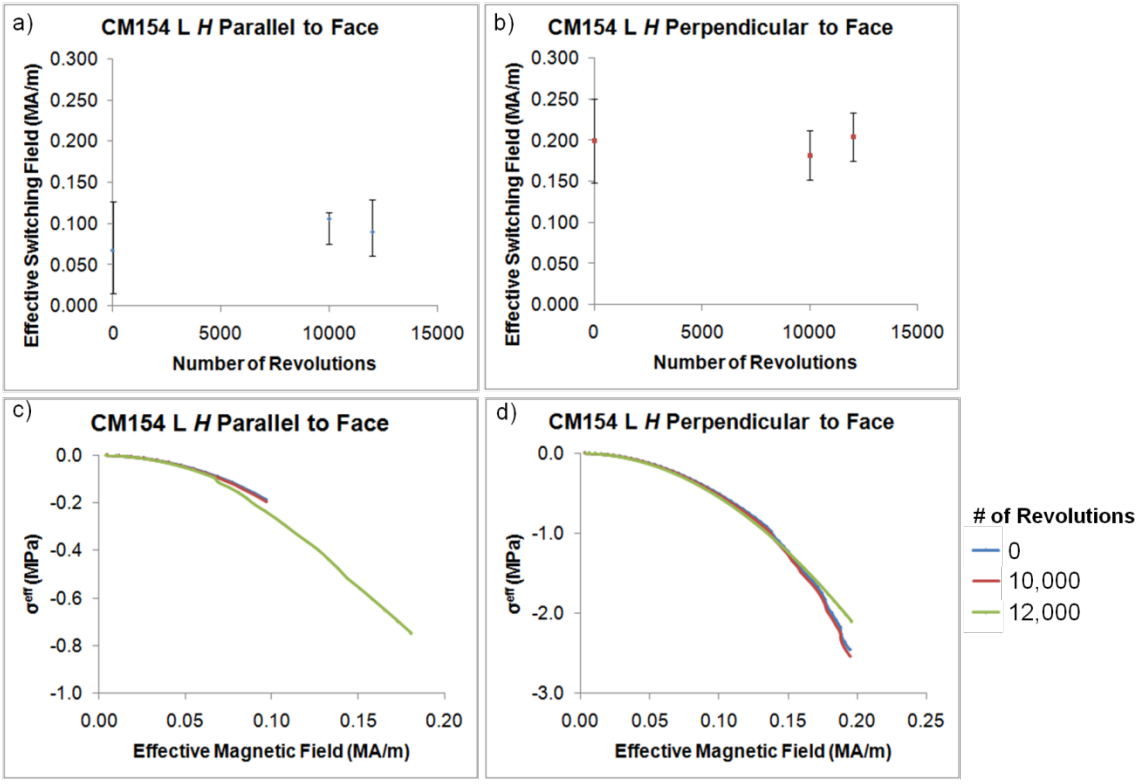

Figure A.6 CM154 L a) Effective switching field measured for prior to testing through 12,000 revolutions with the magnetic field applied parallel to the sample face in the $[010]_S$ direction. b) Effective switching field measured for prior to testing through 12,000 revolutions with the magnetic field applied perpendicular to the sample face in the $[001]_S$ direction. c) Effective compressive stress as a function of magnetic field applied parallel to the sample face in the $[010]_S$ direction prior to testing through 12,000 revolutions. d) Effective compressive stress as a function of magnetic field applied perpendicular to the sample face in the $[001]_S$ direction prior to testing through 12,000 revolutions.

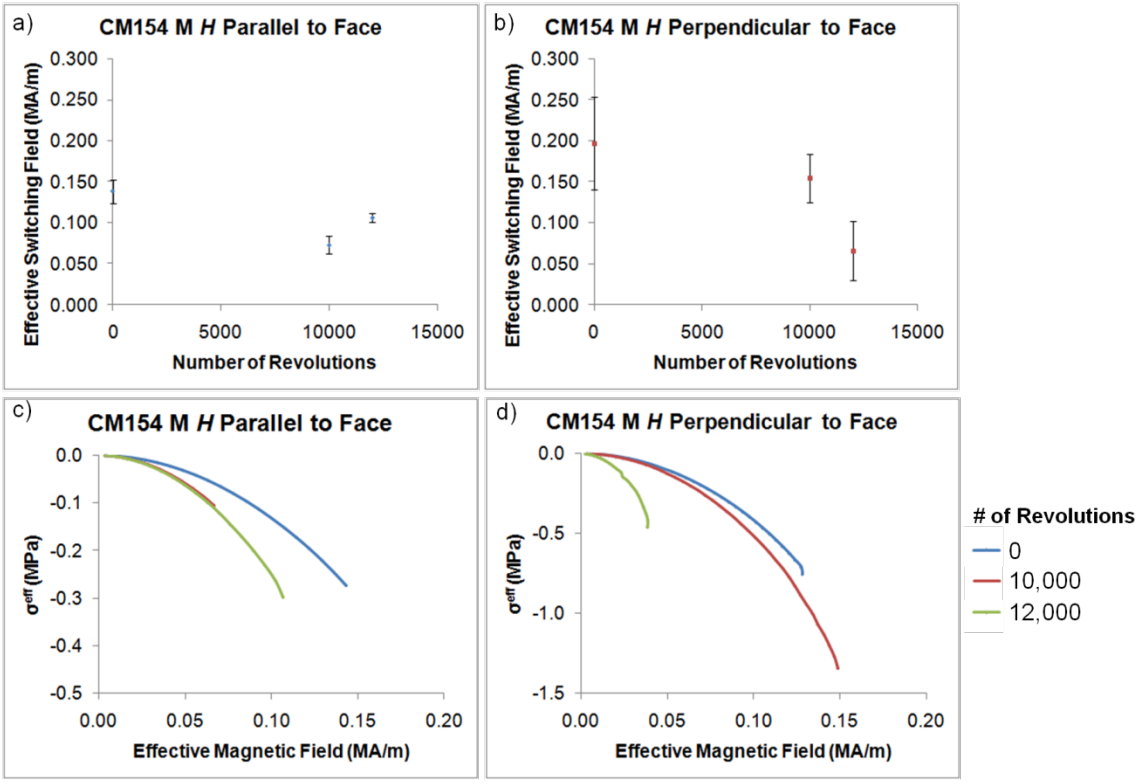

Figure A.7 CM154 M a) Effective switching field measured for prior to testing through 12,000 revolutions with the magnetic field applied parallel to the sample face in the $[010]_S$ direction. b) Effective switching field measured for prior to testing through 12,000 revolutions with the magnetic field applied perpendicular to the sample face in the $[001]_S$ direction. c) Effective compressive stress as a function of magnetic field applied parallel to the sample face in the $[010]_S$ direction prior to testing through 12,000 revolutions. d) Effective compressive stress as a function of magnetic field applied perpendicular to the sample face in the $[001]_S$ direction prior to testing through 12,000 revolutions.

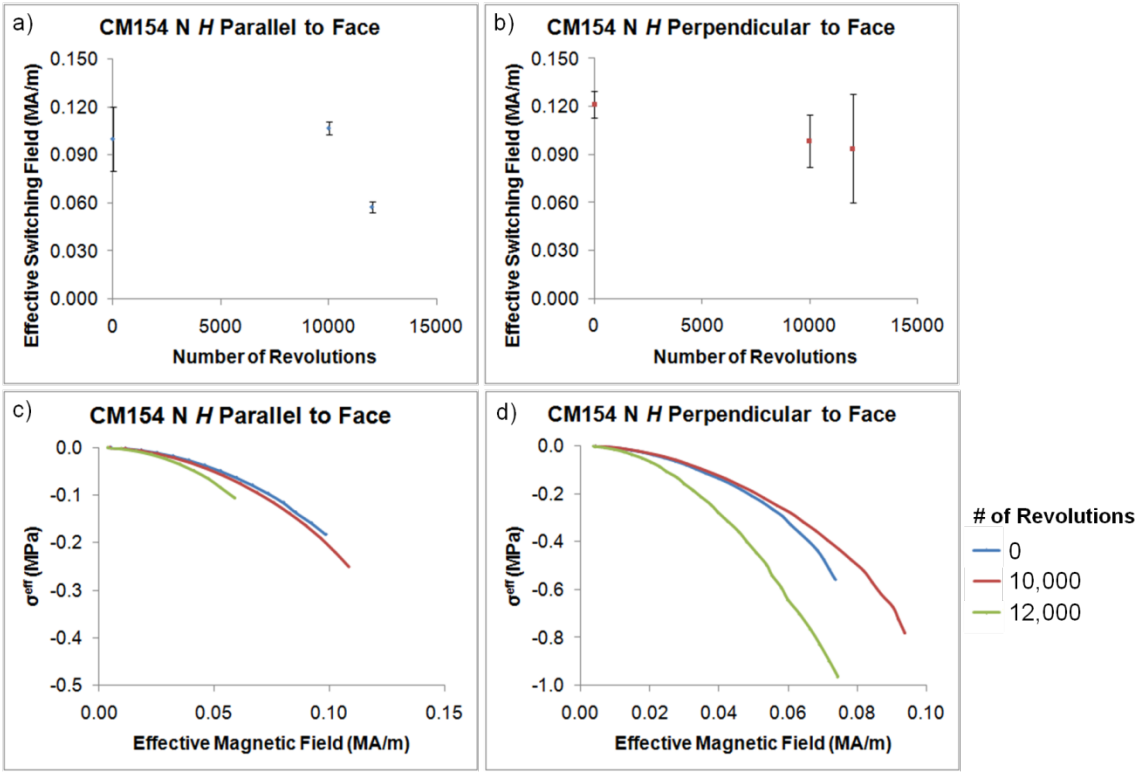

Figure A.8 CM154 N a) Effective switching field measured for prior to testing through 12,000 revolutions with the magnetic field applied parallel to the sample face in the $[010]_S$ direction. b) Effective switching field measured for prior to testing through 12,000 revolutions with the magnetic field applied perpendicular to the sample face in the $[001]_S$ direction. c) Effective compressive stress as a function of magnetic field applied parallel to the sample face in the $[010]_S$ direction prior to testing through 12,000 revolutions. d) Effective compressive stress as a function of magnetic field applied perpendicular to the sample face in the $[001]_S$ direction prior to testing through 12,000 revolutions.

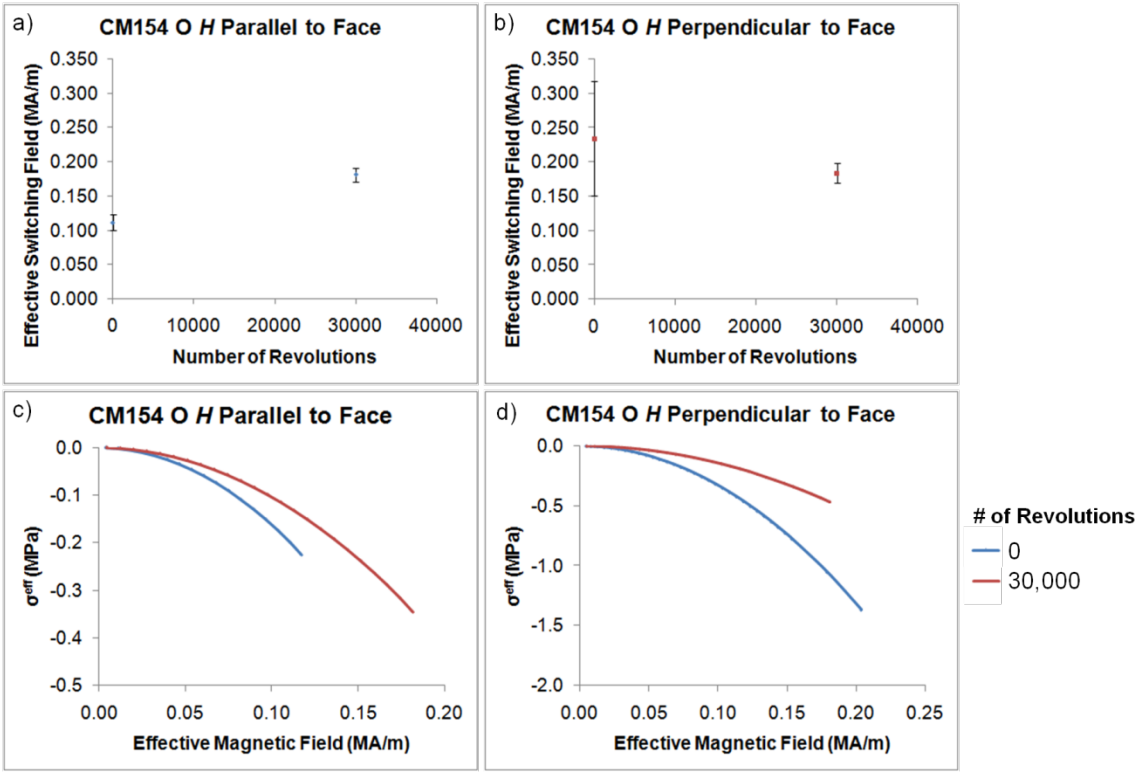

Figure A.9 CM154 O a) Effective switching field measured for prior to testing through 30,000 revolutions with the magnetic field applied parallel to the sample face in the $[010]_S$ direction. b) Effective switching field measured for prior to testing through 30,000 revolutions with the magnetic field applied perpendicular to the sample face in the $[001]_S$ direction. c) Effective compressive stress as a function of magnetic field applied parallel to the sample face in the $[010]_S$ direction prior to testing through 30,000 revolutions. d) Effective compressive stress as a function of magnetic field applied perpendicular to the sample face in the $[001]_S$ direction prior to testing through 30,000 revolutions.

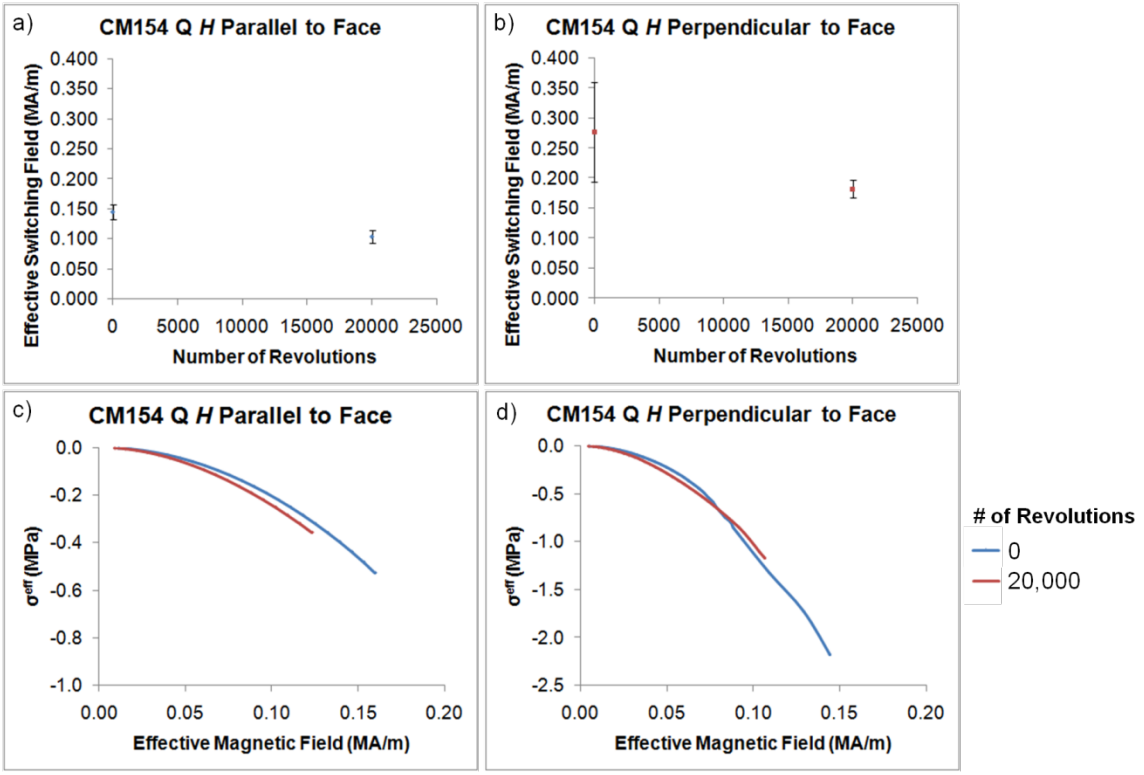

Figure A.10 CM154 Q a) Effective switching field measured for prior to testing through 20,000 revolutions with the magnetic field applied parallel to the sample face in the $[010]_S$ direction. b) Effective switching field measured for prior to testing through 20,000 revolutions with the magnetic field applied perpendicular to the sample face in the $[001]_S$ direction. c) Effective compressive stress as a function of magnetic field applied parallel to the sample face in the $[010]_S$ direction prior to testing through 20,000 revolutions. d) Effective compressive stress as a function of magnetic field applied perpendicular to the sample face in the $[001]_S$ direction prior to testing through 20,000 revolutions.